8|VII-97

ISSN 0234-5366

КРАТКИЕ СООБЩЕНИЯ ОИЯИ

JINR RAPID COMMUNICATIONS

2[82]-97

Издательский отдел ОИЯИ ДУБНА

JINR Publishing Department DUBNA

Объединенный институт ядерных исследований
Joint Institute for Nuclear Research

2[82]-97

КРАТКИЕ СООБЩЕНИЯ ОИЯИ

JINR RAPID COMMUNICATIONS

Дубна 1997

ОГЛАВЛЕНИЕ
CONTENTS

УДК 539.14

COLLECTIVE ENERGY DISSIPATION AND FLUCTUATIONS IN ELASTOPLASTIC SYSTEMS

T.I.Mikhailova[1], *I.N.Mikhailov*[2], *M.Di Toro*[3]

Starting from the equations of motion of a simple system possessing the properties of elastic and plastic bodies, we reconstruct its Lagrangian and Hamiltonian functions and also the so-called Rayleigh dissipation function. This allows us to find the rate of the system «heating» and to analyse the fluctuations of the basic observables. In this way a rather general scheme of solving analogous problems in more complex elastoplastic systems is established.

The paper gives a basis for studying open problems in the nuclear fusion and heavy-ions quasi-elastic collisions processes. It may be applied also for the theoretical treatment of dynamical problems in the other mesoscopic systems of fermions.

The investigation has been performed at the Bogoliubov Laboratory of Theoretical Physics and Laboratory of Nuclear Problems, JINR in collaboration with INFN (Catania, Italy).

Диссипация коллективной энергии и флуктуации в эластопластических системах

Т.И.Михайлова, И.Н.Михайлов, М. Ди Торо

Беря за основу уравнения движения простой системы, обладающей свойствами упругих и пластических тел, мы восстанавливаем ее функции Лагранжа и Гамильтона, а также диссипативную функцию Рэлея. Это позволяет нам найти скорость «нагревания» системы и проанализировать флуктуации основных наблюдаемых. Таким образом устанавливается достаточно общая схема решения аналогичных проблем в более сложных эластопластических системах.

В работе представлен метод изучения проблем, возникающих в процессах слияния ядер и квазиупругих столкновений тяжелых ионов. Он может быть также использован для теоретического описания динамических задач в некоторых других системах, состоящих из большого, но конечного числа частиц.

Работа выполнена в Лаборатории теоретической физики им. Н.Н.Боголюбова и Лаборатории ядерных проблем, ОИЯИ в коллаборации с Национальным институтом ядерной физики (Катания, Италия).

[1]Laboratory of Nuclear Problems, JINR, Dubna

[2]Bogoliubov Laboratory of Theoretical Physics, JINR, Dubna

[3]Laboratorio Nazionale del Sud, INFN, Catania, Italy

1. Introduction

Elastoplastic materials are well known in nature. Their name signifies that these materials combine properties of elastic and plastic bodies. As the first, they respond with an elastic force restoring and initial configuration when they are brusquely disturbed, but as plastic materials they easily change their shape under an external pressure.

The mathematical studies of elastoplastic materials date to the time of Maxwell. Most of such studies concern macroscopic bodies for which the plasticity is a well understood property. However, for about a decade one discusses in the literature the elastoplastic properties of atomic nuclei [1], [2]. The microscopic (quantum) nature of nuclei demands some additional formal study of such systems. A study of this kind is presented in this paper on the basis of very simple equations of motion describing an elastoplastic dynamics.

The model considered below is similar but much simpler than the models describing nuclear elasto-plasticity. However, it allows some qualitative comparison with more realistic nuclear models and may be eventually generalized to study the nuclear processes in a quantitative way. One may think also that algorithms formulated in a way which is free from complications of a specific model may be used outside the realm of the nuclear physics, probably in the molecular physics and in the physics of atomic clusters.

The paper is organized as follows:

— In **Section 2** we give a general description of elastoplastic systems and present the equations of motion of a simple elastoplastic system which will be subjected for examination. The model is compared with the one describing collective dynamics in the nuclear fusion process.

— In **Section 3** we give a Rayleigh-Lagrange form for the equations of motion.

— In **Section 4** we define the collective Hamiltonian and study the rate of the collective energy dissipation.

— **Section 5** is devoted to the study of the fluctuations of the collective energy in the system analysed before. The Langevin-type equations are formulated for collective variables. We find that the fluctuations of some of collective variables are suppressed at the beginning of regaining the equilibrium state.

— We finish the paper with a short conclusion.

2. Elasto-Plastic Systems and Nuclei

Consider a system described by the equations

$$\frac{1}{2}\ddot{Q}+\frac{\alpha}{2}Q=\Pi, \tag{1}$$

$$\dot{\Pi}+\frac{\beta}{2}\dot{Q}=-\frac{1}{\tau}\Pi. \tag{2}$$

The right-hand side of Eq.(1) plays a role of a part of the force affecting the physical quantity $Q(t)$. The second of these equations may be transformed to an integral form giving

$$\Pi(t) = -\frac{\beta}{2}\int_{t_0}^{t} dt' \exp\left(-\frac{t-t'}{\tau}\right)\dot{Q}(t') + C\exp\left(-\frac{t}{\tau}\right) \tag{3}$$

and showing that this part of the force is determined by the evolution of the system during the preceding period of time of the order of τ. One may say that the system «decides» what to do in the next moment recollecting information on what had happened to it before. For this reason this system could be called also as a system with a «memory». Thus, the parameter τ determines the memory scale. In the processes going slowly in this scale (in adiabatic processes) the system described by Eqs.(1), (2) follows in its evolution an equation of motion of a vibrator with the frequency $\sqrt{\alpha}$ ($\alpha > 0$) damped by the friction force $\chi Q(t)$ where $\chi = \tau\beta/2$:

$$\frac{1}{2}\ddot{Q} + \chi\dot{Q} + \frac{\alpha}{2}Q = 0. \tag{4}$$

When $\chi^2 \geq \alpha$, vibrations are overdamped, and the body is plastic.

The fast (diabatic) processes in the same system proceed as if the system were an elastic body (see Ref.2):

$$\ddot{Q} + (\alpha + \beta)Q = 0.$$

In this regime the vibrational frequency is renormalized and is equal to $\Omega = \sqrt{\alpha + \beta}$.

Choosing an appropriate time scale one may always transform the parameters in Eq.(1) and Eq.(2) in such a way that $|\alpha| = 1$. The elastoplastic properties are then well pronounced when $\beta >> 1$. The «memory» scale parameter τ determines the division of the perturbations into the slow and the fast ones: subjected to fast perturbations the system reacts as an elastic body, in the other case — as a plastic one.

The evolution of the system described by Eqs.(1),(2) is demonstrated in Fig.1 and Fig.2. Here the time dependence of Q and Π variables is shown for a «large» value of β

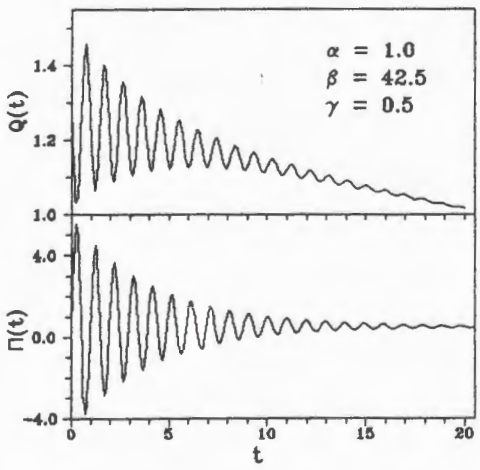

Fig.1. Above: time dependence of Q variable; below: time dependence of Π variable for $\alpha = 1$, $\beta = 42.5$ and $\gamma = 0.5$

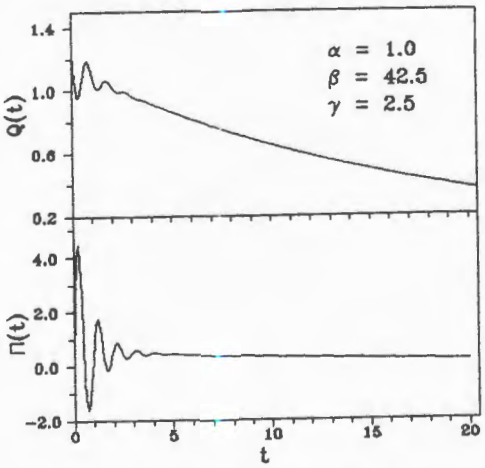

Fig.2. Same as in Fig.1 for $\alpha = 1$, $\beta = 42.5$ and for $\gamma = 2.5$

and for two different values of $\gamma = \tau^{-1}$. Elastic properties are more pronounced for small values of γ, but are distinctly seen even when it becomes comparable with the «diabatic» vibrational frequency $\sqrt{\beta}$.

Regarding the nonzero starting values of Q and $\dot{Q}(t)$ variables as a result of instantaneous external perturbation, one may say that an external force applied to such a system produces at the beginning phenomena typical for elastic bodies. The final part of the evolution process corresponds to an exponential decrease of the absolute value of the variable Q (when $\alpha > 0$). Hence, the way of coming to the equilibrium state of this system reveals its plastic properties.

Experiments using heavy ions with energies close to the Coulomb barrier performed during the last decade reveal rather unexpected nuclear properties. Depending on the experimental conditions, colliding heavy nuclei behave either as elastic bodies or as bodies made of a very plastic material. The studies of nuclear elastoplasticity have already a certain history [1], [2]. Equations (1) and (2) of the previous section have essentially the same structure as those obtained in Ref.2 for the description of the nuclear fusion. In application to the process, the elements in these equations have the following meaning:

a) The quantity $Q(t)$ is the $Q(t)_{2,0}$ component of the nuclear quadrupole mass tensor;

b) The quantity $\Pi(t)$ is the $(\lambda, \mu = 2,0)$ component of the intrinsic kinetic energy tensor;

c) The quantity $\alpha Q(t)$ in Eq.(1) substitutes the term in the corresponding equation considered in Ref.2 originating from the deformation dependence of the nuclear self-consistent potential $V(\mathbf{r}, t)$. The origin of the quantity $(\beta/2)\dot{Q}(t)$ in Eq.(2) lies in the coupling between the time dependent deformations of the geometrical and Fermi surfaces;

d) The parameter τ is nothing but the mean relaxation time appearing in the approximate expression for the «collision» or «relaxation» term in the microscopic theories based upon the kinetic equation.

For small Q values the model of Ref.2 gives a good description of nuclear giant quadrupole resonance [3]. The width of GQR in the daughter nucleus for the system of two fusing ^{58}Ni nuclei is well reproduced when $\gamma = h/\tau = 2.5$. The same equations [2] yield $\beta = 42.5$ for the same fusing system.

The nuclear elastoplasticity reveals itself in a number of ways. It determines the conditions for the fusion and explains the «extra push» phenomenon [4], [5]. It explains the anisotropy of γ-radiation from the low-spin fraction of fused nuclei.

The model of fusion formulated in Ref.2 allows a relatively simple numerical analysis and leads to a number of nontrivial predictions concerning the nuclear fusion. Having evident merits this model is, however, limited in its application for various reasons. One particular drawback of the model: it treats the collective processes taking place in nuclear reactions in a purely classical way. The equations of the model define a classical «trajectory» of the system which, at best, may be associated with some mean characteristics of the process. In quantal systems as nuclei, the fluctuations around the mean values play an important role.

The study of fluctuations in an elasto-plastic system is one of the subjects of this paper. There is another problem which we want to solve in this paper: the determination of the collective energy associated with the motion in the elasto-plastic system of the type described in Ref.2.

3. «Rayleigh–Lagrange» Form of Equations of Motion

To know the partition between the collective energy and the energy of intrinsic (statistical) excitation one must render the equations of motion a form as close as possible to a canonical Hamiltonian form. It turns out that it is easier to arrive first at the Lagrangian form of such equations and then to use the well-known algorithms to pass to the Hamiltonian form.

To render a canonical form to Eqs.(1),(2), let us consider the $\Pi(t)$ variable in these equations as a generalized velocity, introducing a generalized co-ordinate $Z(t)$ such that:

$$\Pi(t) = \dot{Z}(t). \tag{5}$$

Then Eqs.(1),(2) become

$$\begin{aligned} &\ddot{Q} + \alpha Q - 2\dot{Z} = 0, \\ &\frac{4}{\beta}\ddot{Z} + 2\dot{Q} = -4\frac{\dot{Z}}{\tau\beta}. \end{aligned} \tag{6}$$

If the right-hand side of the second of Eqs.(6) were equal to zero, these two equations would satisfy the conditions at which their standard Lagrangian formulation is possible [6]. The expression in the right-hand side could be also incorporated in the Lagrangian formulation. One may do it in the same way as one treats the friction force [6] by introducing two functions: the Lagrangian function

$$L = \frac{M_Q}{2}(\dot{Q}^2 - \alpha Q^2) + 2M_Q\left(\frac{1}{\beta}\dot{Z}^2 + \dot{Z}Q\right) \tag{7}$$

and the dissipation function

$$\Sigma = 2\frac{M_Q}{\tau\beta}\dot{Z}^2, \tag{8}$$

where M_Q is an arbitrary constant to be fixed later on.

4. Collective Energy

Now, we introduce the generalized momenta $P_i = \partial L/\partial\dot{Q}_i$ and the Hamiltonian function

$$H_{\text{coll}}(P_i, Q_i) = \sum_i P_i\dot{Q}_i - L.$$

The standard technique of transforming the Lagrange equations to the Hamiltonian form applied to the system, in which the dissipations function operates, leads to the following equations

$$\dot{Q}_i = \frac{\partial}{\partial P_i}H_{\text{coll}}, \qquad \dot{P}_i = -\left(\frac{\partial\Sigma}{\partial\dot{Q}_i} + \frac{\partial}{\partial Q_i}H_{\text{coll}}\right).$$

From these equations it follows:

$$\frac{d}{dt}H_{\text{coll}} = -\sum_i \dot{Q}_i \frac{\partial \Sigma}{\partial \dot{Q}_i}. \tag{9}$$

Using the above relations and the expressions of the previous section, one arrives at the definition of generalized momenta

$$P_Q = M_Q \dot{Q}, \quad P_Z = 2M_Q\left(\frac{2}{\beta}\dot{Z} + Q\right) \tag{10}$$

and at the following expression for the Hamiltonian function

$$H_{\text{coll}} = \frac{1}{2}\left(\frac{P_Q^2}{M_Q} + \alpha M_Q Q^2\right) + \frac{\beta M_Q}{2}\left(\frac{P_Z}{2M_Q} - Q\right)^2. \tag{11}$$

In this way one obtains a new form of the equations of motion

$$\dot{Q} = \frac{P_Q}{M_Q}, \qquad \dot{Z} = \left(\frac{\beta}{2}\right)\left(\frac{P_Z}{2M_Q} - Q\right), \tag{12}$$

$$\dot{P}_Q = -M_Q(\alpha+\beta)Q + \frac{\beta}{2}P_Z, \quad \dot{P}_Z = -2\frac{M_Q}{\tau}\left(\frac{P_Z}{2M_Q} - Q\right). \tag{13}$$

We associate the instantaneous value of the Hamiltonian function defined in Eq.(11) with the energy of collective motion accumulated in the system. Expressed in terms of the variables Q, $\dot{Q}$ and Π the collective energy becomes

$$E_{\text{coll.}} = \frac{M_Q}{2}\left(\dot{Q}^2 + \alpha Q^2 + \frac{4}{\beta}\Pi^2\right). \tag{14}$$

The first term in this expression may be interpreted as the kinetic energy of the collective flow, while the second is the deformation potential energy. Hence, the parameter M_Q in the Hamiltonian must be equal to the effective mass parameter of the collective flow in scrutiny. In the model described in Ref.2 and discussed in the previous section this is the mass parameter of a potential flow of nuclear matter, and α is given by the action of the surface and Coulomb potentials.

The last term in Eq.(14) is a part of the collective energy issuing from deformations of the Fermi surface of the system. It may be regarded then as a collective part of the intrinistic (kinetic) energy.

Collective energy constitutes in elastoplastic systems only a part of the total excitation energy, the rest of it being the energy of statistical excitation of the system. The collective energy is not conserved in such systems due to the relaxation phenomena associated with the finite value of the mean-relaxation-time parameter τ. The energy conservation law implies that the decrease of the collective energy is accompanied by the heating of the system. An example of the energy partition into different channels is shown in Fig.3 as a function of time. Notice the strong contribution of the collective intrinsic energy (in addition to the kinetic energy of collective flow) to the total energy of the system at small

Fig.3. , Partition of the total energy into different channels: 1) thermal energy $E_0 - E_{coll}$, 2) intrinsic collective energy $E_{intr} = M_Q \frac{2\Pi^2}{\beta}$, 3) potential energy $E_q = M_Q \frac{\alpha Q^2}{2}$, 4) kinetic energy of collective flow $E_{kin} = M_Q \frac{\dot{Q}^2}{2}$

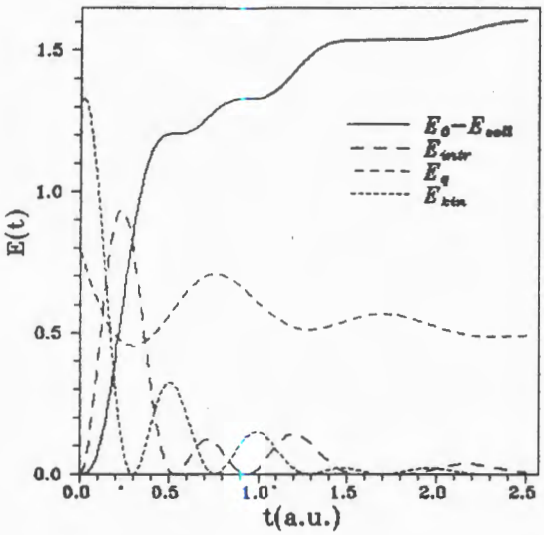

time when the regime of the motion has an elastic character. Only after the installation of the plastic (viscose) regime at larger time these two components of the energy disappear, and the temperature is well defined by the potential energy of the system.

5. Fluctuations in Classical Elastoplastic Systems

Equations (1), (2) chosen here to describe an elastoplastic system give a very limited information of such a complex many-body physical object: the time evolution of some collective degrees of freedom of it. The dissipation of the collective energy signifies an interaction of these degrees of freedom with the numerous others. The description given by these equations may be called «macroscopic» as, for example, one calls the description in terms of the friction force of a massive (Brownian) particle propagation through the liquid [7]. When the size of the Brownian particle decreases, the quality of such a description diminishes. To learn more about the motion of a «small» system, one must pass from the «macroscopic» to «microscopic» description. In this section we make a step towards it for our «elastoplastic system» following the standard techniques established for the study of the Brownian motion.

Let us introduce a «microscopic» Hamiltonian

$$H_{micr} = H_{coll} - ZF_\xi + H_\xi, \tag{15}$$

where H_{coll} is the collective Hamiltonian of Eq.(11) and H_ξ is an «intrinsic» Hamiltonian operating in the space of intrinsic co-ordinates and momenta (ξ). With the chosen form of the coupling term ($-ZF_\xi$), the Hamiltonian H_{micr} leads to the same equations of motion as in Eqs.(12) and in the first of Eqs.(13). The second of the latter equations takes the form:

$$\dot{P}_Z = F_\xi. \tag{16}$$

Now, we suggest that averaging of the «microscopic» Hamiltonian in the microscopic details of the intrinsic motion leads to former equations of motion, Eqs.(10—13). The average of the function F_ξ itself is a function of instant values of the collective variables. Pursuing our aim to find out more about the motion than we can learn from the equations for averaged in the intrinsic motion quantities, we write

$$F_\xi = \overline{F_\xi} + \delta F(t), \tag{17}$$

where $\delta F(t) = \delta F_\xi(\xi(t))$ is given by the intrinsic dynamics. We consider this quantity as a «random» function changing fast with the time.

We are looking now for the solution of equations of motion writing the unknown functions $Q(t)$, $P_Q(t)$, $Z(t)$ and $P_Z(t)$ in the form: $Q(t) = \overline{Q(t)} + \delta Q(t)$, etc.

From our definitions it follows that $\overline{\delta F(t)} = 0$. Consequently, the equations of motion for averaged quantities coincide with those which we have introduced (e.g., with Eqs.(12),(13)) for the quantities carrying no averaging mark.

The evolution of the quantity δQ is given by:

$$\frac{d^3\delta Q}{dt^3} + \frac{1}{\tau}\frac{d^2\delta Q}{dt^2} + (\alpha+\beta)\frac{d\delta Q}{st} + \frac{\alpha}{\tau}\delta Q = \frac{\beta}{2M_Q}\delta F(t) \tag{18}$$

and $\delta Q(t)$ may be written as [8]:

$$\delta Q(t) = \frac{\beta}{2M_Q}\int_0^t dt' G(t-t')\delta F(t'), \tag{19}$$

where:

$$G(t) = \frac{1}{[(a_1-a_2)^2+b^2]}\left\{\exp(-a_1 t) - \exp(-a_2 t)\left(\cos(bt) + \frac{(a_2-a_1)}{b}\sin(bt)\right)\right\}. \tag{20}$$

In Eq.(20) the following notations are used: $\lambda_1 = -a_1$, $\lambda_2 = -a_2 + ib$ and $\lambda_3 = -a_2 - ib$; λ_i being the roots of the third order algebraic equation

$$\lambda^3 + \frac{1}{\tau}\lambda^2 + (\alpha+\beta)\lambda + \frac{\alpha}{\tau} = 0. \tag{21}$$

The quantity $\delta Q(t)$ determines also the other functions entering into the collective energy (14) and in particular $\delta P_Q(t)$. Obviously, the averaging of solutions renders the quantities $\delta Q(t)$ and $\delta P_Q(t)$ equal to zero. However, the average values of $(\delta Q)^2$ and $(\delta P_Q)^2$ are not equal to zero. To find these quantities one must calculate integrals containing the expression $\Phi(t-t') = \overline{\delta F(t)\delta F(t')}$.

To do it, we assume that the function $\delta F(t)$ changes fast with the time, and that the following approximation for the function $\Phi(t-t')$ may be used:

$$\Phi(t-t') = \sigma^2\delta(t-t'), \tag{22}$$

where the quantity $\sigma^2 = \sigma_0^2 T$ measures the amplitude of perturbations introduced by the random force $\delta F(t)$. Then

$$\overline{(\delta Q(t))^2} = \left(\frac{\sigma_0 \beta}{2M_Q} \right)^2 \int_0^t dt' G(t-t')^2 T(t'). \tag{23}$$

The value of parameter σ in Eq.(22) may be determined from the thermal equilibrium conditions between the collective and intrinsic motions, just as in the case of the Brownian motion. We remind that the last term in the expression (14) for the collective energy represents intrinsic degrees of freedom. The fluctuating force $\delta F(t)$ contributes, in particular a term

$$\overline{\delta E^{Q}_{\text{coll}}(t)} = \frac{M_Q}{2} \left(\overline{\delta \dot{Q}^2} + \alpha \overline{\delta Q^2} \right) \tag{24}$$

to the part of the collective energy which represents the «Q» degree of freedom in the collective Hamiltonian in Eq.(11).

In the case of the thermal equilibrium with a medium (i.e., with the ensemble of intrinsic degrees of freedom) at the temperature T (which is here supposed to be sufficiently high) the system must accumulate on the average an energy $\delta E^{Q}_{\text{coll}}(T) = kT$, where k is the Boltzmann constant. Equating $\delta E^{Q}_{\text{coll}}(t \to \infty) \equiv (\sigma)^2 \Delta$ with the latter expression one finds:

$$\sigma^2 = \frac{kT}{\Delta}. \tag{25}$$

Suggesting a Gauss distribution of the fluctuating quantities one may find the probability of deviations of these observables from their positions on the macroscopic trajectory [7]. In systems with strongly accentuated elastoplasticity, where $\beta >> \alpha$ and $\sqrt{\beta} >> 1/2\tau$, the quantity $\overline{\delta Q^2}$ regarded as a function of time lags behind $\overline{\delta \dot{Q}^2}$ in its saturation properties during the time $0 < t \le \tau\beta/\alpha$ (Fig.4). As a result during this time interval the averaged fluctuation energy in Eq.(24) remains lower than kT. One may say that the temperature determining the statistical properties of quantities depending on Q and $\dot{Q}$ and defined as

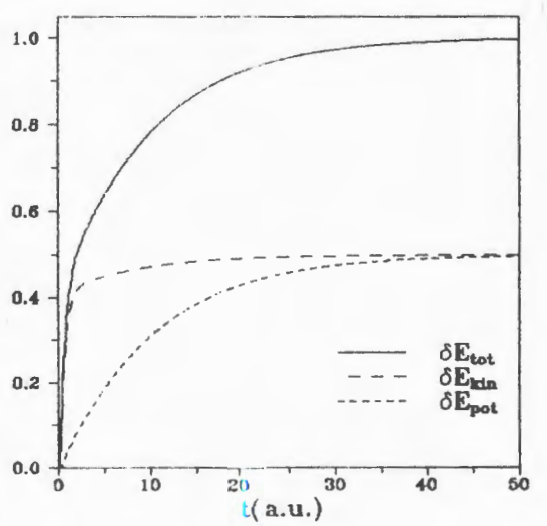

Fig.4. Time dependence of averaged fluctuating collective energy in «Q» channel $\overline{\delta E_{\text{coll}}(t)}$ devided by its asymptotic value $\overline{\delta E_{\text{coll}}(t \to \infty)}$ and of the functions $\delta E_{\text{pot}} = \sqrt{\overline{\delta Q^2}}$ and $\delta E_{\text{kin}} = \sqrt{\overline{\delta \dot{Q}^2}}$

$kT^* = \overline{\delta E^{Q}_{\text{coll}}(t)}$ is lower than the instantaneous value of the real temperature $T(t)$ in the system during the time interval $0 < t \leq \tau\beta/\alpha$.

6. Concluding Remarks

Above we suggested a way to render the equations of a simple elastoplastic system a form close to the canonical Hamiltonian form. The algorithm of this procedure may surely be used in more complex and more realistic situations like the one met in the description of the heavy-ion fusion.

In this way we succeeded to establish the partition of the energy of an elastoplastic system into the collective and statistical components. This allows us to determine the time dependence of the temperature of the system. Our studies show that the temperature is not always given by the energy transmitted from the collective degree of freedom related with the system's geometry: a part of the collective energy is accumulated by the intrinsic degrees of freedom.

Another point which we consider to be of importance is a certain advance achieved here in treating the fluctuations in an elastoplastic system. We show that during the time when the elastic properties of the system dominate the motion, the fluctuations in the collective channel are hindered due to its coupling with the channel of intrinsic excitations.

These observations could be very important for studying the conditions for the heavy-ions fusion and the accompanying processes such as the radiation generated by their heating. These preliminary conclusions demand further analysis, and we are planning to start it without much delay.

References

1. Nörenberg W. et al. — Phys. Lett., 1981, v.104B, p.107.
2. Mikhailov I.N., Mikhailova T.I., Di Toro M. et al. — Nucl. Phys., 1996, v.A604, p.368..
3. Balbutsev E.B., Mikhailov I.N. — In: «Collective Nuclear Dynamics». Editor R.Djolos, Leningrad «Nauka», USSR, 1990, p.3.
4. Swiatecki W.J. — Nucl. Phys., 1982, v.A 376, p.275.
5. Bjørnholm S. — Nucl. Phys., 1982, v.A 387, p.51c.
6. Goldstein H. — Classical Mechanics (second edition), p.21, Addison-Wisley Series in Physics, 1959.
7. Balescu R. — Equilibrium and Nonequilibrium Statistical Mechanics, v.2, ch.11. A Wiley-Interscience Publication, John Wiley and Sons, 1975.
8. Bronstein K.A., Semendiaev I.N. — Handbook on Mathematics, Moscow, «Nauka», 1986.

Received on December 24, 1996.

УДК 621.384.66
621.384.663

СИСТЕМА ДИАГНОСТИКИ ЦИРКУЛИРУЮЩЕГО ПУЧКА НУКЛОТРОНА НА ОСНОВЕ МИКРОКАНАЛЬНЫХ ПЛАСТИН

А.А.Балдин, В.В.Борисов, Л.Г.Ефимов, В.С.Королев, К.В.Михайлов, С.В.Семашко

Описана конструкция системы диагностики циркулирующего пучка нуклотрона ЛВЭ ОИЯИ на основе микроканальных пластин. Представлены технические характеристики и результаты эксплуатации системы.

Работа выполнена в Лаборатории высоких энергий ОИЯИ.

Diagnostics System of the Circulating Beam of the Nuclotron Based on Microchannel Plates

A.A.Baldin et al.

The construction of the diagnostics system of the circulating beam of the LHE, JINR Nuclotron based on microchannel plates is described. Technical characteristics and results of maintenance of the system are represented.

The investigation has been performed at the Laboratory of High Energies, JINR.

1. Введение

К основным параметрам, контролируемым при настройке и эксплуатации ускорителя, относятся интенсивность и пространственные характеристики пучка (профили, размеры, положение центра тяжести). При этом особое внимание уделяется возможности контроля динамики указанных параметров в режимах инжекции, ускорения и вывода [1], [2].

В рамках подготовки детекторной базы установки МАРУСЯ наша задача формулировалась как создание перспективных средств диагностики пучков в широком диапазоне интенсивностей (от 10^4 до 10^{12} зарядов за цикл), который не перекрывается существующими средствами. Для решения указанной задачи нами был изготовлен и испытан прототип детектора ионизационного типа на основе микроканальных пластин [3].

Использование МКП в координатных и временных детектирующих системах для решения различных измерительных задач [4—12], в частности, для профилометрии и спектрометрии пучков на ускорителях [13,14], позволяет реализовать их уникальные возможности: загрузочные способности до 10^6 част.$\cdot$см$^{-1}\cdot$с$^{-1}$, пространственное разрешение на уровне ~ 10 мкм, коэффициент усиления до 10^8 на шевронной сборке, низкий уровень собственных шумов и высокую радиационную стойкость.

2. Конструкция и принцип работы детектора

Детектор установлен на неохлаждаемом участке нуклотрона между линзами 7Д1 и 7Ф2. Перед детектором, по направлению циркуляции пучка, расположена станция внутренних мишеней, что позволяет наблюдать динамику ввода мишеней. Детектор размещен в боксе из нержавеющей стали, который имеет общий вакуумный объем с рабочей камерой ускорителя. Рабочая среда детектора поддерживается вакуумной системой нуклотрона на уровне $5\cdot10^{-7}$ торр.

На рис.1 показана конструкция прибора, функционально разделенная на две части — электростатическую и регистрирующую.

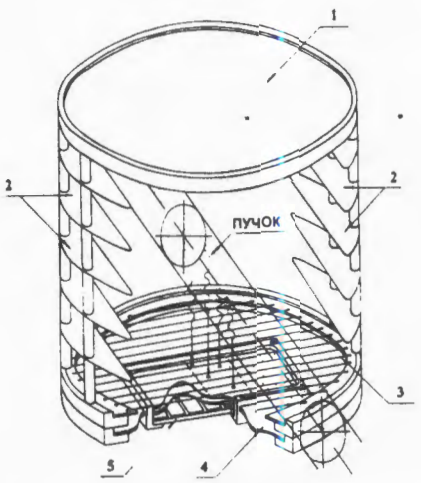

Рис.1. Конструкция прибора. 1 — положительно заряженный электрод; 2 — парные электроды, выравнивающие электростатическое поле; 3 — запирающая сетка; 4 — разрезной отрицательно заряженный электрод, с потенциалом верхней стороны первой МКП

Электростатистическая часть служит для транспортировки ионизированных атомов остаточного газа под действием однородного электрического поля. Она представляет собой группу плоскопараллельных электродов, выполненных из полированной нержавеющей стали, изолированных друг от друга фторопластовыми деталями.

Регистрирующая часть включает в себя шевронную сборку, состоящую из двух микроканальных пластин размером 63x43 мм^2 и позиционно-чувствительный анод. Первоначально анод состоял из восьми прямоугольных электродов — ламелей с размерами 38x6,4 мм^2, перекрывающих чувствительную площадь 2242 мм^2 (59x38 мм^2).

В таблице указаны основные технические параметры детектора. Использование запирающей сетки было предусмотрено на случай больших загрузок (> 10^6 ионов/см^2)

Таблица. Параметры детектора

Электростатическая часть	
Отталкивающий электрод (ОЭ), диаметр	136 мм
Потенциал ОЭ	до +6000 В
Расстояние ОЭ— МКП	111 мм
Расстояние ОЭ — сетка	102 мм
Расстояние сетка — МКМ	9 мм
Запирающий потенциал на сетке	до 400 В
Отрицательнозаряженный разрезной электрод (ОРЭ), диаметр	136 мм
Потенциал ОРЭ	–2500 В
Напряженность поля	до 765 В/см
Шевронная сборка МКМ	
МКМ $(SiO_2)PbO$, размер	63x43 мм^2
Диаметр каналов	0,015 мм
Угол наклона каналов МКМ	7°
Расстояние МКП1—МКП2	0,2 мм
Рабочее напряжение на МКП	1100 В
Позиционно-чувствительный анод	
Чувствительная площадь анода	59x38 мм^2
Захват по координате	59 мм
Расстояние МКП-анод	0,2 мм
Потенциал на аноде	0 В

3. Организация съема сигналов с детектора и считывания данных

Блок-схема электронной аппаратуры представлена на рис.2.

Измерения пространственных характеристик и относительной интенсивности циркулирующего пучка основаны на счете сигналов, снимаемых с электродов детектора $S_1 \ldots S_n$ в программно-задаваемых временных интервалах «ворота».

В ходе предварительных исследований амплитудного спектра сигналов со сборки МКП на вакуумном стенде с α-источником было установлено, что планируемые счетные измерения могут быть реализованы в схеме без использования усилителей указан-

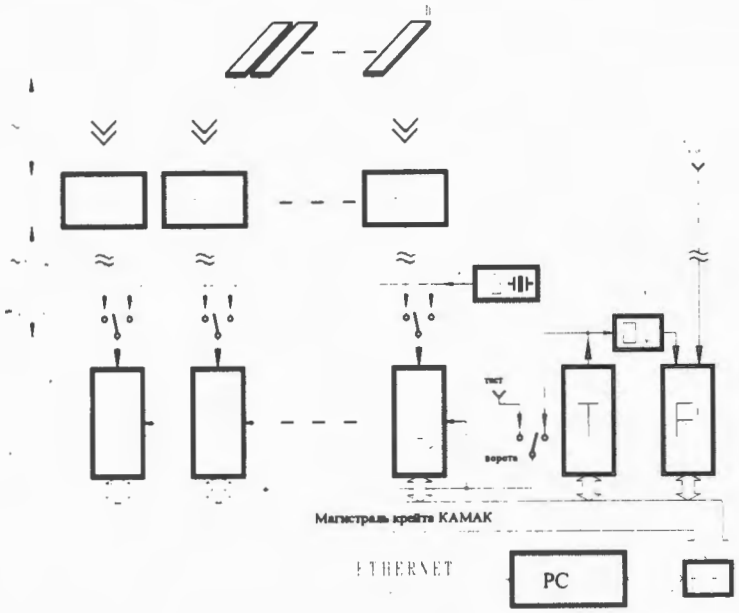

Рис.2. Блок-схема электронной аппаратуры. ОВ — одновибратор, КК — контроллер крейта КАМАК

ных сигналов. При этом сигналы подаются непосредственно на входы формирователей *F*, в качестве которых применяются размещаемые вблизи детектора быстрые амплитудные дискриминаторы типа 4Ф-115 (разработка ЛВЭ ОИЯИ).

Так, для импульсов длительностью ~ 1 нс минимальный порог срабатывания формирователей с учетом разброса по каналам имеет значение (25±5) мВ, что эквивалентно чувствительности схемы к снимаемым с детектора зарядам величиной не менее 0,5 пКл.

Логические сигналы NIM с выходов формирователей поступают по трассе коаксиальных кабелей длиной ~ 60 м на входы счетчиков *S*. Для выработки в каждом цикле ускорителя серии сигналов «ворота», разрешающих входы счетчиков, используется программируемый счетчик-таймер *T*. Временная привязка общего инициирования программы считывания данных к внешнему синхросигналу «начало цикла ускорения» (НЦУ) и каждого опроса счетчиков к спаду сигнала «ворота» осуществляется с помощью входного регистра R. С целью автономной проверки системы обеспечена возможность подключения входов счетчиков к различным по частоте выходам кварцевого генератора G и постоянного разрешения счетчиков уровнем «тест».

4. Обработка получаемой информации и результаты измерений

К моменту написания данной работы система прошла стендовые испытания и успешно эксплуатировалась в четырех сеансах работы нуклотрона.

На рис.3 приведена временная диаграмма профиля пучка с момента инжекции до получения ускоренного циркулирующего пучка.

Эксплуатация системы показала целесообразность увеличения гранулярности анода, что требует увеличения числа каналов. В последнем сеансе работы нуклотрона была произведена модернизация на 16-канальный вариант, при этом пространственное разрешение улучшилось вдвое. На рис.4 представлены соответствующие временные диаграммы.

На рис.4а,б показана временная диаграмма отсчетов при введении в пучок мишени в двух- и трехмерной проекциях. Поскольку детектор расположен за станцией внутренних мишеней по направлению циркуляции пучка, отчетливо виден всплеск интенсивности отсчетов от рассеянных частиц в момент ввода (1,4 с от момента инжекции).

Данные, приведенные на рис.3,4, не нормированы на зависимость величины удельной ионизации от энергии ускоряемого пучка. Измерение абсолютной величины интенсивности пучка в процессе ускорения требует дополнительного изучения.

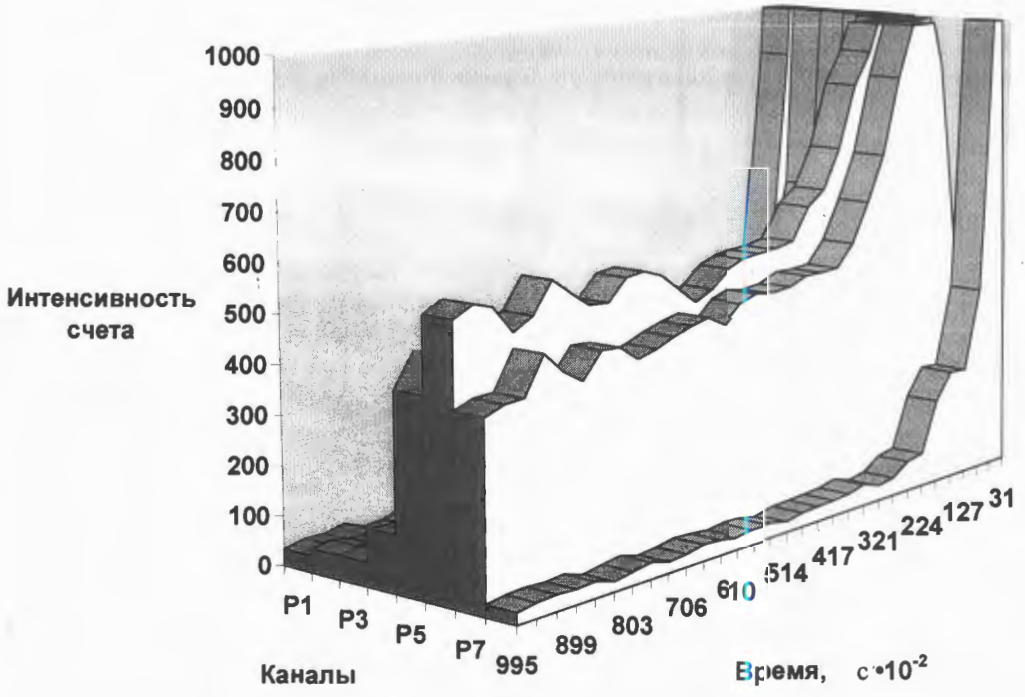

Рис.3. Временная диаграмма профиля пучка с момента инжекции до получения ускоренного циркулирующего пучка

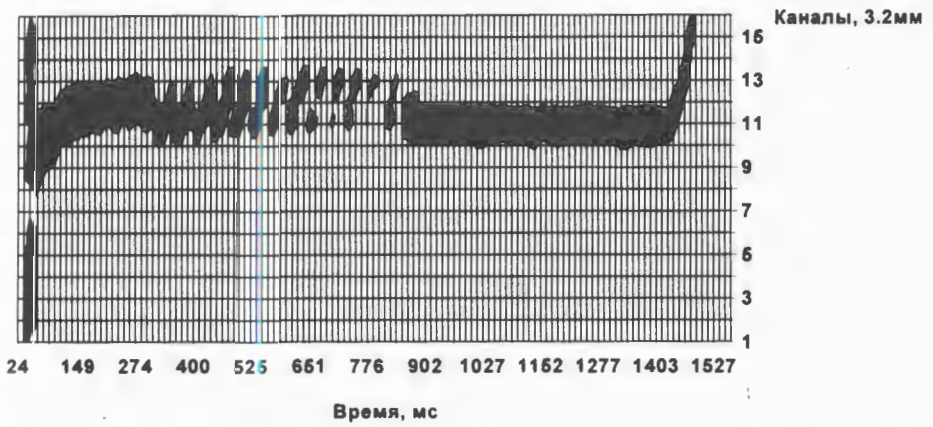

а

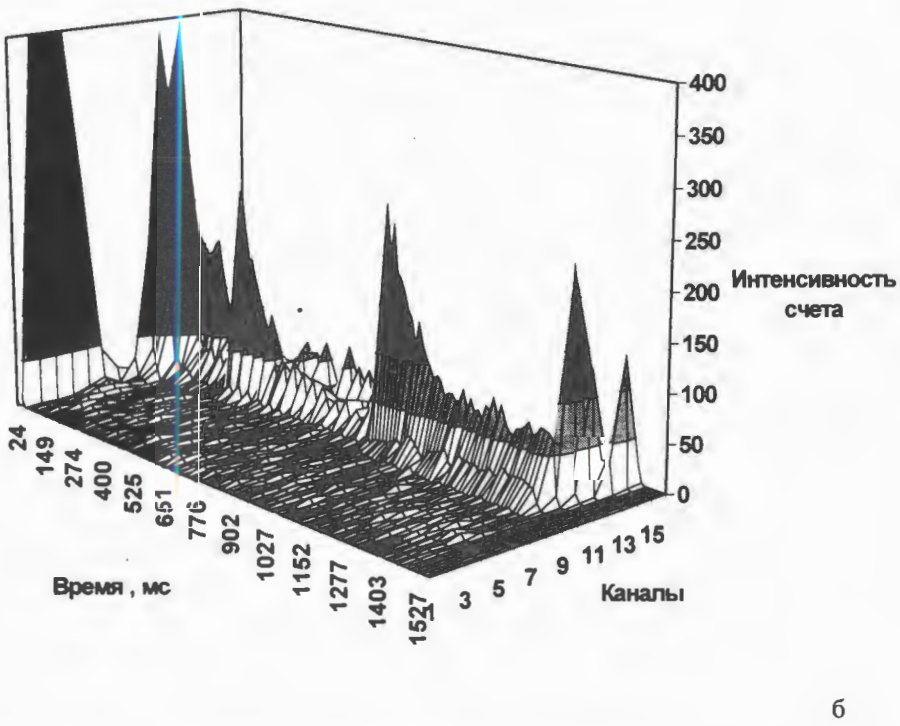

б

Рис.4. Временная диаграмма отсчетов при введении в пучок мишени в двух- (а) и трехмерной (б) проекциях

5. Перспективы развития системы

Возможно поэтапное совершенствование системы для измерения и контроля пространственных характеристик пучка нуклотрона не только в горизонтальной, но и в вертикальной плоскостях, а также увеличение чувствительной области детектора.

Планируется перестройка длительности сигнала «ворота» в широком диапазоне (от 1 мкс до 10 мс), реализуемая путем применения модулей автономного накопления отсчетов в буферных запоминающих устройствах.

Для измерения относительной интенсивности пучков нуклотрона в требуемом диапазоне необходимо при соответствующих режимах работы ускорителя провести детальное исследование процессов ионизации остаточного газа, сбора ионов на МКП и формирование выходных сигналов датчика с изучением их амплитудного спектра.

В плане адаптации описываемой системы к инфраструктуре существующего комплекса автоматизированных средств контроля нуклотрона предусматривается осуществить поцикловый дистанционный вывод получаемых данных через локальную компьютерную сеть на пульт управления ускорителем и представление там цифрографической информации в удобном для принятия решений виде.

6. Благодарности

Авторский коллектив приносит глубокую благодарность А.Д.Коваленко, А.С.Водопьянову, В.И.Волкову, В.А.Мончинскому и Г.Г.Ходжибагияну за поддержку работы и содействие в проведении испытаний системы на нуклотроне.

Особую благодарность авторы выражают А.П.Кобаченко за помощь, оказанную им при разработке детектора, и передачу опыта, накопленного в создании подобных систем.

Считаем также своим приятным долгом выразить искреннюю благодарность П.К.Маньякову, А.Н.Парфенову, Ю.С.Анисимову, В.А.Арефьеву и А.А.Кукушкину за помощь в монтаже и настройке элементов системы.

За полезные обсуждения и возможность использования программы представления информации с детектора на пульте нуклотрона авторы признательны В.М.Слепневу и С.Н.Базылеву.

Авторы выражают благодарность А.Куглеру (ИЯФ, Ржеж, Чехия), а также фонду «Клуб-ФОН», грант № 1-02-07-96, за финансовую поддержку данной работы.

8. Литература

1. Москалев В.А., Сергеев Г.И., Шестаков В.Г. — Измерение параметров пучков заряженных частиц. М.: Атомиздат, 1980, с.4.
2. Сорокин О.М. — ПТЭ, 1982, № 2, с.146.
3. Берковскмй А.Г., Гаванин В.А., Зайдель И.Н. — Вакуумные оптоэлектронные приборы. М.: Радио и связь, 1988, с.85.
4. Kellogg E. et al. — Rev. Sci. Instrum., 1976, Vol.47, No.3, p.282.

5. Грунтман М.А. — ПТЭ, 1984, № 1, с.14.
6. Keller H. et al. — NIM, 1987, Vol.A258, p.221.
7. Lapington J.S. et al. — IEEE Trans. on Nucl. Sci., 1987, Vol.NS-34, No.1, p.431.
8. Lampton M. et al. — Rev. Sci. Instrum., 1987, Vol.58, No.12, p.2298.
9. Williams M.B. and Sobottka S.E. — EEE Trans. on Nucl. Sci., 1989, Vol.36, No.1, p.227.
10. Baldin A.A., Efimov L.G., Feofilov G.A. et al. — JINR Rapid Communications, 1994, No.2[65]-94, p.33.
11. Andreyev A.N. et al. — JINR, Commun. E15-94-471, Dubna, 1994.
12. Feofilov G.A. et al. —NIM, 1995, Vol.A367, p.402.
13. Kawakubo T. et al. — KEK, Preprrint 90-175, Tsukuba, JAPAN, 1991.
14. Buon J. et al — In: Proc. of the First European Workshop on Beam Diagnostics and Instrumentation for Particle Accelerators (Montreux, Switzerland, May 3—5, 1993), CERN PS/93-35 (BD), CERN SL/93—35 (BI), Geneva, 1993, p.166.

Рукопись поступила 16 декабря 1996 года.

УДК 539.1.074

ДЕТЕКТОР ВРЕМЕНИ ПРОЛЕТА ДЛЯ ЭКСПЕРИМЕНТА WA98, ЦЕРН

В.В.Авдейчиков, В.А.Будилов, А.С.Водопьянов, А.П.Ларичева, В.В.Мялковский, В.А.Никитин, П.В.Номоконов, А.В.Павлюк, И.А.Руфанов
Объединенный институт ядерных исследований, Дубна

М.Мартин, Х.Калешовский, Л.Росле
Женевский университет, Женева, Швейцария

Х.Х.Гутброд, Б.Колб, М.Пуршке, Ю.Я.Ли
ГСИ, Дармштадт, Германия

Описан времяпролетный детектор (TOF # 1), являющийся одним из детекторов установки WA98 (ЦЕРН), предназначенной для изучения ядро-ядерных взаимодействий на пучке SPS. Вместе с трековой системой MSAC детектор TOF позволяет идентифицировать частицы по массе в интервале импульсов 1 ÷ 5 ГэВ/с. Детектор состоит из 480 пластиковых сцинтилляторов размерами $480 \times 32 \times 24$ мм^3, каждый из которых просматривается фотоумножителями с обоих торцов. Размеры времяпролетной системы 4×2 м^2. Измеряются как время, так и амплитуды сигналов. Временное разрешение $\sigma = 120$ пс. Описана конструкция детектора, система лазерного контроля, процедуры калибровки и введения коррекций. Приведены иллюстрации идентификации частиц из данных, полученных в 1995, 1996 гг. в сеансах по изучению взаимодействия ядер свинца с энергией $158 \times A$ ГэВ со свинцовой мишенью.

Работа выполнена в Лаборатории высоких энергий ОИЯИ.

Time-of-Flight Detector for WA98 CERN Experiment

V.V.Avdeichikov et al.

The Time-of-Flight detector (TOF # 1) used in WA98 CERN experiment is described. The goal of the experiment is to study Pb-Pb collisions at $160 \times A$ GeV beam of SPS for investigation of highly excited compressed nuclear matter. The MSAC tracking system is backed by TOF wall in order to allow particle identification, i.e., π, K, p separation in the momentum range 1.0 ÷ 5.0 GeV/c. The TOF wall consists of 480 plastic scintillators. The size of each scintillator is $480 \times 32 \times 24$ mm^3. The PMTs are fixed at both ends of scintillators. Full size of TOF wall is 4×2 m^2. The time resolution is $\sigma = 120$ ps. Both time and amplitude of signals of scintillators are measured. There are described the design of the TOF wall, the laser control system, the algorithm of the calibration and finding of time corrections. There are presented the examples of particle identification taken in experiments of Pb–Pb interactions in 1995, 1996.

The investigation has been performed at the Laboratory of High Energies, JINR.

Введение

В данной работе описан один из детекторов эксперимента WA98 (ЦЕРН), предназначенного для исследования высоковозбужденной ядерной материи и поиска ее возможного фазового перехода в кварк-глюонную плазму. Изучаются выход фотонов, нейтральных и заряженных адронов и их корреляции в столкновениях ядер свинца при энергии $158 \times A$ ГэВ. Перечислим основные детекторы установки WA98 (рис.1). Детектор Plastic Ball измеряет множественность и импульсы частиц и легких ядерных фрагментов в основном в области фрагментации мишени. Далее по пучку, недалеко от мишени расположены кремниевый детектор с ячеистой структурой SPMD (Silicon Pad Multiplicity Detector) и кремниевая дрейфовая камера SDC (Silicon Drift Chamber) для регистрации множественности и угловых распределений заряженных частиц в центральной области быстрот. Два калориметра измеряют потоки энергии. Калориметр MIRAC (Mid-Rapidity Calorimeter) измеряет поперечный поток энергии. Калориметр ZDC (Zero Degree Calorimeter) измеряет поток энергии под нулем градусов. Детектор из 10000 модулей свинцового стекла LEDA (Lead-Glass Calorimeter) позволяет получить данные по выходу π^0- и η-частиц в широкой области быстрот и поперечных импульсов, покрывающих как область тепловой генерации фотонов, так и жесткого рассеяния и, таким образом, определить отношение выхода тепловых и прямых фотонов к выходу π^0. Preshower (предливневый) детектор множественности фотонов PMD (Photon Multiplicity Detector) позволяет из сравнения с множественностью заряженных

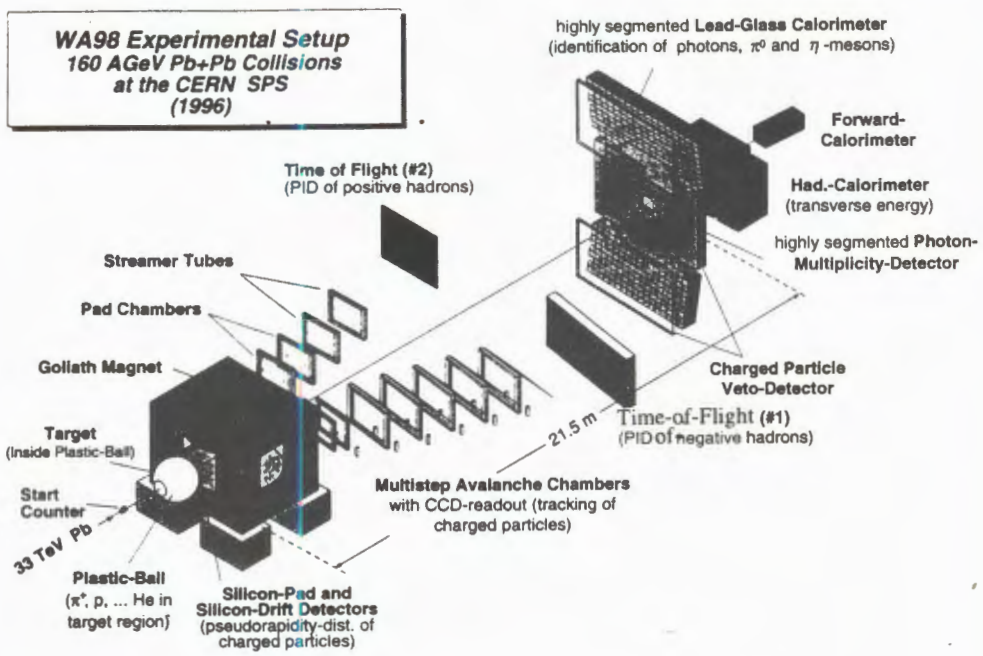

Рис.1. Расположение детекторов установки WA98

частиц определить класс событий с аномальным выходом фотонов. Два плеча трековых детекторов и детекторов времени пролета с меньшим аксептансом служат для измерения импульсов и идентификации заряженных частиц обоих знаков. Сравнением отношения сечений и импульсных распределений хорошо идентифицированных частиц (π^{+-}, K^{+-}, p, $\bar{p}$) можно изучать степень термализации и химического равновесия возбужденной системы. Измеряя корреляционные функции тождественных адронов, можно определить размер источника испускания частиц. Сигналы калориметров MIRAC и ZDC вместе с сигналами пучковых и вето-счетчиков служат для выработки триггерных сигналов с различными величинами параметра соударения ядер. Для определения импульса заряженных адронов в эксперименте WA98 используется магнит «Goliath» с зазором 1600 мм по вертикали. Величина $B \times L = 2$ Тл·м сообщает заряженным частицам поперечный импульс около 0,6 ГэВ/с. В сеансах 1994 и 1995 работало одно трековое плечо MSAC (MultiStep Avalanche Chambers), в конце которого находилась времяпролетная система. Основная статистика получена при направлении магнитного поля, когда на MSAC отклонялись отрицательные частицы. В 1996 установка WA98 была дополнена еще одной трековой и времяпролетной системой для регистрации положительных частиц. Новая трековая система состоит из двух камер с ячеистой структурой и двух плоскостей дрейфовых трубок. Времяпролетная система в правом плече, расположенная в конце трековой системы MSAC, изготовлена в Объединенном институте ядерных исследований в Дубне. В коллаборации WA98 эта система называется TOF # 1 (Time-of-Flight). Времяпролетная система, расположенная в левом плече, изготовлена в Японии и называется TOF # 2. В данной работе описывается времяпролетная система, которая работает с трековой системой MSAC, то есть TOF # 1. MSAC состоит из 6-ти многоступенчатых лавинных камер, расположенных вне магнитного поля. Первая камера находится на расстоянии 6 м от мишени. Расстояние между камерами 1,4 м. Размеры камер 1,2 × 1,6 м. Около 10% всех заряженных частиц от центральных столкновений проходят через апертуру камер. Измерение имульса производится с разрешением $\Delta P / P = 0{,}003 \times P$ (где P — в ГэВ/с). Подробное описание детекторов установки можно найти в работе [1], а описание трековой системы в работе [2]. В конце трековой системы MSAC на расстоянии около 17,6 м от мишени расположен детектор TOF # 1. Измерение времени пролета вместе с измерением импульса частиц трековой системой позволяет идентифицировать заряженные частицы по массе (π^{+-}, K^{+-}, p, $\bar{p}$ и легкие ядра).

В 1994–1996 гг. проведены три сеанса по исследованию столкновений ядер свинца с энергией 158 × A ГэВ с ядерными мишенями. Наибольшая статистика набрана на свинцовой мишени. Иллюстрации идентификации частиц, приведенные в этой работе, получены на основе экспериментальных данных сеансов 1995 и 1996 гг. на пучке Pb 158 × A ГэВ.

Конструкция и характеристики времяпролетной системы WA98

Общий вид времяпролетной системы показан на рис.2. Это стенка, размером 4 × 2 м^2, состоящая из 480 пластмассовых сцинтилляторов, расположенная на расстоянии 17,6 м от мишени. Она полностью перекрывает апертуру трековой системы MSAC.

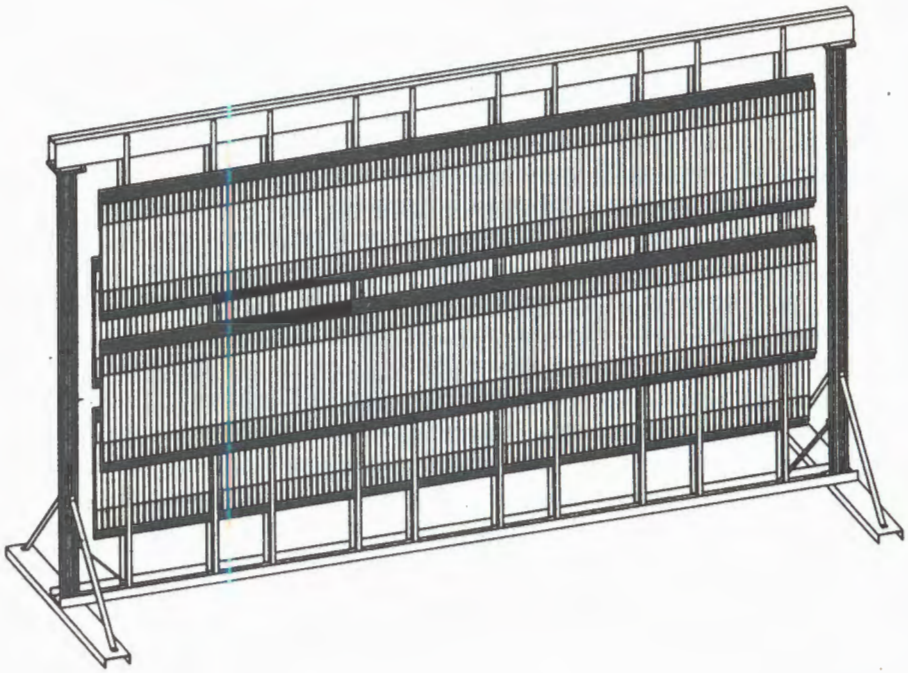

Рис.2. Общий вид системы времени пролета (TOF # 1)

Элемент детектора времени пролета показан на рис.3. Сцинтилляторы на основе полистирола изготовлены в ОИЯИ методом блочной полимеризации и последующей механической обработкой. По характеристикам сцинтиллятор близок к известному типу NE110 или BC412. Размер каждого сцинтиллятора 480 × 32 × 24 мм^3. Толщина сцинтиллятора по пучку 24 мм. Высота — 480 мм. Каждый сцинтиллятор просматривается фотоумножителями с обоих торцов. Это позволяет определить координату попадания частицы в сцинтиллятор, измеряя разность времени прихода световых импульсов к торцам сцинтиллятора. Полусумма этих величин дает временную отметку, не зависящую от координаты. Сцинтилляторы отполированы и обернуты черной бумагой. Использованы фотоумножители XP2972, демонтированные из калориметра эксперимента WA70 (ЦЕРН). Характеристики этих фотоумножителей подробно описаны в работе [3].

Тип фотокатода	bi-alkaline D(Sb K Cs)
Полезный диаметр фотокатода	23 мм
Число ступеней усиления	10
Материал динода	CuBeO
Время нарастания анодного импульса при 1800 В	1,9 нс
Время распространения сигнала в ФЭУ при V = 1500 В	23 нс
Длительность анодного импульса на полувысоте при 1800 В	3,0 нс

Анодные сигналы используются для измерения амплитуды импульсов, а динодные сигналы — для запуска дискриминаторов, сигналы от которых являются стартовыми сигналами для измерения времени пролета. Для удобства механического крепления сцинтилляторы собраны в 20 модулей. Каждый модуль состоит из 24 сцинтилляторов, к торцам которых приклеены фотоумножители. Компактные делители высокого напряжения для питания динодов с помощью сварки соединены с ножками фотоумножителей. Фотоумножители обернуты магнитным экраном. Для уменьшения шумов на магнитные экраны подается высокое напряжение, близкое по величине к напряжению фотокатода. Сцинтилляторы с фотоумножителями закреплены на листе из оргстекла толщиной 6 мм. На этом же листе закреплены разъемы для высоковольтного питания фотоумножителей и разъемы, на которые выведены анодные и динодные сигналы. Всего на каждом модуле находятся 3 разъема для высоковольтного питания (16 каналов на каждом), 8 разъемов типа BURNDY для динодных сигналов (по 6 на каждом) и 4 разъема для анодных сигналов типа AMP (по 12 на каждом). Для высоковольтного питания фотоумножителей использовалась многоканальная система LeCroy 1440. Дискриминаторы и схемы перекрытия выполнены в стандарте NIM. Они применялись ранее в эксперименте WA70 и подробно описаны в работе [3]. Крейты с дискриминаторами располагаются рядом с времяпролетной системой. В каждом модуле NIM находится 18 дискриминаторов. На передней панели блока дискриминаторов расположены коаксиальные разъемы NIM для выходных импульсов. Входные кабели длиной около 4-х метров подпаиваются непосредственно внутри блока. Они выходят через отверстия в задней панели блока и объединены в 3 группы по 6 кабелей. Каждая группа заканчивается разъемом BURNDY. Дискриминаторы имеют регулируемый порог от 1 до 10 мВ. В эксперименте WA98 устанавливались максимально возможные значения порогов — 10 мВ. Высокое напряжение на фотоумножителях подбиралось таким образом, чтобы сигналы от релятивистской частицы, прошедшей через середину сцинтиллятора, имели на 50 Ом анодной нагрузке амплитуду около 150 мВ. Величины высокого напряжения на фотоумножителях варьируются в диапазоне 1500 + 1800 В. Сигналы с выходов дискриминаторов и анодные сигналы по коаксиальным кабелям длиной 108 м приходят в помещение, где располагаются крейты NIM со схемами перекрытия (конверторы время — заряд) и разветвителями сигналов «общий стоп», крейты КАМАК с АЦП для измерения зарядов анодных сигналов и зарядов сигналов от схем перекрытия. Схема перекрытия («overlap units») вырабатывает сигнал постоянной стабильной амплитуды с длительно-

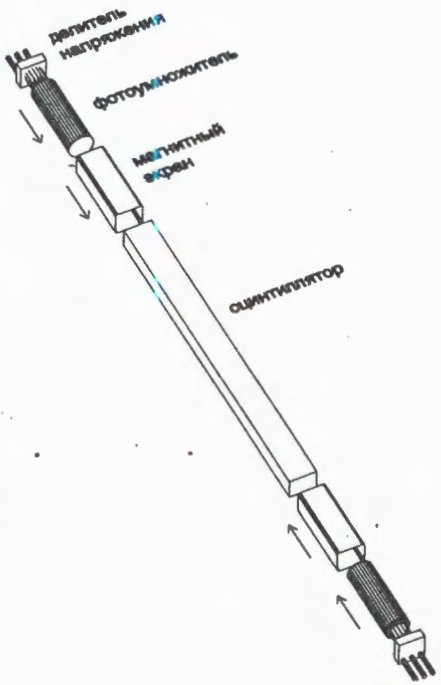

Рис.3. Один из элементов детектора времени пролета: сцинтиллятор, фотоумножители, магнитные экраны

стью, определяемой интервалом времени между срабатыванием дискриминатора динодного импульса и сигналом «общий стоп», вырабатываемым пучковым счетчиком. В каждом модуле находится 24 канала. Для измерения как анодных сигналов, так и сигналов от схем перекрытия используется система LeCroy CAMAC ADC 2280. В модуле ADC единичной ширины находится 48 измерительных каналов. Для 1960 измерительных каналов системы времени пролета используются 40 модулей ADC, расположенных в трех крейтах КАМАК.

Счетчик сигнала «общий стоп»

Сигнал «общий стоп» вырабатывается азотным черенковским счетчиком, который располагается на расстоянии около 3 м от мишени в направлении, противоположном направлению пучка. На пучке ядер свинца количество света в газовом счетчике оказывается таким большим, что позволяет получить собственное временное разрешение около 40 пс. Азот находится при атмосферном давлении. В счетчике взаимодействует около 0,5% пучка. Поскольку счетчик работает в условиях больших загрузок, используется подпитка последних динодов фотоумножителя отдельным источником высокого напряжения. Преимуществом газового черенковского счетчика является также отсутствие радиационных повреждений.

Лазерная система контроля

Работоспособность и стабильность системы времени пролета контролировалась с помощью импульсного азотного лазера (PRA Laser, Inc., Model LN100). Длина волны испускаемого света — 337 нм, длительность импульса меньше 1 нс. Для транспортировки света от лазера использовались кварцевые волоконные световоды, прозрачные для ультрафиолета. Свет от лазера сначала расщепляется в два длинных световода диаметром 1 мм, один из которых подходит к фотоумножителю пучкового стартового счетчика, а второй поступает к распределителю света на 960 каналов, расположенному около системы времени пролета. Двухступенчатый распределитель света сделан из свернутой в трубочки алюминиевой фольги. Кварцевый световод толщиной 1 мм подходит от лазера к трубке диаметром 25 мм и длиной 150 мм. На другом конце этой трубки находятся торцы 60 кварцевых световодов диаметром 0,3 мм и длиной 0,6 м. Каждый из этих световодов подходит к второй ступени распределителя света — трубке диаметром 4,5 мм и длиной 60 мм. С противоположных концов этих трубок выходят по 22 световода, каждый из которых подведен к своему фотоумножителю. Диаметр фотокатода на несколько миллиметров больше толщины пластика, так что каждый световод торцом упирается непосредственно в фотокатод. В конечном счете к каждому фотоумножителю подходит световод 0,3 мм с лазерным светом. Лазерная система служит, в основном, для проверки стабильности всех трактов во времени (особенно выявления медленного дрейфа), правильности занесения пьедесталов в память контроллера ADC 2280 и для определения временной шкалы ADC пс/канал. Абсолютная калибровка каналов с помощью лазерной системы в нашем случае не обладает достаточной

точностью, поскольку длины кварцевых световодов не имеют строго одинаковой длины. Иногда для группы облучений наблюдается смещение на большую постоянную величину. Этот эффект проще всего объяснить неправильной записью пьедесталов в систему 2280. Процедура обновления пьедесталов обычно проводилась один раз в несколько дней.

Внутреннее временное разрешение системы времени пролета

Внутренним временным разрешением назовем временное разрешение, которое определяется фотоумножителями и электроникой при световом импульсе лазера таком же, как от частиц в сцинтилляторе. Средняя величина временного разрешения каждого канала от лазера — около 90 пс. Вклад в ухудшение разрешения вносят как фотоумножители, так и электроника (в основном, схема перекрытия). Схемы перекрытия обладают внутренним шумом, и в некоторых каналах наблюдались осцилляции, сильно ухудшающие временное разрешение. Для устранения эффекта осцилляций нами была проведена небольшая модификация схем перекрытия. Тем не менее проверка от генератора схем перекрытия показала широкий разброс их собственного временного разрешения (от 25 до 80 пс). Вклад от стартового счетчика — около 40 пс, и он может быть учтен вычитанием измеренных времен от любой пары фотоумножителей (удобно сравнить сумму и разность).

Определение временной цены канала АЦП пс/канал с помощью лазера

Для определения цены каждого канала АЦП в единицах времени (пс/канал) во всем динамическом диапазоне проводилась калибровка с помощью лазерных сигналов. В тракте сигнала «общий стоп» автоматически изменялась задержка с шагом 1 нс. Эта процедура проводилась в течение нескольких часов один или два раза за сеанс. Временные спектры от одного из фотоумножителей со сдвигом 1 нс показаны на рис.4. Для каждого канала был сделан линейный фит зависимости показаний АЦП от переменной величины задержки в динамическом диапазоне около 80 нс. Таким образом для каждого тракта определяются два параметра: сдвиг и ширина канала. Средняя ширина канала всех трактов — около 20 пс/канал. Разброс средних значений по 960 каналам *RMS* ≈ 1,1 пс.

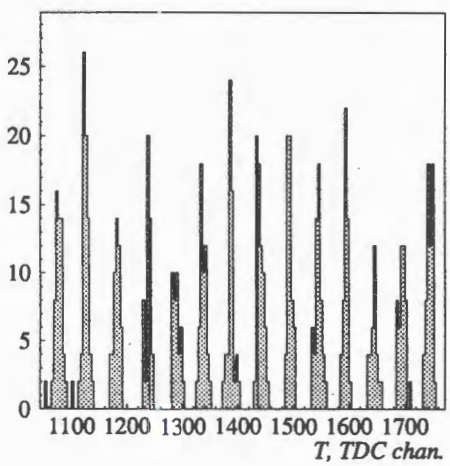

Рис.4. Временной спектр, полученный от одного из фотоумножителей при сканировании TOF лазером с шагом задержки в тракте сигнала «общий стоп» 1 нс

Как выглядят амплитуды сигналов от заряженных частиц в сцинтилляторе

Были использованы сцинтилляторы без световодов длиной 480 мм. Длина затухания в нашем случае определяется в основном качеством полировки и в меньшей степени прозрачностью сцинтиллятора. Ее величина варьируется от 500 мм до 250 мм. Амплитуда почти экспоненциально изменяется в зависимости от расстояния до фотокатода. Распределение амплитуд сигналов от двух концов сцинтиллятора показано на рис.5. Между величиной логарифма отношения амплитуд и разностью времен прихода сигналов к противоположным концам пластика существует линейная зависимость. На рис.6 показана двумерная гистограмма этих величин для одного из пластиков, полученная во время экспозиции на пучке свинца. Из этого распределения можно оценить внутреннее разрешение системы времени пролета без учета стартового счетчика. Типичная величина разрешения — около 120 пс. Помимо сигналов от заряженных адронов в спектрах присутствуют сигналы малых амплитуд. Возможно, что это — смесь сигналов от нейтронов, гамма-квантов и дельта-электронов.

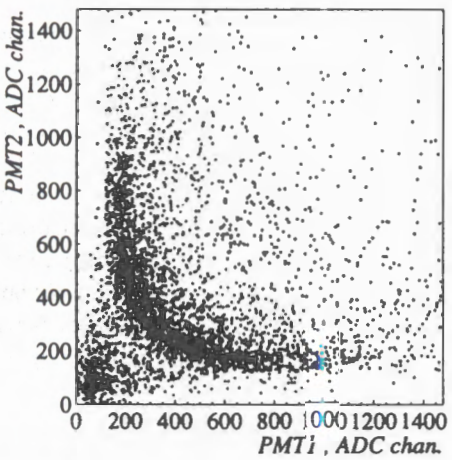

Рис.5. Распределение амплитуд сигналов от двух концов сцинтиллятора

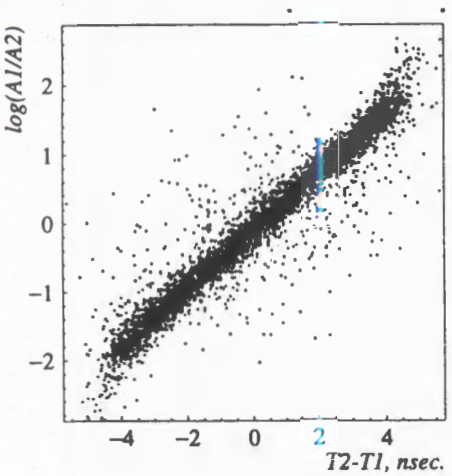

Рис.6. Двумерная гистограмма разности времен и логарифма отношения амплитуд от двух концов сцинтиллятора

Определение *Y*-координаты

X-координата определяется позицией сцинтиллятора. *Y*-координату можно определить как по разности временных сигналов, так и из отношения амплитуд с двух концов сцинтиллятора. Распределение разности временных сигналов показано на рис.7. Длина пластика — 480 мм. На этой длине распределение по *Y* должно быть однородным, т.е. плоским. Для каждого пластика были набраны аналогичные спектры и получены параметры левой и правой границы распределения на уровне 1/3 от плоской вершины распределения. *Y*-координата вычисляется как

$y = y_0 + (t_1 - t_2) \times K$, где параметры y_0 и K — индивидуальные для каждого сцинтиллятора. Эффективная скорость распространения светового сигнала в сцинтилляторе в нашем случае — около 112 мм/нс. Она определяется как коэффициентом преломления, так и эффективным углом полного внутреннего отражения и приблизительно равна $v \approx c \times \cos(a)/n \approx c/n^2$. Поскольку не были использованы световоды, то для событий, когда частица прошла через сцинтиллятор вблизи фотокатода, эффективная скорость распространения светового сигнала до него несколько увеличивается. Эта небольшая нелинейность находится из экспериментальных спектров и корректируется при дальнейшей обработке.

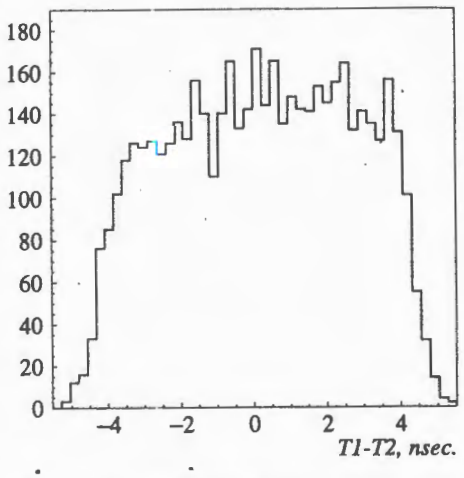

Рис.7. Распределение разности времен от двух концов сцинтиллятора

Заметим, что при одновременном попадании двух частиц в сцинтиллятор, сохраняется линейная зависимость между разностью времен прихода сигналов к концам сцинтиллятора и логарифмом отношения амплитуд. При этом полученная *Y*-координата соответствует середине между точками попадания.

Стыковка трековой системы MSAC и системы времени пролета

На рис.8 показано двумерное распределение величин разностей между координатами проекций трека MSAC на TOF и координатами попадания частицы в TOF, определяемыми из позиции сработавшего пластика и разности времен сигналов с двух его противоположных торцов. Пространственное разрешение $\sigma_X = 17$ мм определяется размерами пластика по *X*-координате (33 мм). Разрешение $\sigma_Y = 20$ мм определяется временным разрешением TOF и координатным разрешением трековой системы MSAC. Считаем, что трек в MSAC и сцинтилляция в TOF порождены одной частицей, если расстояние между точкой, полученной из экстраполяции трека MSAC на TOF, и точкой попадания частицы, найденной из данных TOF, меньше некоторой заданной величины (25 + 35 мм). Пространственная стыковка геометрии TOF и MSAC проводилась для каждого из 20 модулей TOF отдельно. Это позволило найти отклонения в позиции каждого модуля и внести их в описание геометрии. Величины этих отклонений не превышают нескольких мм.

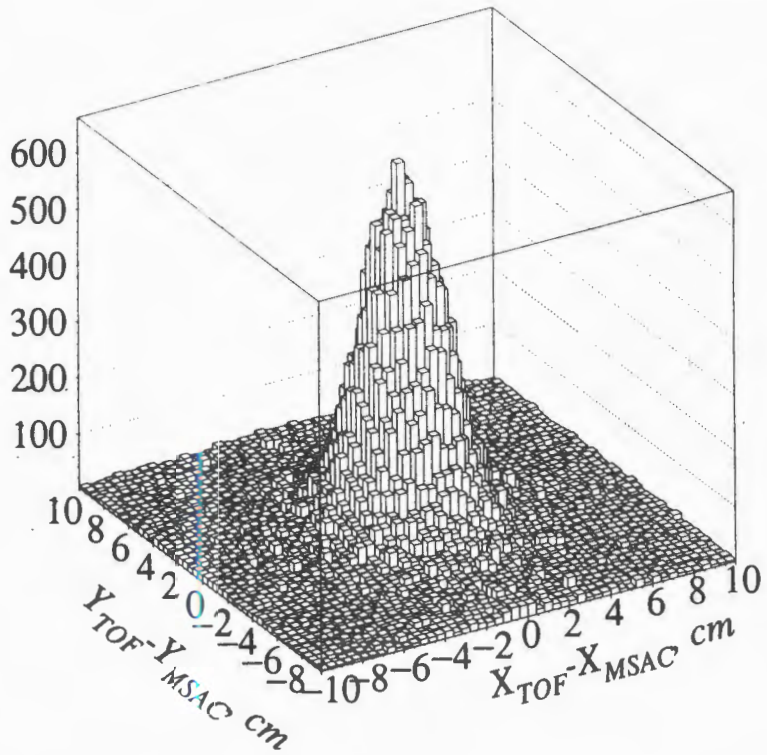

Рис.8. Распределение для разностей $X_{TOF} - X_{MSAC}$ и $Y_{TOF} - Y_{MSAC}$ координат, определенных по данным MSAC и TOF

Коррекция, связанная с величиной амплитуды сигнала

Поправка на зависимость времени срабатывания дискриминатора от амплитуды импульса существенна для малых амплитуд. Мы использовали амплитудную коррекцию, одинаковую для всех измерительных трактов

$$\Delta t = K / \text{номер канала ADC}.$$

Коэффициент «K» в этой формуле находится экспериментально так, чтобы не было зависимости от амплитуд на двумерных гистограммах

$$\{(t_{up} + t_{down}), A_{up}\} \quad \text{и} \quad \{(t_{up} + t_{down}), A_{down}\}.$$

В этом выражении t_{up}, t_{down}, A_{up}, A_{down} — времена и амплитуды сигналов на верхних и нижних торцах сцинтилляторов.

Если предположить, что величина напряжения на входе дискриминатора линейно нарастает во времени, то момент срабатывания дискриминатора

$$t = t_0 + t_{\text{front}} \times \text{threshold} / \text{amplituda}.$$

Эмпирически находится параметр $K = t_{\text{front}} \times \text{threshold}$. В нашем случае получается, что для оптимальной величины параметра K и порога дискриминатора 10 мВ длительность переднего фронта импульса — около 2,5 нс, что близко к его действительному значению.

Коррекция времени, связанная с *Y*-координатой сцинтиллятора

Как уже упоминалось выше, мы не использовали световоды, а сцинтиллятор приклеивался оптическим эпоксидным клеем непосредственно к фотоумножителю. При прохождении частицы через сцинтиллятор ближе 3–4 см от края возрастает вклад света, распространяющегося под углами, меньшими угла полного внутреннего отражения. Таким образом, у краев в направлении ближайшего фотокатода эффективная скорость распространения светового сигнала увеличивается. Чтобы ввести коррекцию на этот эффект, набираются двумерные гистограммы разности времен T_{TOF} (время, измеренное TOF) и T_{MSAC} (время пролета, вычисленное из данных MSAC в предположении, что частица — пион) $\{(T_{\text{TOF}} - T_{\text{MSAC}}), Y\}$. *Y*-координата берется из данных MSAC. На основании этих спектров делается коорекция времени пролета в зависимости от *Y*-координаты. Вес этой поправки невелик в силу того, что она имеет значимую величину не более чем для 10% попаданий в пластик.

Коррекция на медленный дрейф

Поскольку лазерный контроль охватывает как фотоумножитель пучкового стартового счетчика, генерирующего сигнал «общий стоп», так и все индивидуальные каналы, то он является эффективным средством наблюдения за медленным временным дрейфом, связанным с измерением температуры или деградацией фотоумножителей и электроники. После каждого цикла ускорения во все каналы записывается один или несколько лазерных импульсов. Таким образом можно контролировать каждый канал. В основном поправки невелики, но иногда в некоторых каналах что-то случается, чему трудно найти объяснение. В частности, большие отклонения в некоторых трактах можно объяснить сбоями при записи пьедесталов в контроллер ADC 2280. Запись пьедесталов проводится во время сеанса один раз в несколько дней. Величины дрейфа, измеренные с помощью лазера и по спектрам частиц (отслеживается дрейф центра распределения $T_{\text{TOF}} - T_{\text{MSAC}}$), показывают согласие, но, конечно, по лазерным данным дисперсия намного меньше. Для внесения коррекций на медленный дрейф для каждого канала распределения времен от лазерного сигнала в зависимости от номера облучения сглаживаются, и полученные значения заносятся в базу данных.

Абсолютная временная калибровка системы времени пролета

Окончательная калибровка каждого временного канала проводится по экспериментальной информации, полученной на основе анализа треков MSAC. На основе анализа длины трека и величины импульса вычисляем время пролета в предположении, что частица — пион и гистограммируем разности между вычисленным значением времени пролета и временем, измеренным в TOF после введения лазерной калибровки и всех вышеупомянутых поправок. Поскольку больше 90% частиц являются отрицательными пионами, то такая калибровка вполне корректна. Находим центр каждого распределения. Найденные значения помещаем в базу данных и используем в дальнейшем для нахождения времени пролета частицы для каждого трека. Итак, теперь время вычисляется как

$$t = t_{\text{las calib}} + \Delta t_{\text{slow drift}} + \Delta t_{\text{MSAC}},$$

где $t_{\text{las calib}}$ — величина, полученная из показаний ADC и приведенная по результатам лазерной калибровки к реальной временной шкале;

$\Delta t_{\text{slow drift}}$ — поправка на медленный дрейф электроники. Эта поправка определяется для каждого номера облучения;

Δt_{MSAC} — основная калибровочная поправка, полученная из сравнения времени пролета пионов по данным трековой системы MSAC и времени, измеренного в TOF.

Эта процедура требует достаточно большой статистики и несколько осложняется из-за наличия фона.

Проблема фона для абсолютной калибровки TOF

Одной из причин, ухудшающих идентификацию частиц, является неточная калибровка каналов, связанная с фоном частиц, которые дают временную отметку раньше, чем пионы, вылетевшие из мишени. Это могут быть вторичные частицы, как электроны, так и пионы, вылетающие из вещества, расположенного на пути летящих из мишени частиц. Поскольку при восстановлении трека производится экстраполяция через магнитное поле в мишень, то для частиц, вылетающих не из мишени, длина траектории и величина импульса определяются неверно. В сеансе 1995 года одним из источников такого фона была вакуумная труба для проводки непровзаимодействовавшего пучка, которая начиналась примерно в центре магнита. При выключенном магнитном поле, когда треки прямые, изображение этой трубы

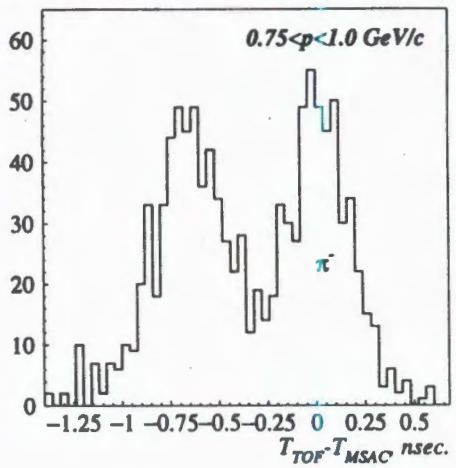

Рис.9. Разность времен, измеренных TOF и вычисленных из данных MSAC в предположении, что частица является пионом. Правый максимум относится к пионам, вылетевшим из мишени, левый — к фоновым частицам

хорошо видно. Чтобы избежать ошибок, связанных с фоном, процедура калибровки на пионы делается следующим образом. Для каждого сцинтиллятора набирается гистограмма разности между временем, измеренным TOF, и временем, вычисленным по данным MSAC, в предположении, что все частицы — пионы и вылетают из мишени. Пример такого распределения показан на рис.9. Полученное распределение фитируется суммой двух гауссовских распределений. Величины центров пика, которые относятся к пионам, вылетевшим из мишени, заносятся в базу данных и используются в дальнейшем анализе.

Описание процедуры вычисления времени пролета

Суммируя все вышесказанное, перечислим кратко, как из показаний ADC вычисляется время пролета.

1) Переводим показания ADC в реальную временную шкалу, используя параметры, полученные при сканировании всех трактов лазерным сигналом с шагом 1 нс.

2) Вводим коррекцию, связанную с зависимостью от амплитуды сигнала.

3) Добавляем поправку, связанную с макровременем. Для каждого тракта и каждого номера облучения эти величины находятся как сдвиг временной позиции лазерного репера, усредненный в каждом облучении.

4) Вычисляем полусумму времен с обоих концов сцинтиллятора и вводим коррекцию, связанную с изменением скорости распространения сигнала у концов сцинтиллятора.

5) Добавляем поправку, найденную из калибровки на пионы при сравнении времен, вычисленных из данных MSAC и измеренных TOF.

Иллюстрации идентификации частиц

Приведем иллюстрации идентификации частиц на основе экспериментального материала, полученного при взаимодействии ядер свинца с энергией $158 \times A$ ГэВ со свинцовой мишенью в сеансах 1995, 1996 гг. После нахождения соответствия трека в MSAC и сцинтилляции в TOF для каждого трека известны величина импульса, длина траектории от мишени до попадания в TOF и время пролета. Из этих величин определяется масса частицы. На рис.10 показаны двумерные гистограммы времени пролета в зависимости от величины импульса, определяемого трековой системой. Приведены данные как для положительных, так и для отрицательных частиц, полученные при противоположных знаках магнитного поля. Время пролета для всех треков приведено к одной длине траектории 17,6 м.

Недостатки, замеченные в работе TOF

Основным обнаруженным дефектом работы TOF являются перекрестные наводки канала на канал. Они вызваны неудачным выбором разъемов (BURNDY) для соединения динодных выходов с входами дискриминаторов. В разъеме проходит несколько см неэкранированного тракта, и этого оказалось достаточным для того, чтобы вызвать срабатывание дискриминатора в соседнем канале, начиная с какой-то величины амплитуды. При этом величина амплитуды, измеряемая в анодном тракте, остается нулевой.

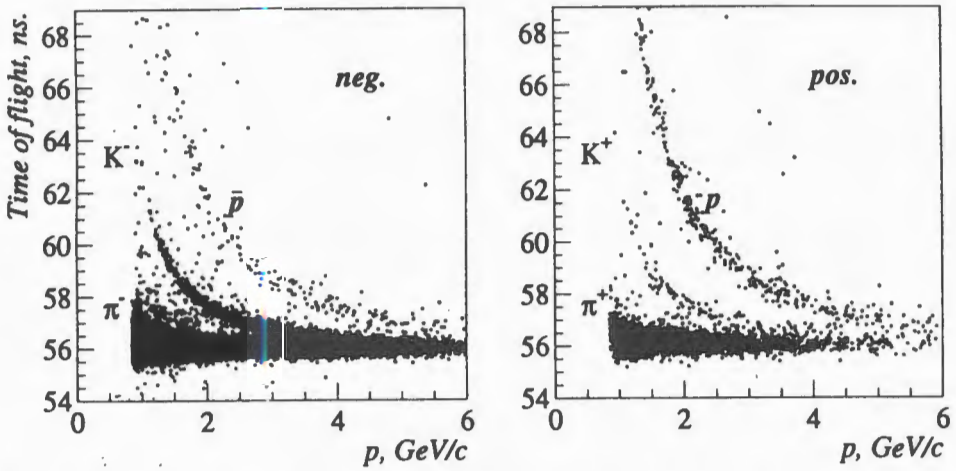

Рис.10. Распределение времени пролета в зависимости от импульса. Распределения для отрицательных и полохительных частиц получены при противоположных знаках магнитного поля магнита «Goliath»

Низкие пороги 10 мВ (которые максимальны для данной системы) фактически были еще ниже из-за шумов, смещающих базовую линию на входе дискриминаторов. Особенностью этой наводки является то, что она вызывает срабатывание соседнего дискриминатора с задержкой примерно на 8 нс. Таким образом, мы имеем искажение информации для медленных частиц, если в соседний канал попала какая-то частица. Этот эффект довольно легко учесть, но он приводит к потере статистики около 15%.

Заключение

Авторы выражают благодарность академику А.М.Балдину за поддержку работы, коллективам химиков Лаборатории высоких энергий и Лаборатории ядерных проблем за варку сцинтиллятора, коллективу экспериментальных мастерских Лаборатории высоких энергий за большую работу по механической обработке сцинтиллятора, П.К.Маньякову за консультации по модификации электроники, а также всему коллективу эксперимента WA98, и прежде всего А.Прзыбыла за большую помощь в монтаже и эксплуатации системы времени пролета.

Литература

1. CERN/SPSLC 91-17, SPLC/P260, May, 1991;
   Peitzmann T. et al. — Nucl. Phys., 1996, v.A610, p.200.
2. Angelis A.L.S. et al. — Nucl. Phys., 1994, v.A566, p.605.
3. Bonesini M. et al. — Nucl. Instr. and Meth., 1988, v.A263, p.325; 1988, v.A264, p.205.

Рукопись поступила 5 марта 1997 года.

УДК 538.971

ОБРАЗОВАНИЕ ФРАКТАЛЬНЫХ СТРУКТУР НА ПОВЕРХНОСТИ МАТЕРИАЛОВ, ОБЛУЧАЕМЫХ СИЛЬНОТОЧНЫМИ ЭЛЕКТРОННЫМИ И ИОННЫМИ ПУЧКАМИ

М.В.Алтайский, В.В.Иванов, С.А.Коренев, О.Л.Орелович, И.В.Пузынин, В.В.Черник

Обсуждаются результаты обработки микрофотографий поверхностей веществ, облученных импульсными сильноточными электронными и ионными пучками. Показано, что на облучаемой поверхности могут образоваться фрактальные структуры. Их размерности определены с помощью box-counting алгоритма.

Работа выполнена в Лаборатории вычислительной техники и автоматизации ОИЯИ.

Fractal Structure Formation on the Surfaces of Solids Subjected to High Intensity Electron and Ion Treatment

M.V.Altaisky et al.

We discuss the results of scanning electron microscopy of surfaces of the solids subjected to high intensity electron and ion beam treatment. The appearance of fractal structures on the modified surfaces is shown. The fractal dimensions of these structures were estimated by box-counting algorithm.

The investigation has been performed at the Laboratory of Computing Techniques and Automation, JINR.

Введение

Поверхностная модификация материалов сильноточными электронными и ионными пучками находит широкое применение в высоких технологиях [1,2]. Однако, несмотря на обилие экспериментального материала, механизм взаимодействия интенсивных пучков с поверхностью твердого тела еще не до конца ясен. Понимание процесса изменения морфологии поверхности облучаемых образцов может дать ключ к построению физической модели, которая, с одной стороны, может объяснить наблюдаемые результаты, а с другой — позволит контролировать процесс формирования поверхностного слоя. Последнее обстоятельство особенно важно для практического применения.

При облучении материалов импульсными сильноточными электронными и ионными пучками наблюдаются как структурно-фазовые изменения, так и изменения морфологии поверхностного слоя, толщина которого зависит от кинетической энергии

частиц пучка. Вместе с тем, результаты исследований в области физики конденсированных сред, в частности, формирования конденсированной системы в неравновесных условиях [3], когда образуемое вещество представляет собой не сплошную среду, а пористые фрактальные структуры, позволяют по-новому подойти к вопросам морфологии поверхности образцов, облучаемых электронными и ионными пучками. Кроме того, развитие современных методов вычислительной физики [4] позволяет применить новые подходы для решения рассматриваемой проблемы.

В настоящей работе обсуждается новый механизм формирования фрактальных структур в поверхностном слое твердого тела, облучаемого сильноточными электронными и ионными пучками. Приводятся результаты численного анализа фрактальных структур для различных образцов.

1. Механизм образования получения фрактальных структур при облучении импульсным пучком

В настоящее время известно несколько методов получения фрактальных структур на поверхности твердых тел:

— электрический взрыв проволоки [5];
— нагревание вольфрамовой спирали в вакууме [6];
— взрыв материала [7];
— сжигание SiH [8];
— лазерное облучение металлов [9,10].

В последнем случае, при облучении образца лазерным излучением вблизи поверхности образуется слабоионизированный пар металла, который, расширяясь в пространство, вначале охлаждается, а затем конденсируется на ионах. Когда температура образующихся частиц становится меньше температуры плавления материала, частицы металла кластеризуются, образуя фрактальные структуры в поверхностном слое облучаемого металла.

Нами обсуждается новый механизм формирования фрактальных структур, суть которого состоит в следующем. При облучении поверхности образца импульсным пучком частиц в образце, на глубине, определяемой кинетической энергией бомбардирующих частиц, в течение короткого промежутка времени происходит заметное выделение энергии. В результате этого при облучении образца электронами происходит плавление поверхностного слоя с последующей кристаллизацией или аморфизацией, а в случае ионного пучка наблюдается ионное перемешивание [11]. При этом в условиях интенсивной диссипации происходят фазовые превращения вещества, характеризуемые образованием пористых фрактальных агрегатов, подобно тому, как это имеет место при лазерном облучении металлов [9,10].

Если такой механизм действительно реализуется, то наш подход имеет ряд преимуществ по сравнению с лазерным облучением:

— максимально используется энергия пучка;
— достигается большая глубина проникновения пучка в образец;
— возможна регулировка энергии, выделяемой в образце.

Анализируемые образцы были получены на установке ЭЛИОНА (ЛСВЭ ОИЯИ), позволяющей формировать электронные и ионные пучки со следующими параметрами [12]:

— кинетическая энергия ионов и электронов	100 + 150 кэВ
— длительность импульса тока пучка	300 нс
— плотность тока пучка электронов	100 + 1000 А/см^2
— плотность тока пучка ионов	5 + 200 А/см^2
— сорт ионов	C^+, Ti^+.

Блок-схема установки показана на рис.1, а на рис.2 приведены вольт-амперные характеристики источника ионов для типичных материалов: Be, C, Cu, Al. Для облучения использовались металлы, металлические пленки на подложках из кремния, а также высокотемпературные сверхпроводники. Микрофотографирование поверхности облученных образцов проводилось на сканирующем электронном микроскопе JSM870.

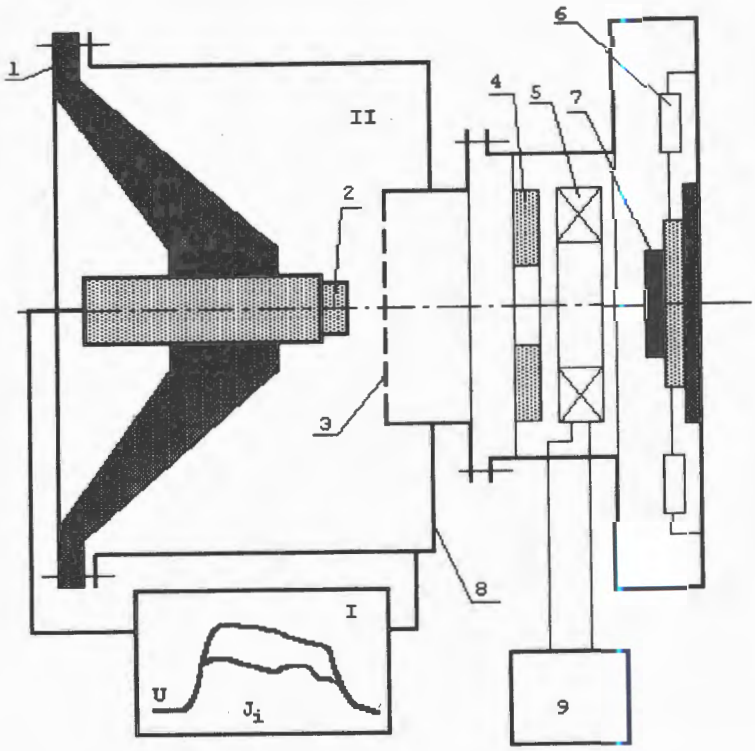

Рис.1. Блок-схема установки. I — генератор импульсного напряжения, II — плазменный эмиттер электронов и ионов, 1 — проходной высоковольтный изолятор, 2 — эмиттер частиц; 3 — вытягивающий электрод, 4 — коллиматор, 5 — трансформатор Роговского, 6 — шунт тока, 7 — образец, 8 — вакуумная камера, 9 — осциллограф

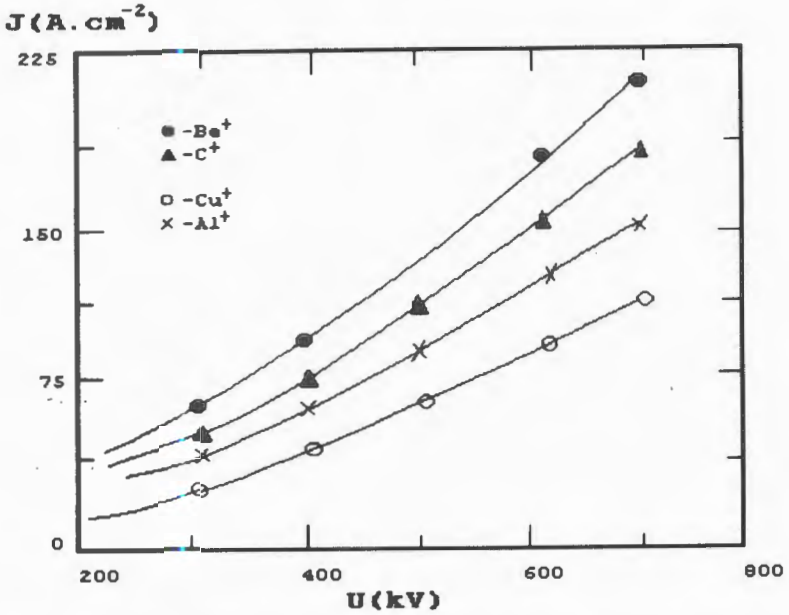

Рис.2. Вольт-амперная характеристика ионного диода установки ЭЛИОНА для типичных материалов Be, C, Cu, Al, снятая при длительности импульса 300 нс. Расстояние между анодом и катодом — 7 мм

2. Определение фрактальной размерности

Для анализа микрофотографий была разработана программа PLATO, использующая box-counting алгоритм, описанный в [13]. Процедура обработки изображений на микрофотографиях состояла в следующем. Все графические файлы (растры), полученные в результате сканирования микрофотографий, приводились к черно-белой шкале: всего 256 градаций от черного (0) до белого (255). Затем растры преобразовывались согласно следующему алгоритму. Выбирался граничный цвет X: $0 < X < 255$. Затем все цвета, начиная с цвета X и выше, заменялись на белый цвет, а остальные — на черный. При этом цвет X выбирался таким образом, чтобы изоцветовая линия имела максимальную длину.

Для проверки работоспособности программы и определения погрешности были проведены измерения размерностей тестовых объектов: прямой линии ($D = 1$), кривой Коха ($D = \ln 4/\ln 3 \approx 1{,}2618...$), кривой Гивена ($D = \ln 6/\ln 3 \approx 1{,}63092...$). Относительная погрешность не превышает 0,04.

Вывод о том, что изображения на микрофотографиях, полученных в процессе экспериментов с электронно-ионным источником, являются фракталами, основан на результатах вычислений длины кривой, «разделяющей» участки разного цвета. Подсчитав количество квадратов $N(\delta)$ со стороной δ, необходимых для покрытия указанной кривой, можно определить длину как $L(\delta) = N(\delta)\delta$.

3. Результаты

Проведен анализ данных экспериментов, выполненных с целью изучения процесса изменения морфологии поверхности и улучшения эксплуатационных свойств облучаемых материалов.

3.1. Электронное облучение

Приведем результаты облучения стали У8 и пленки Nb(3)Ge на подложке из нержавеющей стали.

Рис.3 содержит фотографию поверхности облученной инструментальной стали У8, полученную на сканирующем электронном микроскопе. Облучение проводилось электронным пучком с кинетической энергией 250 кэВ при токе 1000 А и длительности импульса 300 нс.

Фотографии поверхности Nb(3)Ge, взятые из работы [14], приведены на рис.4. На них показана поверхность пленки Nb(3)Ge, полученной на ленте из нержавеющей стали из паровой фазы (рис.4а) и облученной импульсным электронным пучком при

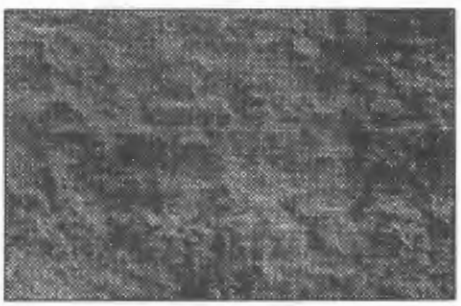

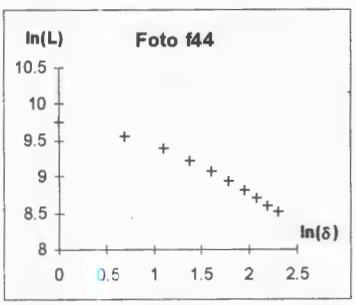

Рис.3. Микрофотография поверхности облученной инструментальной стали У8 и график зависимости длины изоцветовой линии L от размера ячейки покрытия δ (в пикселях). Найденная размерность изолинии $D = 1{,}7$.

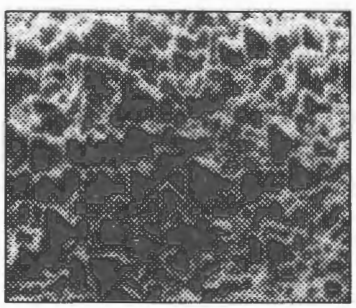

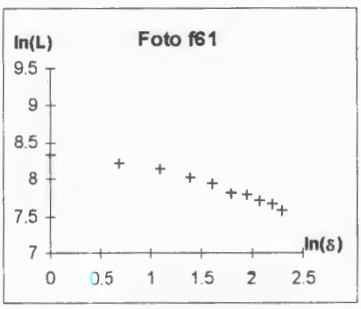

Рис.4а. Микрофотография поверхности пленки Nb(3)Ge, полученной из паровой фазы на подложке из нержавеющей стали и график зависимости длины изоцветовой линии L от размера ячейки покрытия δ (в пикселях). Найденная размерность изолинии $D = 1{,}6$.

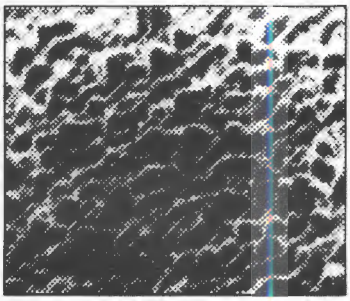

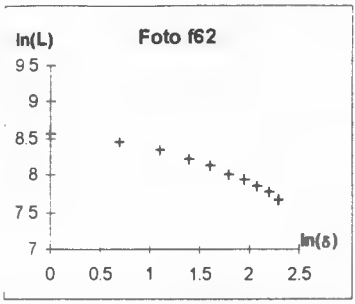

Рис.4б. Микрофотография облученной поверхности Nb(3)Ge I = 300 А/см^2 и график зависимости длины изоцветовой линии L от размера ячейки покрытия δ (в пикселях). Найденная размерность изолинии D = 1,5

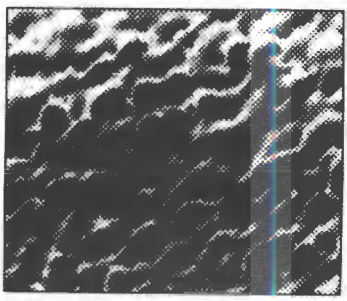

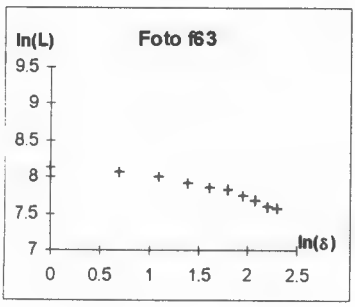

Рис.4в. Микрофотография облученной поверхности Nb(3)Ge I = 700 А/см^2 и график зависимости длины изоцветовой линии L от размера ячейки покрытия δ (в пикселях). Найденная размерность изолинии D = 1,4

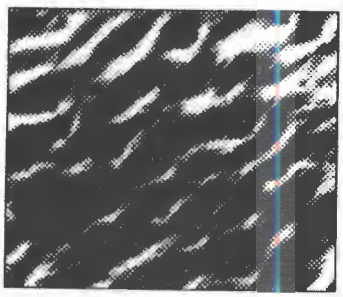

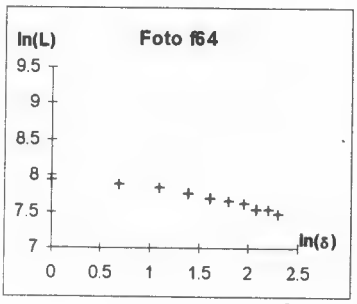

Рис.4г. Микрофотография облученной поверхности Nb(3)Ge I = 1000 А/см^2 и график зависимости длины изоцветовой линии L от размера ячейки покрытия δ (в пикселях). Найденная размерность изолинии D = 1,3

различной плотности электронного тока: 300 А/см^2 — рис.4б, 700 А/см^2 — рис.4в, 1000 А/см^2 — рис.4 — при кинетической энергии электронов 100 кэВ и длительности импульса тока пучка 30 нс. В последнем случае на фотографиях виден поверхностный проплав пленки.

3.2. Ионное облучение

Фотографии поверхности пленки Ti, облученной ионами Ti, представлены на рис.5а и 5б. Режимы облучения отличались кинетической энергией однозарядных ионов титана: рис.5а соответствует энергии ионов титана 250 кэВ, рис.5б — 400 кэВ.

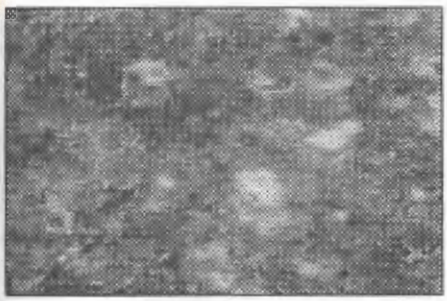

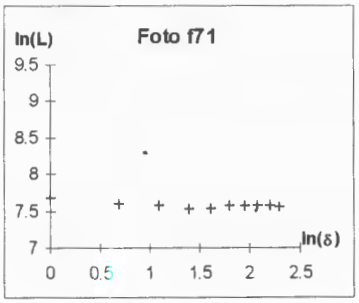

Рис.5а. Микрофотография облученной поверхности пленки Ti U = 250 кэВ и график зависимости длины изоцветовой линии L от размера ячейки покрытия δ (в пикселях). Найденная размерность изолинии D = 1,0

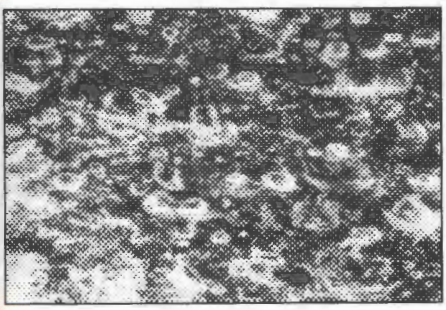

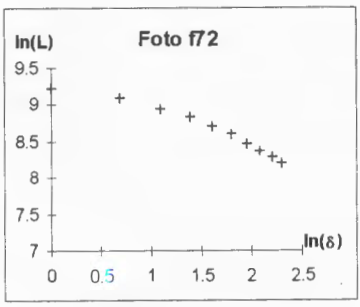

Рис.5б. Микрофотография облученной поверхности пленки Ti U = 400 кэВ и график зависимости длины изоцветовой линии L от размера ячейки покрытия δ (в пикселях). Найденная размерность изолинии D = 1,6

3.3. Фрактальные структуры

Для гладких кривых при $\delta \to 0$ величина $L(\delta)$ стремится к постоянной величине, равной ее длине. Однако для кривых на микрофотографиях этого не происходит. На графиках, приведенных возле каждой микрофотографии, показана зависимость $L(\delta)$ от δ, построенная в логарифмическом масштабе. Из этих графиков следует, что длины

кривых описываются приближенной формулой $L(\delta) \sim \delta^{1-D}$ с показателем степени $D > 1$. Этот факт указывает на то, что структуры, изображенные на фотографиях, имеют фрактальный характер.

Из рассмотрения представленных экспериментальных данных и результатов численного анализа следует, что поверхность облученных образцов имеет фрактальную природу. При этом заметим, что наши результаты носят предварительный характер, и нами не проводится детальный анализ применимости некоторых модельных представлений для описания получаемых экспериментальных результатов.

4. Обсуждение результатов

Формирование фрактальных структур на поверхности раздела (интерфейса) наблюдается экспериментально уже достаточно давно, прежде всего в процессах образования тонких полупроводниковых пленок (см., например, [10]) и кристаллизации. Простейшая модель, описывающая такие процессы, — нелинейное стохастическое дифференциальное уравнение типа Кардара — Паризи — Занга (KPZ) [15], поведение решений которого хотя и объясняется качественно, но в силу математических трудностей, обусловленных значительным вкладом от нелинейного члена $\lambda(\nabla h)^2$, не может быть однозначно связано с управляющими параметрами внешней среды, в которой происходит формирование фрактальных агрегатов.

В случае пучковых технологий процессы происходят за очень короткие времена, квазиадиабатически. Роль нелинейного члена, упомянутого выше, при этом падает и такие параметры структуры, как пористость (а следовательно, фрактальная размерность) и прочность, полностью определяются свойствами материала и свойствами пучка. В простейшей модели типа KPZ, в условиях малости нелинейного члена, анализ подобия дает для размерности напыляемой поверхности $D_F = 2{,}5 + \Delta$. Малая поправка Δ определяется энергетическим разбросом пучка и скоростью поверхностной диффузии. Оба параметра хорошо контролируются: первый — изменением параметров источника частиц, второй — предварительной обработкой поверхности образца [16].

При повышении энергии пучка ($W = IU\tau$, где I — ток пучка, U — кинетическая энергия, τ — длительность импульса), когда доминирующими становятся процессы плавления, кристаллизации и аморфизации, а роль прилипания кластеров уменьшается, основными процессами становятся быстрый разогрев и охлаждение поверхностного слоя, благодаря чему, как показано экспериментально [1], улучшаются прочностные свойства облучаемого материала. Именно это и наблюдалось при исследовании микрофотографий. Так, фрактальная размерность изолиний на фотографиях облученной инструменальной стали (рис.3) падает с увеличением интенсивности пучка с 1,6 до 1,3. В целом же, размерность изолиний попадает в пределы 1,3 + 1,7 (а самих поверхностей, следовательно, около 2,3 + 2,7), что неплохо согласуется с моделями типа KPZ, упомянутыми выше. Динамика этих процессов, безусловно, заслуживает глубокого исследования, хотя, по-видимому, не проявляется непосредственно в наблюдаемых свойствах поверхности.

В настоящей работе исследовалась не фрактальная размерность самой подвергшейся облучению поверхности, а лишь ее изо(цветовые) линии. Для достаточно гладких в трансверсальном направлении фрактальных поверхностей — это, например, имеет место для земного ландшафта — размерность поверхностей ровно на 1 превосходит размерность изолиний [17]; следовательно, можно оценить размерность самой поверхности и сравнить результаты с теоретическими предсказаниями. В случае металлов, подвергшихся поверхностной модификации, такая связь является хотя и весьма вероятной, но не самоочевидной. Здесь, безусловно, важны дальнейшие исследования, требующие прецизионной электронной микроскопии.

Выводы

Экспериментально показано, что в результате облучения твердых материалов импульсными сильноточными электронными и ионными пучками на поверхности образцов образуются фрактальные структуры, имеющие разные фрактальные размерности. Имеются определенные теоретические предпосылки к установлению связи между образуемой на поверхности материалов структурой и происходящими физико-химическими процессами, однако это требует дальнейшего более детального изучения исследуемого явления.

Работа выполнена при поддержке Российского фонда фундаментальных исследований (грант РФФИ-96-02-19508) и поддержке ESPRIT (проект 21042).

Литература

1. Диденко А.Н., Лигачев А.Е., Куракин И.Б. — Взаимодействие заряженных частиц с металлами и сплавами. М.: Энергоатомиздат, 1988.
2. Materials Synthesis and Processing Using Ion Beams. — Materials Research Society Symposium Proceedings, v.316.(Ed. by R.J.Culbertson et al.), Pittsburg, USA, 1994.
3. Смирнов Б.М. — УФН, 1993, т.163, с.51.
4. Фракталы в физике. Труды VI Международного симпозиума по фракталам в физике (под ред. Л.Пьетронеро и Э.Тозатти, пер. с англ. под ред. Я.Г.Синая и И.М.Халатникова). МЦТФ, Триест, Италия, 9—12 июля, 1985.
5. Forrest S.R., Witten T.A. — J. Phys., 1979, v.A12, L.109.
6. Granqvist C.G., Buhrman R.A. — J. Appl. Phys., 1976, v.47, p.2200.
7. Ершов А.П., Луперштох А.Л., Коломийчук В.Р. — Письма в ЖТФ, 1990, т.16. с.43.
8. Hurd A.J., Shaefer D., Martin J.E. — Phys. Rev., 1987, v.A35, p.2361.
9. Лушников А.А., Пахомов Ф.В., Черняев Г.А. — ДАН СССР, 1987, т.292, с.86.
10. Nánai L. et al. — Chaos, Solitons & Fractals, 1995, 5, p.9.
11. Korenev S.A., Perry A.J. — Vacuum, 1996, p.1089.
12. Коренев С.А. — Препринт ОИЯИ Р13-94-192, Дубна, 1994.

13. Oliver D. — Fractal Vision: Put Fractals to Work for You. SAMS Publishing, Carmel, USA, 1992.
14. Вавра И., Коренев С.А. — Препринт ОИЯИ Р13-88-60, Дубна, 1988.
15. Kardar M., Parisi G., Zhang Y. — Phys. Rev. Lett., 1986, v.56, p.889.
16. Шулов В.А. и др. — Поверхность, 1995, 11, с.24.
17. Федер Е. — Фракталы, М.: Мир, 1991.

Рукопись поступила 17 марта 1997 года.

УДК 539.172.17

PRODUCTION OF NUCLEI IN ^{32,34,36}S-INDUCED REACTIONS IN THE ENERGY RANGE 6 ÷ 75 MeV/A

***O.B.Tarasov*[1], *Yu.E.Penionzhkevich*[1], *R.Anne*[2], *D.S.Baiborodin*[1], *D.Guillemaud-Mueller*[3], *A.S.Fomichev*[1], *R.Kalpakchieva*[1], *M.Lewitowicz*[2], *S.M.Lukyanov*[1], *V.Z.Maidikov*[1], *A.C.Mueller*[3], *Yu.Ts.Oganessian*[1], *M.G.Saint-Laurent*[2], *N.K.Skobelev*[1], *O.Sorlin*[3], *V.D.Toneev*[4], *W.Trinder*[2]**

Some regularities in the production of isotopes with $6 \le Z \le 14$ are investigated in reactions induced by ^{32,34,36}S beams at $6 < E < 75$ MeV/A on targets of ^{nat}C, ^{181}Ta and ^{197}Au. The isotope yields and the most probable fragment mass A (for a given Z) are studied as a function of target, projectile mass and energy. A comparison is made of the experimental data at low energies with calculations in the framework of the dynamical model of deep inelastic collisions. The obtained data are considered from the point of view of the feasibility of heavy ion beams for producing nuclei far from the line of stability.

The investigation has been performed at the Flerov Laboratory of Nuclear Reactions, JINR, and at GANIL (France).

Образование ядер в реакциях с ионами ^{32,34,36}S в диапазоне энергий 6 ÷ 75 МэВ/А

О.Б.Тарасов и др.

В настоящей работе исследуются закономерности образования различных изотопов элементов с $6 \le Z \le 14$ в реакциях на пучках ^{32,34,36}S в диапазоне энергий $6 \le E \le 75$ МэВ/А. Получены выходы ядер в зависимости от мишени, от энергии пучка и от нейтронного избытка ядер пучка. На основе экспериментальной информации даны оценки образования различных изотопов для промежуточных энергий на пучках ^{32,34,36}S. Приведены сравнения экспериментальных результатов в области низких энергий с расчетами по динамической модели глубоконеупругих столкновений. Полученные данные обсуждаются с точки зрения возможностей реакций с тяжелыми ионами в широком диапазоне энергий для получения ядер, удаленных от линии стабильности.

Работа выполнена в Лаборатории ядерных реакций им.Г.Н.Флерова ОИЯИ и в ГАНИЛ (Франция).

[1]Flerov Laboratory of Nuclear Reactions, JINR, Dubna.
[2]Grand Accelerateur National d'Ions Lourds, Caen, France.
[3]Institut de Physique Nucleaire, Orsay, France.
[4]Bogoliubov Laboratory of Theoretical Physics, JINR, Dubna.

1. Introduction

Heavy-ion induced reactions are shown to be one of the most efficient tools for producing nuclei far from the stability line. The first experiments carried out in Dubna using ^{22}Ne and ^{40}Ar beams of 7 MeV/A resulted in the observation of about 20 new isotopes lying significantly away from stability [1,2]. In these experiments, a new heavy-ion-reaction mechanism was discovered which later on was called deep inelastic reactions [2]. This process, corresponding to a transitional regime between complete fusion and direct reactions, has been well studied at energies up to 10 MeV/A. It was shown that in deep inelastic processes the production yields of different isotopes could be well described using statistical models [3], and could also be explained by the reaction Q-value taking into account pairing corrections (Q_{gg}-systematics) [2]. However, the advent to the region of nuclear instability by using deep inelastic reactions was limited by the low production cross sections of the sought-after exotic nuclear species. Later, reactions with high-energy heavy ions were used, where as a result of the projectile fragmentation on a thick target many new neutron-rich light-element isotopes were produced with relatively high cross sections [4]. The advent into the region of more neutron-rich isotopes and of heavier elements required beams of heavy projectiles with higher intensities. In the late 1970s, the availability of new heavy ion accelerators of intermediate energies provided further possibilities of using reactions induced by heavy ion beams of $E = 50 + 100$ MeV/A for the production of new exotic nuclei. Very successful was proven to be the use of ^{36}S and ^{48}Ca beams in the fragmentation of which many extremely neutron-rich nuclei were observed. A series of experiments using a ^{48}Ca beam, performed within the GANIL-Dubna collaboration, made possible the observation and investigation of the properties of over 20 new isotopes lying close to the limit of particle stability [5]. There is evidence that, although for a certain domain of nuclei the fragmentation process is dominant already at 27 MeV/A [6], the multinucleon transfer reaction plays still a noticeable role. For example, in ^{58}Ni($Z = 28$)-induced reactions at 55 MeV/A new neutron-deficient Cu isotopes were observed [7]. A similar effect, viz. production of charge pickup products ($Z > 50$), has been observed also in ^{112}Sn-induced reaction at 63 MeV/A [8]. The continuous investigation of the mechamism of nuclear reactions is closely connected with the projects for radioactive nuclear beam facilities, which will open new possibilities for the study of exotic nuclei and where, for the generation of radioactive secondary beams, primary beams of very different energies will be used [9], e.g. 100 MeV/A (GANIL), 20 MeV/A (Dubna) and up to 1 GeA/A (GSI and RIKEN). Questions arise concerning the extent of coexistence of different reaction mechanisms (e.g., multinucleon transfer reactions and fragmentation) at various energies, the dependence of the production rates on the projectile and target isospin, etc.

The present work was undertaken in order to obtain experimental information on the trends in the formation of different isotopes with $6 \leq Z \leq 14$ in reactions induced by ^{32,34,36}S beams in the energy range $6 < E < 75$ MeV/A.

2. Experimental Procedure

The experiments with $^{32,34}S$ beams of energies $6 < E < 20$ MeV/A were carried out at the U400 cyclotron of the Flerov Laboratory of Nuclear Reactions (JINR). The yields of the various isotopes were measured at a laboratory angle $\theta_{lab} = 4°$ using the MSP-144 magnetic spectrometer [10] with a position-sensitive ionization chamber as the focal plane detector [11]. The solid angle was 0.85 msr; and the momentum acceptance, ± 4.1%. In the measurements, targets of ^{nat}C (400 μg/cm^2 thick) and ^{197}Au (200 μg/cm^2 thick) were used. The beam monitoring was performed by means of a Faraday cup. The Z and A identification of the reaction products was done using the measured energy-loss (dE), total energy (E) and position (x) in the focal plane. The relations used are:

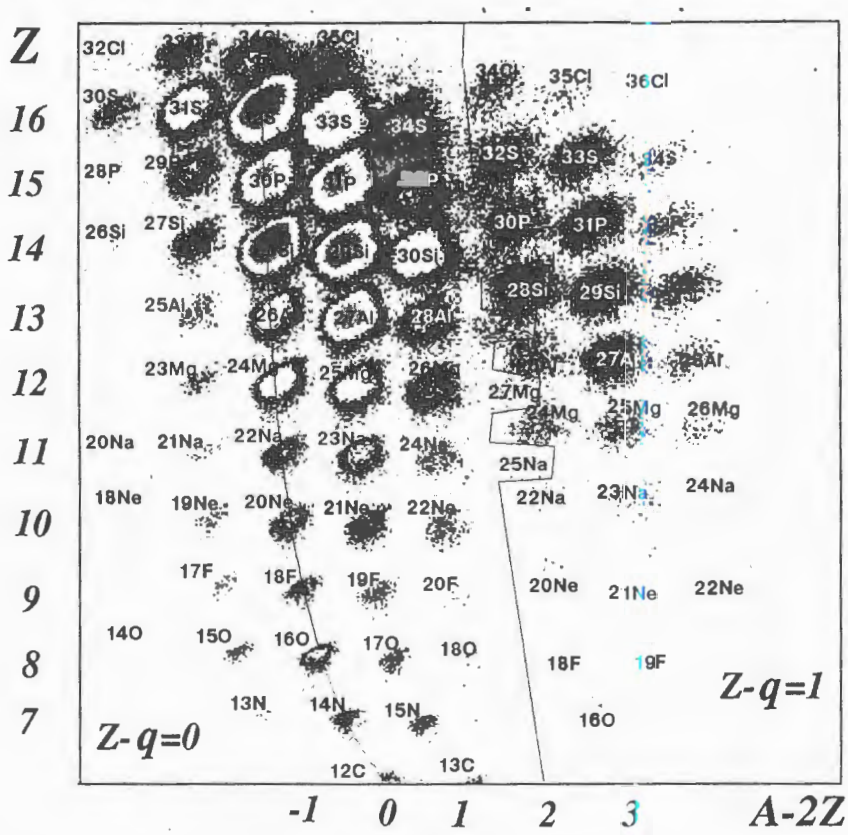

Fig.1. Identification matrix ($A - 2Z$, Z) of the products of the ^{32}S (14.5 MeV/A) + C reaction obtained at a magnetic field $B = 0.7975$ T. The left solid line passes through the completely stripped nuclei with zero isotopic spin. The right curve discriminates between regions of nuclei with charge $q = Z$ and $q = Z - 1$

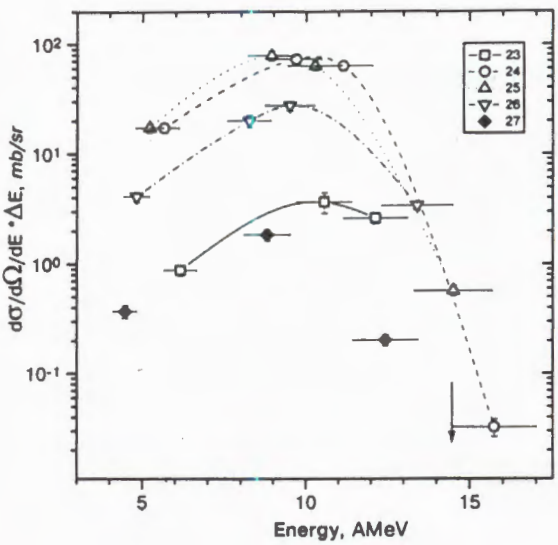

Fig.2. Energy spectra of magnesium isotopes from the reaction ^{32}S (14.5 MeV/A) + C. The horizontal error bars indicate the energy acceptance at the corresponding magnetic rigidity of the spectrometer. The vertical arrow indicates the primary beam energy. The curves are the result of smoothing

$$dE \approx \frac{AZ^2}{E}, \tag{1}$$

$$E = K(Bx)^2 \frac{q^2}{A}, \tag{2}$$

where A, Z and q are the mass, the atomic number and the ionic charge of the nucleus, respectively, B — the magnetic field of the spectrometer and k — a constant. For a better presentation of the identified isotopes a two-dimensional plot of production yields as a function of $A - 2Z$ and Z was used. One example is shown in Fig.1. As can be seen from the figure, in the given experimental set-up, a good separation of the isotopes ranging from C to Cl was achieved, which in turn allowed unambiguous identification of the reaction products.

Several settings of magnetic spectrometer was used in order to obtain the energy spectra of the produced isotopes. Fig.2 represents the energy distributions of Mg isotopes obtained in the reaction ^{32}S (14.5 MeV/A) + C.

The ^{36}S (75 MeV/A)-beam was provided by the accelerator complex GANIL (France) and the isotope yields were measured [12] with the help of the fragment separator LISE [13].

3. Experimental Results and Their Analysis

The results discussed in the present work have been obtained in reactions induced by ^{32,34,36}S ions in a very broad energy range.

The distributions of carbon, oxygen, neon, magnesium and silicon isotopes produced in the ^{36}S (75 MeV/A)-projectile fragmentation on two targets (^{nat}C and ^{181}Ta) are shown in Fig.3. To describe the experimental data on the production cross sections of the isotopes

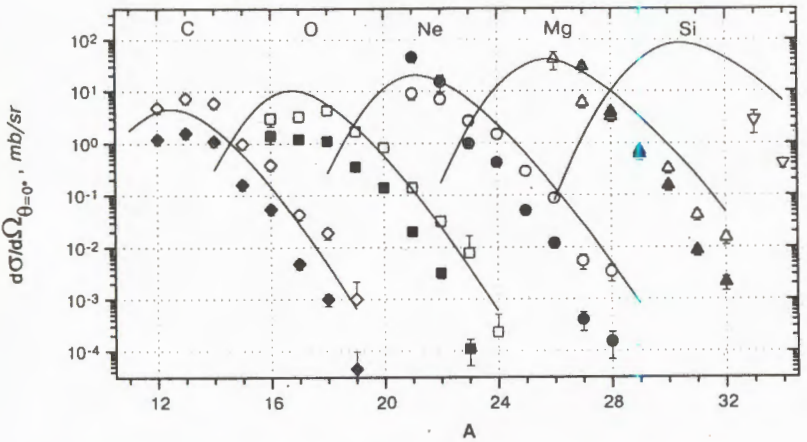

Fig.3. Experimental isotopic distributions of carbon, oxygen, neon, magnesium and silicon nuclei obtained in the fragmentation of a 75 MeV/A ^{36}S beam on two targets — ^{12}C (closed symbols) and ^{181}Ta (open symbols) [12]. The solid line is the result of calculations for the Ta target based on a modification of the empirical parameterization [14]

with atomic nubmers $6 \leq Z \leq 14$ an empirical parametrization similar to the one in [14] was used. The calculations for the Ta-target, denoted by the solid line in Fig.3, show a satisfactory agreement with the experimental data. It can also be seen that at an energy of 75 MeV/A the production cross sections of neutron-rich nuclei are higher for the Ta than for the C-target.

Figures 4a,b show the experimental isotopic distributions from the ^{32}S (9.1 and 16.1 MeV/A) beam for two target (^{nat}C and ^{197}Au), and Fig.4c — the calculations for ^{32}S at 75 MeV/A, obtained as for Fig.3 using the same set of parameters. From the comparison of the experimental data with the calculations it follows that the isotopic distributions can be described by a smooth curve close to a Gaussian distribution. The widths of these distributions at 9.1 and 16.1 MeV/A differ strongly for the two targets (^{nat}C, ^{197}Au), at least for the isotopes of elements far from the projectile (oxygen and neon). At the same time, the yield of the neutron-rich isotopes of these elements in the case of the Au-target is significantly higher than in the case of the C-target.

The comparison (Fig.5) of the differential production cross sections as a function of the atomic number Z of the products for different targets, projectile energies and projectile neutron excess has made it possible to draw the following conclusions about the trends in the formation of various nuclei in *S*-induced reactions.

At energies 7 + 10 MeV/A for the light target, a rather large drop in cross section for smaller Z-values (or greater number of transferred protons) is observed: from 700 mb/sr, in the case of two stripped protons, to 1 mb/sr, for the stripping of 7 protons (see Fig.5a). At higher bombarding energies this difference decreases and at intermediate energies is negligible (Fig.5b). Comparison of reactions induced by projectiles of different mass shows that

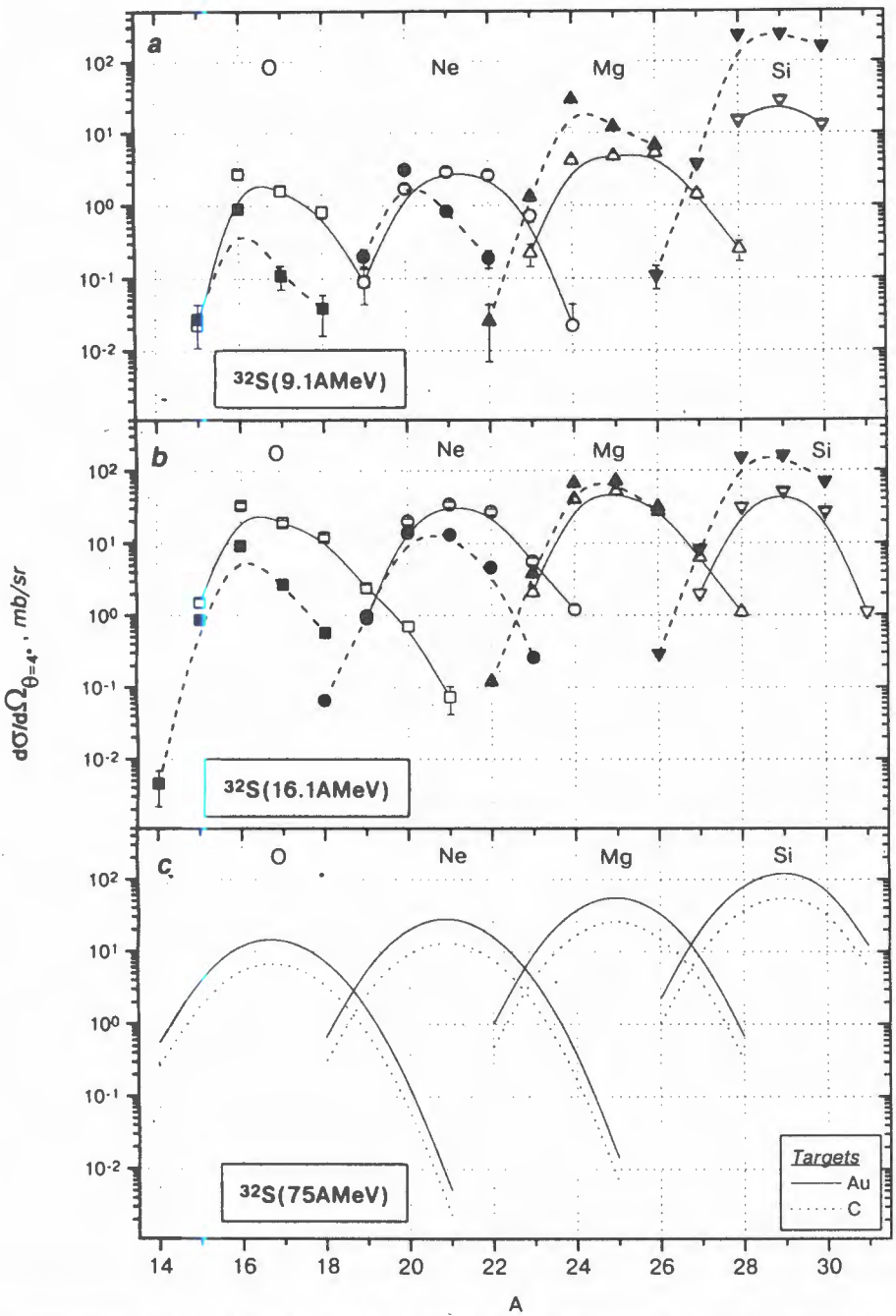

Fig.4. Experimental isotopic distributions of oxygen, neon, magnesium and silicon isotopes obtained for two targets, ^{12}C (closed symbols) and ^{197}Au (open symbols), at a laboratory angle $\theta_{lab} = 4°$ and at two different energies of ^{32}S, 9.1 MeV/A (a), and 16.1 MeV/A (b). Calculated distributions for 75 MeV/A are presented for $\theta_{lab} = 0°$ in (c). The curves on (a) and (b) are the result of smoothing

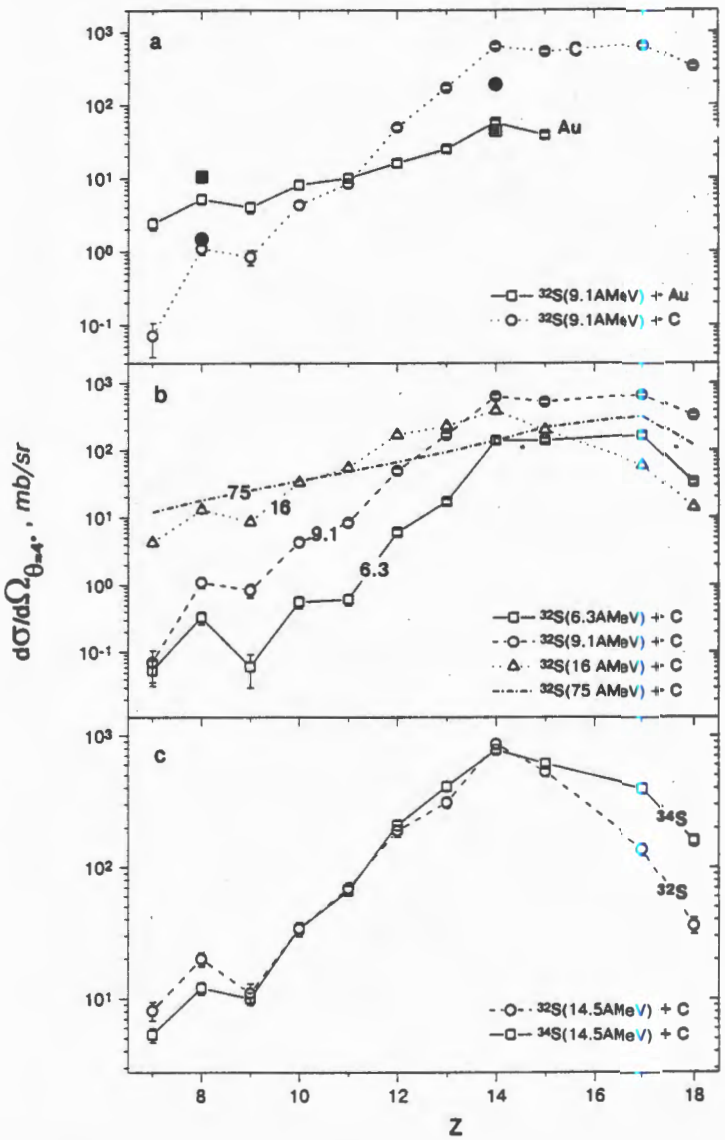

Fig.5. Differential production cross sections of elements vs the atomic number Z. Comparisons are made for: (a) different targets for the ^{32}S beam (9.1 MeV/A), (b) different incident energies of the ^{32}S beam on the C-target, (c) different neutron excesses of the projectile in the case of ^{32}S (14.5 MeV/A) and ^{34}S (14.6 MeV/A) beams. The closed symbols in (a) correspond to theoretical calculations carried out in the framework of the dynamical model of deep inelastic collisions [17]

the cross sections obtained for ^{32}S and ^{34}S beams are very close to each other. Significant difference can be noticed only for products with Z higher than the projectile atomic number, which corresponds to the case of pick-up of protons by the projectile (Fig.5c).

A comparison of the centers of gravity of the isotopic differential-cross-section-distribuions of Fig.4, corresponding to neutron excess values (N–Z), is shown in Fig.6 for the studied reactions as a function of the atomic number Z. In the case of the heavy target, one can observe on the average a shift of the centers of gravity in the direction of the neutron-rich region when decreasing the bombarding energy (Fig.6a). On the contrary, the displacement is towards the proton-rich side for the light target (Fig.6b). The observed trend is in a qualitative agreement with the microscopic theory of multinucleon exchange [15]. The direction of the flow of nucleons in the system is determined by the difference in the corresponding Fermi energies, with the nucleons «flowing» from the nucleus with a higher Fermi energy to the nucleus with the smaller one. The decreased shift in the centers of gravity with increasing the projectile energy in the case of the heavy target can be explained by the high excitation, which can lead to the emission of a larger number of neutrons. Moreover, at small incident energies oscillations are observed in the centers-of-gravity distributions, due to odd-even effects, which are smoothed with increasing the energy. Figures 6c,d show the Z dependence of the most probable neutron excess of the produced isotopes for the two ion beams, ^{32}S and ^{34}S, at an energy of 14.5 MeV/A (experimental data) and at 75 MeV/A (calculated values). From Fig.6c it follows that, from the point of view of the production of neutron-rich isotopes, there is only a small advantage in using a ^{34}S beam compared to a beam of ^{32}S at an energy of 14.5 MeV/A. However, at high energies some advantage can be expected, but only for the production of nuclei close to the projectile with $Z \geq 12$.

As it was mentioned earlier, the yields of isotopes in deep inelastic processes are well described by the reaction energy (Q_{gg}). The cross sections are determined by the relation [2]:

$$\sigma \sim \exp\{[Q_{gg} + \Delta E_c - \delta]/T\}, \tag{3}$$

where Q_{gg} is the energy necessary for the rearrangement of the nuclei in the input channel into the nuclei in the exit channel, ΔE_c — the change in the Coulomb energy of the system due to the redistribution of protons between the nuclei and to the deformation of the system, δ — the nucleon pairing corrections, and T — the temperature of the dinuclear system. Figure 7 presents the experimental differential cross sections for producing oxygen isotopes as a function of Q_{gg} for different target-projectile combinations at various projectile energies. It can be seen that there is an overall good agreement between the experimental points and the expected from relation (3). Making use of the Q_{gg} systematics, it is possible to estimate the yields of nuclei lying far from the stability line.

The obtained experimental results are of great interest from the point of view of the reaction mechanism involved in the formation of nuclei and because they give a possibility of estimating the usefulness of heavy-ion-induced reactions as a way to produce high-intensity beams in radioactive nuclear beam factories. For this purpose it is necessary to

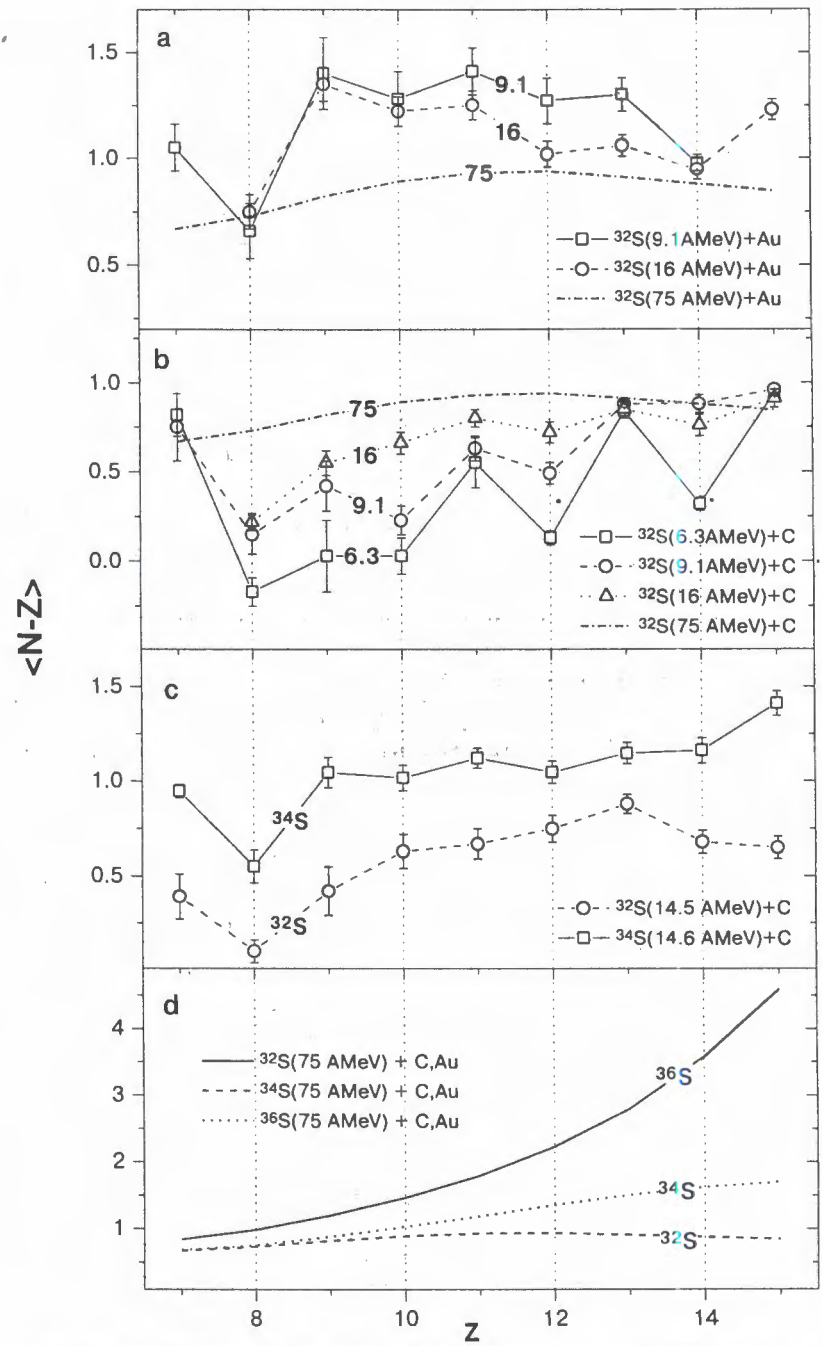

Fig.6. Centers of gravity, expressed as (N–Z), of the differential distributions of Fig.4, as a function of the atomic number Z. Energy dependence for the ^{32}S beam for the gold target (a), the carbon target (b); dependence on the projectile neutron excess at an energy of 14.5 MeV/A for a carbon target (c), and calculations for $^{32,34,36}S$ at 75 MeV/A (d)

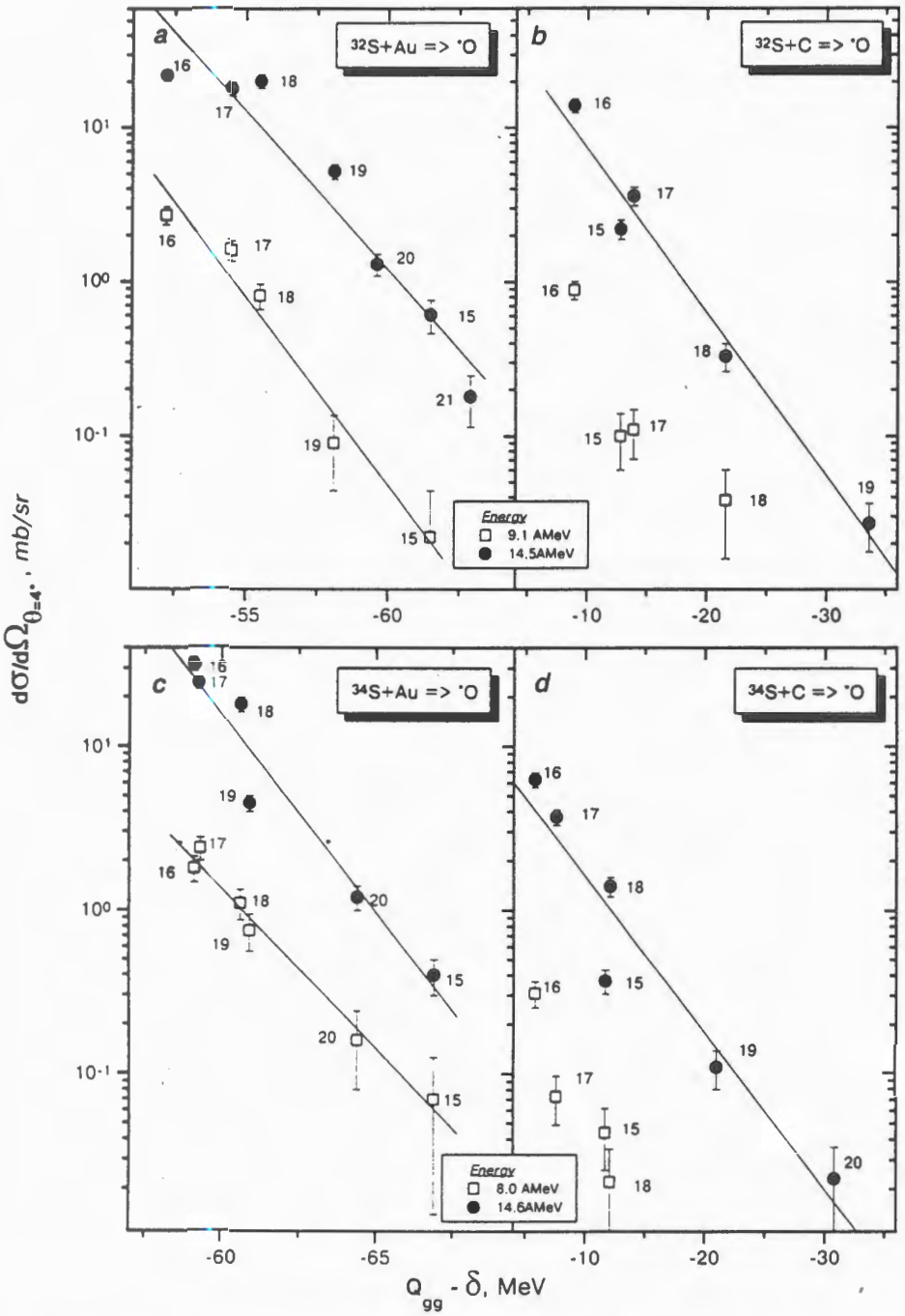

Fig.7. Experimental differential production cross sections for oxygen isotopes as a function of Q_{gg}, in different target-projectile combinations at various energies. The lines are fits with the relation $d\sigma/d\Omega = C_1 \exp[C_2(Q_{gg} - \delta)]$

consider the total reaction cross sections, which means that the angular distributions of the products have to be taken into account.

The angular distributions at low energies $6 < E < 20$ MeV/A were calculated in the framework of the dynamical model of deep inelastic collisions [16,17]. This model takes into account both the dissipation of the kinetic energy of the colliding nuclei and the fluctuations of the motion of the nuclei with respect to the classical trajectories, as well as the effect of deformation of the fragments in the exit channel. The results of the calculations for producing oxygen nuclei in the $^{32}S + ^{197}A$ reaction are presented in Fig.8. The solid and dashed curves correspond to deep inelastic fragments produced at different ion kinetic energy losses ($\Delta E > 50$ MeV and $\Delta E > E - V_C$). In Fig.8, two experimental points from the present experiment are also included. They are in agreement with the calculation corresponding to the small kinetic energy losses. This implies that the differential cross sections can be transformed to total cross sections by integrating over the angular distributions for the small kinetic energy losses.

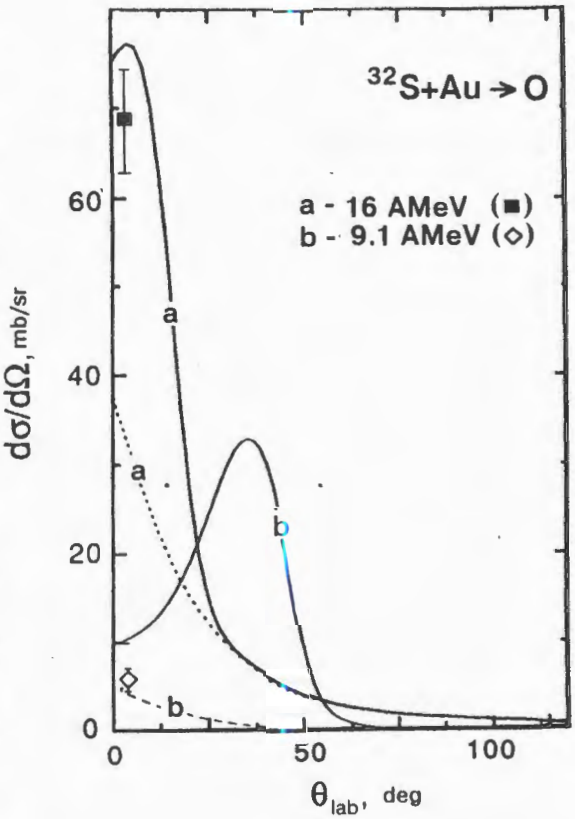

Fig.8. Angular distributions for oxygen isotopes obtained in the reaction $^{32}S + Au$ at 16 MeV/A (a) and 9.1 MeV/A (b), calculated in the framework of the dynamical model of deep irelastic collisons [17]. The solid and dashed curves correspond to deep inelastic fragments produced at projectile kinetic energy losses $\Delta E > 50$ MeV and $\Delta E > E - V_C$. The two points are from the present experiment

In the intermediate energy domain, the maximum of the angular distribution of the reaction products lies at $\theta \cong 0°$. The transformation of the differential into total cross sections was made on the basis of the angular distributions calculated by the method used in Ref.18. In the laboratory coordinate system, the angular distributions of products at intermediate energies can be described according to [18] by the expressions:

$$\frac{d^2\sigma}{d\Omega\, dE_A} \propto \sqrt{2AE_A}\, \exp\left[-\frac{A}{\sigma_P^2}\left(E_A - 2\cos\theta \sqrt{E_A \bar{E}} \right) + \bar{E} \right], \qquad (4)$$

where A and E_A are the mass number and the kinetic energy of the fragment, respectively, $\overline{E}$ is the most probable value of the energy and σ_p is the width of the fragment momentum distribution.

The total production cross sections for some isotopes of oxygen obtained by integrating over the angular distributions are shown in Fig.9 as a function of the energy of the projectiles ^{32,34,36}S. As can be seen from Fig.9a the cross sections rise for incident energies up to 15 ÷ 20 MeV/A. For higher energies it can be speculated that they either go to a plateau (^{15}O) or pass through a maximum, after which they tend to decrease (^{19}O, ^{21}O). The solid curves in the figure are the results of smoothing. The dashed lines present the calculated cross sections of transfer reaction products (normalized to the experimental points) as a function of projectile energy. The calculation of the yields of the primary fragments was carried out using the microscopic transport model assuming a binary character of the reaction [15]. The isotopic distributions of the final (experimentally observed) nuclei were calculated within the framework of the statistical theory of decay of excited primary fragments [19].

The comparison of the experimental data and the calculations shows (see Fig.9a) that the contribution from deep inelastic transfer reactions to the cross section of producing both neutron-rich and neutron-deficient isotopes is dominant at low energies, while at intermediate energies the main contribution comes from fragmentation reactions. Nevertheless, as one can see from the figure, at intermediate energies the contribution of multinucleon transfer reactions is still noticeable.

On the basis of the experimental data shown in Fig.9, the yields of different oxygen isotopes as a function of projectile energy were calculated, assuming total absorption in the target of the beam having an initial energy E_0, using the relation:

$$N(E_0) = \int_{V_C}^{E_0} \frac{\sigma(E) N_{\text{beam}}}{M_{\text{target}}} \left(\frac{dE}{dX} \right)^{-1} dE \quad [\text{sec}^{-1}], \tag{5}$$

where V_C is the Coulomb barrier, $\sigma(E)$ — the cross section in units of [cm^2], N_{beam} — the intensity of the beam [pps], M_{target} — the mass of the target nucleus in [mg] and dE/dX corresponds to the stopping power of the projectiles in the target [MeV/(mg/cm^2)]. The yields of oxygen isotopes, calculated using the expession (S), produced in S-induced reaction on a gold target at a beam intensity of 1 eμA are presented in Fig.10 as a function of the projectile energy. In the upper panel (a) one can see the yields of ^{15}O, ^{19}O, and ^{21}O produced by a ^{32}S beam, while in the lower panel (b), the yields of the isotope ^{21}O produced using beams of ^{32}S, ^{34}S, and ^{36}S. From Fig.10a it follows that an increase in the projectile energy leads to an abrupt rise in the yield of neutron-deficient nuclei (^{15}O), while the increase in the yield of neutron-rich nuclei (^{21}O) is negligible. In Fig.10b, it can be seen that at energies of up to 20 MeV/A the difference between the yields of ^{21}O produced with different beams is small. At 75 MeV/A this difference increases and amounts to an order of magnitude for the ^{32}S and ^{36}S beams.

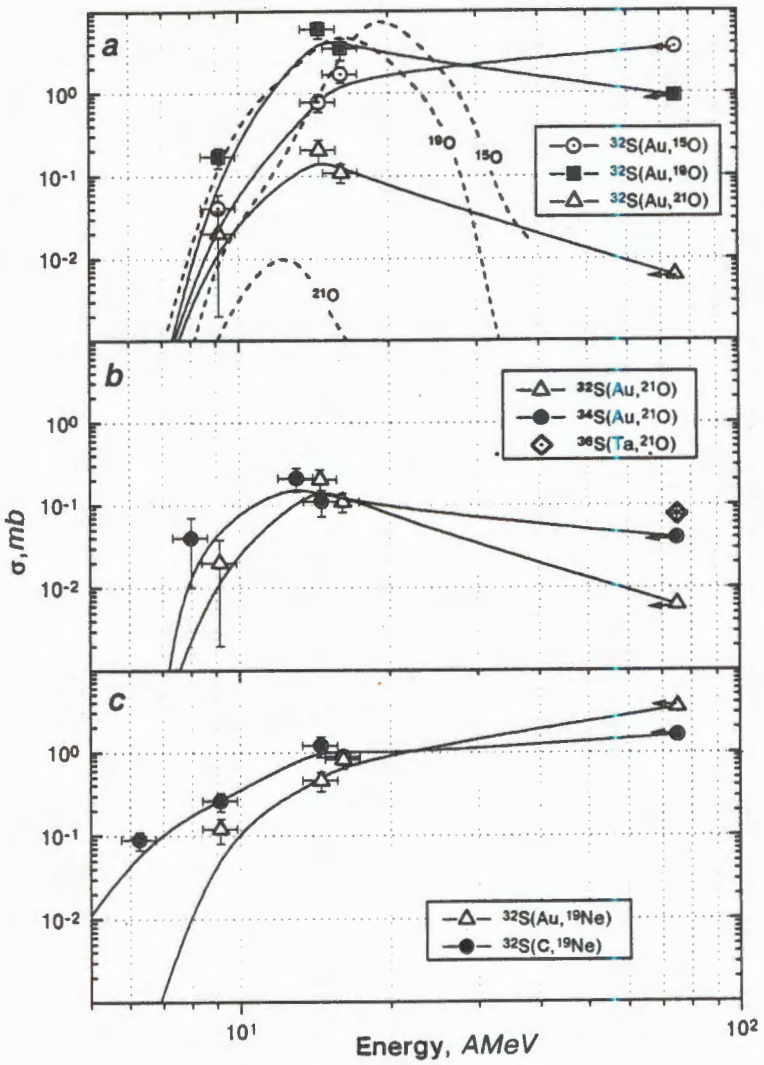

Fig.9. Total production cross sections for different isotopes as a function of energy. Cross sections for producing of: (a) oxygen isotopes in the irradiation of a gold target by the ^{32}S beam; (b) ^{21}O on a gold target by projectiles of different neutron excess, including an experimental point at 75 MeV/A for the ^{36}S-beam; (c) ^{19}Ne on different targets by the ^{32}S-beam. The cross sections for ^{32,34}S (75 MeV/A)-fragmentation were calculated using a modification of the empirical parameterization [14] and are denoted by arrows. The solid curves in the figure are the results of smoothing. The dashed lines present the calculated cross sections of transfer reaction products (normalized to ^{19}O) as a function of the projectile energy

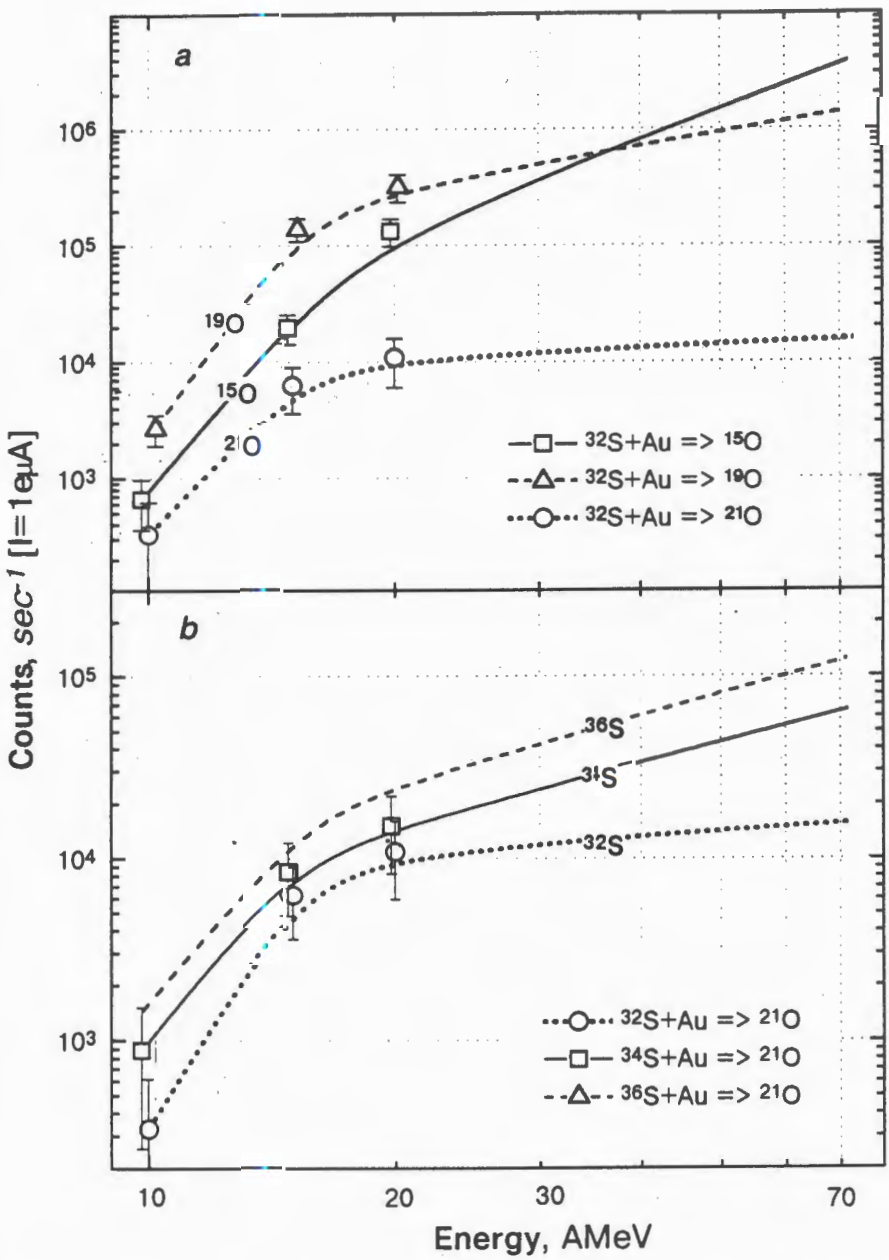

Fig.10. Yields of oxygen isotopes in S-induced reactions on a gold target at a beam current of 1 eμA vs projectile energy. (a) Yields of ^{15}O, ^{19}O, and ^{21}O in the case of a ^{32}S beam. (b) Yields of ^{21}O in the case of ^{32}S, ^{34}S, and ^{36}S beams. Calculations are performed assuming full absorption of the beam in the target

Taking into account that the intensity of the ^{32}S (20 MeV/A) beam in FLNR exceeds by an order of magnitude the intensity of the ^{36}S (75 MeV/A) beam at GANIL, one can expect comparative yields of neutron-rich isotopes within several mass units from the stability line for beams stopped in the target. However, for producing extremely neutron-rich nuclei with $12 \leq Z \leq 15$ the use of a ^{36}S beam is preferable (Fig.6d).

In addition, at it was mentioned earlier, the isotope production cross sections at energies $E < 20$ MeV/A depend on the energy of the reaction (Q_{gg}) and are highest for the smallest absolute values of Q_{gg} (Fig.7). The latter depend on the target-projectile combination and for the case presented in Fig.10 ($^{32}S + Au$) Q_{gg} is not the optimal one ($Q_{gg} < -50$ MeV) for deep inelastic reactions. The target can be chosen so as to have Q_{gg} equal to about -30 MeV (e.g. Nb) and then the expected isotope yields may increase several times.

4. Conclusions

On the basis of the obtained data the following conclusions can be drawn:

- For the energy range 7 + 10 MeV/A a quite abrupt decrease in cross section is observed for the light target when the number of transferred protons is increased. At high energies this difference decreases and at intermediate energies it is negligible.
- As far as the dependence of the isotope yields on the target is concerned, there is evidence that at small projectile energies in the case of the heavy target with a large ratio $N/Z = 1.49$, on the average a shift of the centers of gravity of the differential-cross-section distributions occurs in the direction of the neutron-rich region, and vice versa for the light target ($N/Z = 1$). At intermediate energies this peculiarity of the isotope yields practically vanishes.
- At small incident energies oscillations are observed in the centers-of-gravity distributions. These oscillations are smoothed with increasing the energy.
- At high energies the isotopic content of the projectile plays a dominant role for the production of nuclei close to the projectile ($Z \geq 12$), while at energies $E < 20$ MeV/A the production cross sections for the ^{32}S and ^{34}S beams are comparable. A difference in cross sections is observed only in the region of nuclei heavier than the projectile, where pick-up reactions prevail.
- The isotope production cross sections are seen to rise for energies up to about 15 + 20 MeV/A, after which they either flatten or pass through a maximum and drop for energy regions where fragmentation is expected to prevail.

It is worthwhile noting that for the further investigation of the reaction mechanism it is very important to obtain new information on the yields of reaction products and their angular distributions using ^{32}S and ^{34}S beams in the energy range 30 + 75 MeV/A and a ^{36}S beam at 10 + 50 MeV/A.

Acknowledgements

The authors would like to express their gratitude to A.V.Belozerov for the help in carrying out the experiments, and to A.V.Antonenko and T.N.Shneidman for fruitful discussions.

The present work was carried out with the support of the Russian Foundation for Fundamental Research (RFFI) under grant No.96-02-17381a and of the Bulgarian Foundation for Scientific Research under grant No.F503.

References

1. Artukh A.G. et al. — Nucl. Phys., 1971, v.A176, p.284.
2. Volkov V.V. — Phys. Reports, 1978, v.44, p.93 and references therein; Volkov V.V.— Treatise on Heavy-Ion Science, v.8, p.101 (ed. D.Allan Bromley, Plenum Press, 1989) and references therein.
3. Norenberg W. — Phys. Lett., 1974, v.B52, p.289.
4. Symons T.J.M. et al. — Phys. Rev. Lett., 1979, v.42, p.40; Westfall G.D. et al. — Phys. Rev. Lett., 1979, v.43, p.1595.
5. Guillemaud-Mueller D. et al. — Z. Physik, 1989, v.A332, p.189.
6. Borrel V. et al. — Z. Physik, 1986, v.A324, p.205.
7. Pougheon F. et al. — Z. Physik, 1987, v.A327, p.17.
8. Lewitowicz M. et al. — Phys. Letters, 1994, v.B322, p.20.
9. Penionzhkevich Yu.E. — Phys. Part. Nucl., 1994, v.25, p.394.
10. Maidikov V.Z. et al. — Pribori i Tech. Expt, 1979, v.4, p.68.
11. Belozyorov A.V. et al. — JINR Preprint, P15-89-255, Dubna, 1989.
12. Tarasov O.B. et al. — JINR Rapid Communications, 1996, No.5[79]-96, p.59.
13. Anne R. et al. — NIM, 1987, v.A257, p.215.
14. Sümmerer K. et al. — Phys. Rev., 1990, v.C42, p.2546.
15. Adamian G.G. et al. — Phys. Part. Nucl., 1994, v.25, p.583.
16. Schmidt R., Toneev V., Woloshin G. — Nucl. Phys., 1978, v.A311, p.247.
17. Schmidt R., Toneev V. — Yad. Fizika, 1979, v.30, p.112.
18. Borrel V. et al. — Z. Physik, 1983, v.A314, p.191.
19. Barashenkov V.S., Toneev V.D. — High Energy Interaction of Particles and Nuclei with Atomic Nuclei, Moscow, 1972 (in Russian).

Received on Marth 3, 1997.

УДК 621.039.573

RARE-EARTH ELEMENTS IN SOIL AND PINE NEEDLE FROM NORTHERN TERRESTRIAL ECOSYSTEMS

V.F.Peresedov, S.F.Gundorina, T.M.Ostrovnaya

The experimental data on heavy metal and rare-earth element concentration in the environmental objects (pine needle and soil) caused by the enterprise for the production of mineral phosphoric fertilisers in Apatity (the industrial region in the Murmansk region, Kola Peninsula) have been obtained. The investigation was performed by the neutron activation analysis at the IBR-2 research reactor in the Joint Institute for Nuclear Research. The analysis of nearly 40 element distributions in pine needle and soil from different geographical sites testifies about their contamination by a spectrum of elements, including REEs. Their contamination levels in the soil in the vicinity of the enterprise are significantly high.

The investigation has been performed at the Frank Laboratory of Neutron Physics, JINR.

Редкоземельные элементы в почвах и хвое земных северных экосистем

В.Ф.Переседов, С.Ф.Гундорина, Т.М.Островная

Получены экспериментальные данные по концентрациям тяжелых металлов и редкоземельных элементов (РЗЭ) в объектах окружающей среды (почвах и хвое) в окрестностях комбината для производства минеральных фосфорных удобрений (г.Апатиты Мурманской области). Работа выполнена с использованием нейтронного активационного анализа на реакторе ИБР-2. Анализ поведения концентрацнй ~ 40 элементов в хвое и почвах свидетельствует об их загрязнении рядом элементов и особенно РЗЭ.

Работа выполнена в Лаборатории нейтронной физики им.И.М.Франка ОИЯИ.

Introduction

Monitoring of the environment is actual in connection with significantly increasing technogenic load in many regions of the globe during the past decades. The important objectives of the monitoring are the control and prognosis of the environment state. This requires investigation of interactions between different surroundings as well as the migration processes of contaminating substances. To reliably estimate the quality of the environment systematic studies of different parameters of the environment, including atmospheric air, soil, vegetation, water, etc., need to be carried out. Obtaining of experimental data is an important stage of environmental monitoring.

At present, analysis of the content of different elements and thier combinations is being conducted by different methods. Most suitable are the methods that allow the largest number of elements in biomonitors to be determined reliably. The neutron activation analysis is

an effective method and has been used for monitoring different ecosystems of Russia in the NAA department of FLNP, JINR during the recent years.

As is well known, northern ecosystems are especially sensitive to technogenic load and their recovery is a slow process that takes decades. Therefore, timely monitoring is most important. The objective of the performed investigation was to obtain by NAA the new experimental data on the concentrations of different elements, including REEs in soils and pine needle in the industrial region of the Kola Peninsula (in the vicinity of the plant producing mineral phosphoric fertilisers in the town of Apatity). Till recently, the attention paid to studies of the REEs content in ecosystems, as well as to the REEs accumulation processes by vegetation and to their influence on the vegetable and animal world, was not adequate. This is mainly connected with a low content of REEs in vegetation. Their usual concentrations in clean vegetation are on the low level of $\approx ng/g$ and the ratio of the REE content in plants to that in soils is in the range of $n^*(10^{-5}–10^{-4})$.

Experimental

This is a continuation of our collaboration with Kola Science Centre of the Institute of North Industrial Problems (Apatity, Murmansk region, Russia). In 1995, pine-needle of 1–3 year-age and soil from different genetic horizons were collected in the vicinity of a plant for production of mineral phosphoric fertilisers in Apatity (at 0.5 and 2 km) and in the nearby regions at the distances of 30 and 100 km from the enterprise. The nearby (background) sites were studied for comparison with the data for Apatity. Nearly 40 elements were identified in the samples of soil and pine-needle by the NAA at the IBR-2 high flux research reactor. The procedures of irradiation and elemental analysis by the gamma-spectrometry of short-, middle-, and long-life nuclides were applied. The neutron energy spectra in the irradiation channels of the IBR-2 reactor are characterised by the presence of thermal, epithermal, and fast neutrons with high flux densities [1] and allow one to realize two regimes of sample irradiation, including by thermal, epithermal, fast neutrons and epithermal and fast neutrons. In the first regime, the analysis sensitivity may be higher for Na, Al, Si, S, Cl, K, Sc, Ca, Cr, Ti, V, Mn, Co, Fe, Cu, Zn, La, Ce, Pr, Nd, Eu, Gd, Dy, Lu, Os, Pt; in the second regime — for F, Mg, Ga, Ge, Se, As, Br, Sr, Rb, Y, Zr, Nb, Ru, Mo, Tc, Ph, Cd, Pd, Ag, In, Sn, Te, Sb, I, Ba, Cs, Pr, Sm, Tb, Ho, Tm, Er, Hf, Yb, W, Ta, Re, Ir, Hg, Au, Th, U. This is connected with the difference in the cross-section values for different nuclides in thermal and epithermal neutron energy regions. Thus, the specific character of the neutron energy spectrum and the possibility of sample irradiation in two different regimes (with and without Cadmium) allow us to provide selectivity of the analysis for interesting trace-elements.

Processing of the NAA data was performed by the computer programs and a well-tested bank of nuclear data. Most nuclides were identified by several gamma-lines. The elemental concentrations were calculated by absolute and reference methods (with Standard Reference Materials from MAGATE and the National Institute of Standards (US)). In the gamma-spectrometry, interference during processing was partially avoided by the choice of interference-free photo-peaks. When necessary, contributions from the interfering reactions and the reactions caused by the fast neutrons were accounted for.

Results and Discussion

On the basis of the obtained elemental concentrations in the samples of soil and pine needle (36 and 32, respectively) average concentrations of elements and their confidence intervals were calculated for each geographical point (0.5, 2, 30, and 100 km). The distributions of all determined elements were analysed versus the distance from the enterprise and, for some of them, are presented in Figs.1–3. These distributions testify the conta-

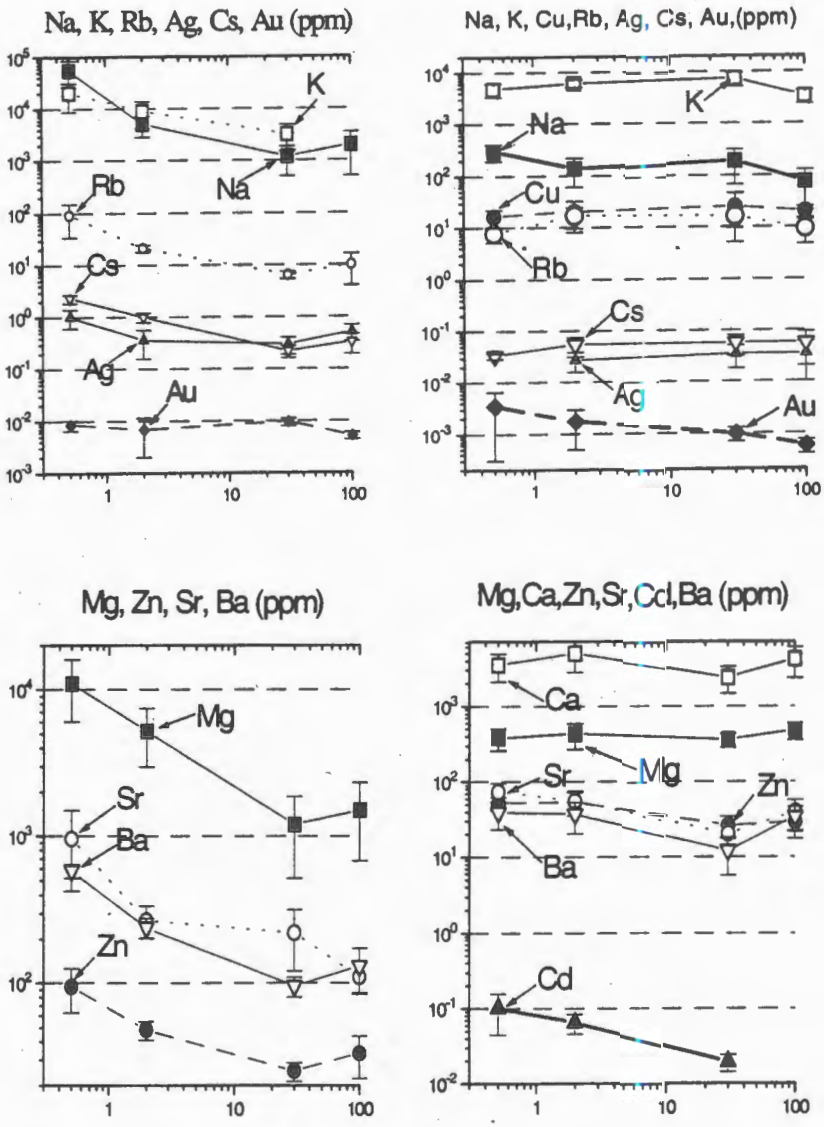

Fig.1. Distributions of elemental concentration for Kola soil and pine needle (left and right, respectively) versus the distance from the enterprise

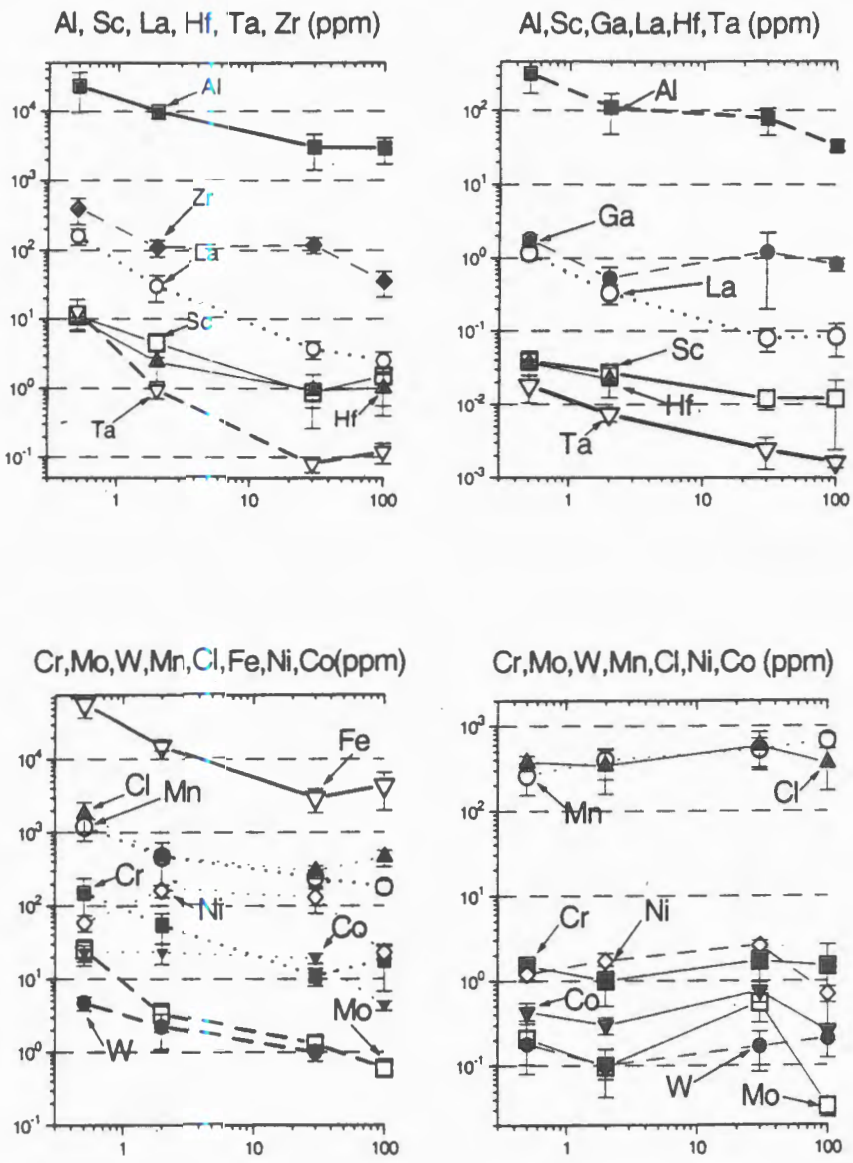

Fig.2. Distributions of elemental concentration for Kola soil and pine needle (left and right, respectively) versus the distance from the enterprise

mination of the biomonitors by the row of elements released in atmosphere by the enterprise in Apatity. Particularly, the increased concentration of Na, K, Rb, Cs, Mg, Sr, Zn, Ba, Al, Zr, Sc, La, Hf, Ta, Fe, Cl, Mn, Cr, Mo, W, Ce, Nd, Sm, Eu, Tb, Yb, Th, and U were observed in superficial soil at distances of 0.5 and 2 km compared to the nearby regions

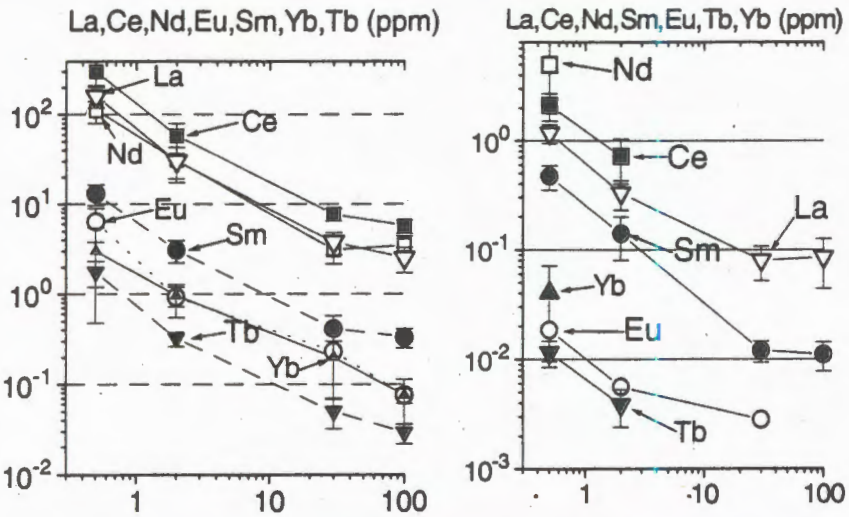

Fig.3. Distributions of elemental concentration for Kola soil and pine needle (left and right, respectively) versus the distance from the enterprise

(30 and 100 km). The concentration of the elements in soil and pine needle with their confidence intervals (in per cent) for Apatity and nearby regions are presented in columns 2–3 of Tables 1–2. The ratios of the maximal REEs concentration in soil (point 0.5 km) to the minimal one (30, 100 km) are high and lay in the range of values from 27 up to 85 (Tab.1, col.4). So, for this specific source of atmospheric pollutions an increased emission of REE is characteristic, what is understandable because the apatit concentrate used as a raw material for the production of mineral phosphoric fertilisers is an intense source of REEs.

In the pine-needle, the increased content of a smaller number of elements, namely — Al, Cd, La, Sc, Ta, Ce, Sm, Eu, Th, and U, is observed. For the content of K, Na, Cu, Rb, Cs, Ag, Ca, Mg, Sr, Zn, Ba, Ga, Hf, Mn, Cl, Cr, Ni, Co, Mo, and W no significant distance-dependence is measured. The concentration of these elements in pine-needle at points 0.5 and 2 km are close to nearby one at points 30 and 100 km. The observed difference in the distributions of concentration of the same elements in soil and pine needle versus the distance from Apatity is, apparently, connected with that in soil, we deal with long-time accumulated amounts of contaminating elements. In pine needle, the contaminating elements were accumulated during a relatively short time and therefore, not exceed significantly their natural concentrations.

Content of REEs in pine-needle in Apatity is higher (1.5–10 times) than in Monchegorsk [7] and significantly higher (10–500 times) than their concentration or upper detection limit in the Tver region (near Moscow). In accordance with Fig.3 we cannot clarify the background content for all REEs in pine-needle. For soil samples we see the complete distance dependence including the suburban points for Sc, La, Ce, Nd, Sm, Eu, Tb, and Yb. As is mentioned above, the natural abundance of REEs in clean vegetation is close to values of the order of *ng / g* [8]. Therefore, the problem of determination of their suburban content in vegetation is not a very simple one. At the same time, this problem is copmlicated by

Table 1. Concentrations of elements (ppm) in soils of the Kola Peninsula (Apatity)

	Literary data	Apatity Maximal	Apatity Minimal	Ratio 2/3	Toxic in Plants
Na	17700 [6]	55000 (50)	1200 (58)	**46.0**	
Mg	17200 [4]	11000 (45)	1200 (57)	**9.2**	
Al	71100 [2]	23000 (58)	2900 (40)	**7.9**	
Cl	1000 [4]	1800 (43)	290 (20)	**6.2**	
K	10500 [4]	20000 (56)	3200 (53)	**6.2**	
Sc	2.5 [4]	11 (40)	0.86 (40)	**12.8**	
V	90 [2]	120 (55)	14 (35)	8.6	50–100
Cr	70 [2]	150 (58)	11 (27)	13.6	60–600
Mn	- 300 [4]	1200 (36)	180 (20)	**6.7**	> 2200
Fe	13100 [4]	57000 (35)	2900 (36)	**19.7**	
Co	8 [2]	23 (25)	4.3 (15)	5.3	
Ni	50 [2]	160 (25)	58 (25)	2.8	
Zn	50 [4]	94 (32)	25 (15)	3.8	
Se	0.37 [3]	1.7 (25)	1.4 (25)	1.2	
As	1 [4]	18 (30)	6.1 (24)	3.0	$15–10^3$
Rb	20 [4]	91 (60)	6.3 (25)	**14.4**	
Sr	70 [4]	960 (55)	110 (25)	**8.7**	
Zr	50 [4]	390 (40)	35 (40)	**11.1**	
Mo	1.0 [2]	25 (40)	0.6 (21)	**41.7**	
Ag	0.015 [4]	1.0 (39)	0.3 (33)	3.3	
Cd	0.8 [4]	0.67 (20)			
Sb	0.07 [4]	1.0 (30)	0.5 (20)	2.0	
Ba	60 [4]	580 (11)	95 (16)	**6.1**	
Cs	1.5 [4]	2.3 (18)	0.22 (25)	**10.5**	
La	0.8 [4]	160 (25)	2.5 (32)	**64.0**	
Ce	5.5 [5]	300 (30)	5.7 (20)	**52.0**	
Nd	2.4 [5]	110 (25)	3.1 (27)	**35.5**	
Sm	0.43 [5]	13.0 (26)	0.33 (23)	**39.0**	
Eu	0.083 [5]	6.4 (40)	0.075 (18)	85.3	
Tb	0.08 [5]	2.5 (25)	0.05 (36)	**50.0**	
Yb	0.8 [4]	2.0 (50)	0.075 (52)	**26.7**	
Hf	0.4 [4]	10 (30)	0.93 (67)	**10.8**	
Ta	0.023 [4]	13 (46)	0.08 (25)	**162.0**	
W	0.7–3 [3]	4.7 (21)	1.0 (25)	**4.7**	
Au	0.007 [4]	0.0095 (18)	0.005 (16)	1.8	
Th	1 [4]	13 (26)	0.33 (37)	**39.4**	
U	0.4 [4]	6.4 (40)	0.075 (19)	**85.3**	

Table 2. Concentration of elements in pine-needle (ppm) of the Kola Peninsula (Apatity)

	Tver Average	Apatity Maximal	Apatity Minimal	Ratio 2/3	Toxic in Plants	Cereal Grains
Na	14 (64)	300 (35)	**74 (71)**	4.1		
Mg	785 (19)	430 (38)	360 (22)	1.2		
Al	148 (46)	300 (45)	33 (15)	**9.1**		
Cl	177 (28)	580 (48)	340 (53)	1.7		
K	2830 (33)	7400 (30)	3300 (30)	2.2		
Sc	0.013 (30)	0.04 (36)	0.012 (30)	3.3		
Cr	< 0.1	1.7 (41)	**1.0 (50)**	1.7	4–30	
V	< 1	2.0 (25)	0.3 (58)	**6.7**		
Mn	234 (51)	670 (20)	260 (40)	2.5		
Fe	55 (43)	412 (29)	67 (44)	**6.2**		25–80
Co	0.039 (89)	0.75 (26)	**0.25 (21)**	3.0	20–50	4–20
Cu		25 (80)	16 (36)	1.6		
Ni	2.4 (70)	2.6 (25)	0.7 (20)	3.7	10–100	0.2–0.6
Zn	33 (36)	52 (21)	26 (33)	2.0	70–400	22–33
Se	< 0.02	0.24 (20)	0.067 (22)	3.6	0.8–22	0.02–0.5
As	< 0.01	0.57 (32)	**0.063 (31)**	**9.1**	2–20	0.05
Rb	21 (76)	17 (44)	7.5 (30)	2.3		4
Sr	3.4 (12)	73 (27)	**20 (28)**	**3.6**	> 600	0.5–2
Mo	< 0.4	0.21 (66)	0.033 (25)	**6.4**	2–10	0.2–0.6
Ag	0.031 (23)	0.05 (30)	0.026 (40)	1.8	5–10	
Cd	< 0.03	0.10 (55)	0.019 (26)	**5.3**	5–30	0.01–0.2
Sb	0.033 (42)	0.028 (45)	0.009 (25)	3.1	> 0.15	0.002
Ba	1.2 (58)	39 (40)	**12 (50)**	3.3	> 500	4–6
Cs	0.081 (91)	0.056 (42)	0.033 (40)	1.7		
La	< 0.01	1.2 (20)	**0.08 (35)**	**15.0**		
Ce	< 0.09	2.1 (28)	< 0.5	**> 40**		
Nd	< 0.2	5.0 (60)	< 0.84	**> 6**		
Sm	< 0.001	0.47 (26)	0.011 (30)	**42.7**		
Eu	0.024 (66)	0.019 (48)	< 0.0028	**> 6.8**		
Tb	< 0.003	0.011 (24)	< 0.00034	**> 32**		
Yb	0.03 (60)	0.04 (50)	< 0.0022	**> 18**		
Hf	0.34 (67)	0.036 (25)	0.022 (43)	1.6		
Ta	0.0015 (40)	0.018 (82)	0.0016 (25)	**11.3**		
W	< 0.02	0.18 (42)	**0.10 (57)**	1.8	> 3	
Au		0.0034 (90)	0.0006 (30)	5.7		
Th	0.07 (12)	0.069 (23)	0.026 (27)	**2.7**		
U	< 0.004	0.022 (30)	0.0073 (25)	**3.0**		

the presence of other contaminating and interfering elements in pine-needle besides REEs. This leads to a decrease in the sensitivity of REEs determination. It can be also noted that in fact, we do not know a priory to what extent the background (suburban) regions are clean. Elucidation of this circumstance was also one of the objectives of this investigation. But we see that pine-needle from the suburban sites is characterised by a sufficiently high content of some other elements, such as Na, Cr, Co, As, Sr, Ba, and W, whose concentration is 5–10 times higher than, for example, in the pine needle from Tver region (Table 2, cols.3,1, respectively). The obtained concentrations and upper detection limits for REEs in the pine needle and soils from suburban sites are in reasonable agreement with analogous ones in [5,8]. Thus we can conclude that for the reliable determination of the majority of REEs in the pine-needle from suburban regions, the maximum sensitivity of analysis must be achieved, possibly, by individual and more suitable regimes of irradiation for some REEs.

Conclusions

As a result, of this work the new experimental data on the concentration of nearly 40 elements in environmental biomonitors, such as soil and pine needle, were obtained. It was elucidated that the investigated enterprise for production of mineral phosphoric fertilisers is a specific source of atmospheric pollution and releases into the environment a wide spectrum of different elements, including REEs. On the basis of the obtained data the emission power of this industrial source of atmospheric pollution can be estimated and used for prognosis of the future state of the environment in this region.

The authors are grateful to their collaborators from the Kola Science Centre of the Institute of North Ecology Problems, to Prof. V.V.Nikonov for providing the samples, the collaborators from FLNP, V.P.Chinaeva, S.S.Pavlov, and V.N.Klochkov, for their assistance in carrying out the project and T.F.Drozdova for the assistance in preparation of this manuscript.

References

1. Peresedov V.F., Rogov A.D. — Journal of Radioanalytical and Nuclear Chemistry, 1996, v.214(4), p.277.
2. Sigel A., Sigel H. — «Metal Ions in Biological Systems», v.20, «Concept on Metal on Toxicity», University of Basel, Switzerland, Marcel Dekker Inc., New York and Basel, 1986.
3. Kabata-Pendias A., Pendias A. — «Trace Elements in Solids and Plants», CRC Press, Boca Raton, Florida, 1984.
4. Fersman A.E. Selected Works, SU Academy of Sciences, Moscow, 1959.
5. Bernd M., Zhang D.L. — The Scien. of the Tot. Environ., 1991, v.103, p.27.
6. Puling L., Jervis R.E. — Journ. of Radioanal. Chem., 1992, v.161, No.1, p.215.
7. Peresedov V.F. et al. — Journal of Radioanalytical and Nuclear Chemistry, 1996, v.207, No.2, p.295.
8. Wyttenbach A. et al. — Biological Trace Elements Research, 1994, v.41, p.13.

Received on January 24, 1997.

УДК 539.172.12

«THERMAL» MULTIFRAGMENTATION IN p + Au COLLISIONS AT RELATIVISTIC ENERGIES

S.P.Avdeyev, V.A.Karnaukhov, W.D.Kuznetsov, L.A.Petrov, V.K.Rodionov, A.S.Zubkevich, H.Oeschler[1], O.V.Bochkarev[2], L.V.Chulkov[2], E.A.Kuzmin[2], A.Budzanovski[3], W.Karcz[3], M.Janicki[3], E.Norbeck[4], A.S.Botvina[5]

Multiple emission of intermediate-mass fragments has been studied for the collisions p + Au at 2.16, 3.6, and 8.1 GeV with the FASA set-up. The mean IMF multiplicities are equal to 1.7, 1.9, and 2.1 (± 0.2) respectively. The multiplicity, charge distributions and kinetic energy spectra of IMF are described in the framework of the empirically modified intranuclear cascade model followed by the statistical multifragmentation model. The results support a scenario of true thermal multifragmentation of a hot and expanded target spectator.

The investigation has been performed at the Laboratory of Nuclear Problems, JINR.

«Тепловая» мультифрагментация в соударениях p + Au при релятивистских энергиях

С.П.Авдеев и др.

Множественная эмиссия фрагментов промежуточной массы была исследована с помощью установки ФАЗА для соударений p + Au при 2,16; 3,6 и 8,1 ГэВ. Найдено, что средние множественности ФПМ соответственно равны 1,7; 1,9 и 2,1 (± 0.2). Распределения по множественности и заряду, а также спектры кинетических энергий ФПМ описываются в рамках эмпирически модифицированной модели внутриядерного каскада, сопровождаемой статистической моделью мультифрагментации. Результаты согласуются со сценарием тепловой мультифрагментации горячего спектатора мишени с пониженной плотностью.

Работа выполнена в Лаборатории ядерных проблем ОИЯИ.

Introduction

The investigation of the decay of very hot nuclei has become a topic of great interest. It is largely concentrated on the process of multiple emission of intermediate mass fragments (IMF, $3 \le Z \le 20$) [1–3]. Now it is established as the main decay mode of highly

[1]Institut für Kernphysik, TH Darmstadt, 64289, Germany.
[2]Kurchatov Institute, 123182 Moscow, Russia.
[3]H.Neiwodniczanski Inst. of Nuclear Physics, 31-342, Cracow, Poland.
[4]University of Iowa, Iowa City, IA 52242, USA.
[5]Institute for Nuclear Research, 117312, Moscow, Russia.

excited nuclei, and this process is likely to occur when a nucleus has expanded and lower density is reached. It is under debate whether this process is related to a liquid-gas phase transition in nuclear matter. The common way to produce very hot nuclei is to use reactions induced by heavy ions at energies 30–100 MeV/nucleon. But in this case heating is accompanied by compression, strong rotation and shape distortion, which cause the so-called dynamic effects in the nuclear decay. It seems difficult to disentangle all these effects to get information on the thermodynamic properties of a hot nuclear system. The picture becomes clearer when light relativistic projectiles are used [4–10]. One should expect that dynamic effects are negligible in that case. A further advantage is that all the IMF's are emitted by the only source — the target spectator, and decay of this hot nucleus proceeds in an apparently statistical manner («thermal multifragmentation»).

The time scale of the IMF emission is a key characteristic for understanding the multifragmentation phenomenon: is it a «slow» sequential process of independent emission of IMF's or is it a new decay mode with «simultaneous» ejection of the fragments governed by the total accessible phase-space? «Simultaneous» means that all fragments are liberated at freeze-out during a time, which is smaller than a characteristic Coulomb time τ_c. For that case emission of IMF's is not independent, they interact via long-range Coulomb forces during acceleration in the electrical field after freeze-out. According to [11], $\tau_c \approx 10^{-21}$ s. Measurement of the emission time for IMF's (τ_{em} is a mean time delay between two consecutive fragment emissions) is a direct way to answer the question as to the nature of the multifragmentation phenomenon. In our papers [12,13] it was found by measuring the relative angle IMF-IMF correlations that for ^{4}He + Au collisions at 14.6 GeV the emission time is less than $3 \cdot 10^{-22}$ s. The trivial mechanism of multiple IMF emission (sequential and independent evaporation) should be definitely excluded. So, the thermal multifragmentation is a new (multibody) decay mode of excited nuclei.

In this paper we present the experimental study of the multifragment emission induced by relativistic protons (up to 8.1 GeV) in gold. The preliminary data were presented in [14].

Experimental Set-Up

The experiments were performed with a proton beam of the JINR synchrophasotron in Dubna at energies of 2.16, 3.6, and 8.1 GeV using the modified 4π-set-up FASA [15]. The main parts of the device are: (i) five ΔE (ion.ch.)$\times$ E(Si)-telescopes, which serve as a trigger for the readout of the system allowing measurement of the charge and energy distributions of IMF's at different angles. They are located at $\theta = 24°$, 68°, 87°, 112°, and 156° to the beam direction and together cover the solid angle 0.03 sr; (ii) a fragment multiplicity detector (FMD) consisting of 64 CsI (Tl) counters (with thickness ranging from 20 to 27 mg·cm^{-2}), which cover 89% of 4π. The FMD gives the number of IMF's in the event and their space distribution. The plexiglass light guides [16] were replaced by hollow metal tubes with a diffuse reflector. This results in reducing the background in FMD (down to less than 2%) caused by the beam halo. It was continuously controlled by means of a

double-gate mode in PM-pulses processing [16]. The scintillator faces were covered by aluminized mylar (0.2 mg·cm^{-2}) to exclude completely the light cross-talk.

A self-supporting Au target 1.5 mg/cm^2 thick was located in the centre of the FASA vacuum chamber. The average beam intensity was $7 \cdot 10^8$ p/spill (spill length 300 ms, spill period 10 s). The blank-target background for telescopes in the angular range 65°–115° is around 5% for $Z_f = 2$ decreasing with Z_f to ≤ 1% for $Z_f \geq 6$.

In this work we revised the calculations of the efficiency of IMF registration by the scintillator counters. The modern data on the response function of CsI(Tl) to heavy ions [17] were used and self-absorption of light in polycrystalline CsI(Tl) [16] was taken into account. The pulse-height thresholds were set (actually off-line) in each counter individually depending on the scintillator thickness to get good separation of IMF from lighter fragments ($Z = 1,2$). The calculated efficiency of FMD for IMF detection is $\varepsilon = 59\%$ (instead of 46% used before), while the admixture of lighter particles to the counting rate is less than 5% with respect ot IMF's.

Fragment Multiplicity

The measured IMF-multiplicity distributions associated with a trigger fragment of charge $6 \leq Z \leq 20$ are shown in Fig.1a. The data were corrected for the admixture of lighter fragments and background in FMD. It was done using the random generator procedure. The mean associated multiplicities $\langle M_A \rangle$ for the beam energies 2.16, 3.6, and 8.1 GeV are equal to 0.73, 0.96, and 1.11 respectively. Note that the number of IMF detected is $1 + M_A$ (triggering fragment is added).

The measured distribution for the associated multiplicity $W(M_A)$ differs from the true (or primary) multiplicity distribution $W(M)$ because of distortion by triggering and because the FMD efficiency is less than 100%. These distributions are related via the response matrix of the FASA set-up $Q(M_A, M)$:

$$W(M_A) = \sum_{M = M_A + 1} Q(M_A, M)\, W(M). \tag{1}$$

The response matrix includes the triggering probability, which is proportional to M, and the probability of detecting (in FMD) M_A fragments from remaining $M - 1$. The latter probability is described by the binomial distribution. So, we have:

$$Q(M_A, M) = \frac{M!}{M_A!(M - 1 - M_A)!}\, \varepsilon^{M_A} (1 - \varepsilon)^{M - 1 - M_A}. \tag{2}$$

Using (1) and (2) one can find the following relation between $\langle M_A \rangle$ and the moments of the primary multiplicity distribution:

$$\frac{\langle M_A \rangle}{\varepsilon} = \frac{\langle M^2 \rangle}{\langle M \rangle} - 1. \tag{3}$$

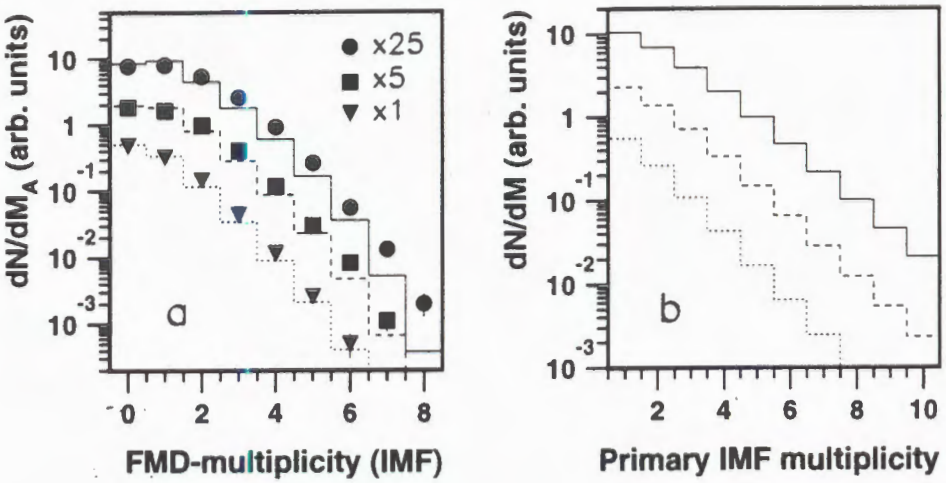

Fig.1. Left: measured IMF-multiplicity distributions associated with a trigger fragment of charge $6 \le Z \le 20$ for p + Au collisions at 8.1 GeV (circles, solid line), 3.6 GeV (squares, dashed line), 2.16 GeV (triangles, dotted line). They are fitted with Fermi-like primary distributions (right picture), folded with the experimental filter

The right side of this equation can be also found from the coincidence rate n_{12} for IMF's in the triggering telescopes:

$$\frac{n_{12}}{n_1 p_2} = \frac{\langle M^2 \rangle}{\langle M \rangle} - 1. \tag{4}$$

Here n_1 is counting rate in telescope 1, p_2 is the detecting probability for the coincident fragment in telescope 2. Using eqs.(3) and (4) one can find the efficiency of the fragment multiplicity detector ε. This is the way to control the calculation of ε:

$$\varepsilon = \langle M_A \rangle \frac{n_1 p_2}{n_{12}}. \tag{5}$$

We used the coincidence data for the telescopes located at θ equal to 68°, 87°, and 112°. For that geometry the probability p_2 is largely determined by the solid angle of telescope 2. The correction for the IMF-IMF angular correlation is around 6%. The FMD efficiency found with (5) differs only by 7% from the calculated one, and that is within the counting rate statistics of coincidences.

How to get the primary multiplicity distribution $W(M)$ from the measured one $W(M_A)$? The first way is fitting the parametrized $W(M)$, folded by the experimental filter according to (1), to the experimental distribution. It was done assuming $W(M)$ to be shaped like a Fermi function. This choice was motivated by calculations using the statistical model of multifragmentation (see below). The results are presented in Fig.1b. The mean values of the primary IMF multiplicities (for the events with at least one IMF) are equal to 1.7 ± 0.2,

1.9 ± 0.2, and 2.1 ± 0.2 for the beam energies 2.16, 3.6, and 8.1 respectively. These values are slightly lower than obtained in paper [14] because a higher FMD efficiency was used*.

Another way (a bit more complicated) is direct reconstruction of $W(M)$ using the reverse matrix $Q^{-1}(M, M_A)$:

$$W(M) = \sum_{M_A=0}^{M-1} Q^{-1}(M, M_A)\, W(M_A). \qquad (6)$$

The matrix Q^{-1} is obtained by solving the equation $Q \cdot Q^{-1} = 1$. Directly reconstructed $W(M)$ are close in shape to those shown in Fig.1b. They are presented in Fig.2 together with the ones calculated by the statistical multifragmentation model.

Comparison with Model Calculations

The reaction mechanism for the relativistic projectiles is divided into two steps. The first one consists of a fast energy deposition stage, during which very energetic light particles are emitted and the nuclear remnant (spectator) is excited. The second one is the decay of the target spectator. The fast stage is usually described by the intranuclear cascade model (INC). We use a version of the INC from Ref.18 to get the distributions of the nuclear remnants in charge, mass and excitation energy. The second stage is described by the statistical multifragmentation model (SMM) [19]. The statistical behaviour of the target spectator is evident from the fact that the angular distributions of IMF's and their energy spectra at different angles are well described in the framework of the statistical decay of a thermalized moving source [20]. Within the SMM the probabilities of different decay channels are proportional to their statistical weights. The break-up volume determining Coulomb energy of the system is taken to be $V_b = (1 + k)A/\rho_0$, where A is the mass number of the decaying nucleus, ρ_0 is the normal nuclear density, k is a model parameter. So, thermal expansion of the system before the break-up is assumed. The primary fragments are hot, and their deexcitation is taken into account to get final IMF distributions. In further calculations we use $k = 2$ based on our analysis of the correlation data [12]. This value corresponds to the break-up density $\rho_b \approx 1/3\rho_0$. The upper dashed line in Fig.3 is obtained by means of this combined model. The calculated mean multiplicity for the highest energy is almost two times larger than the experimental one indicating a significant overestimation of the excitation energy of the residual nucleus. For the lowest beam energy the calculated mean multiplicity is still larger than the experimental one though not so much.

The shortcoming of the INC algorithm is that the exciton approach doesn't provide a reliable calculation of excitation energy in case when many nucleons are involved in the cascade stage. The use of the preequilibrium exciton model (PE) [21] together with the INC results in significant decreasing excitation energy of the target spectator and reducing mean IMF multiplicities (lower dotted line in Fig.3). The calculated value of $\langle M \rangle$ at the beam

*In the light of these results the IMF multiplicities in helium-induced reaction [5] were remeasured: $\langle M \rangle = 2.2 \pm 0.2$ for 14.6 GeV.

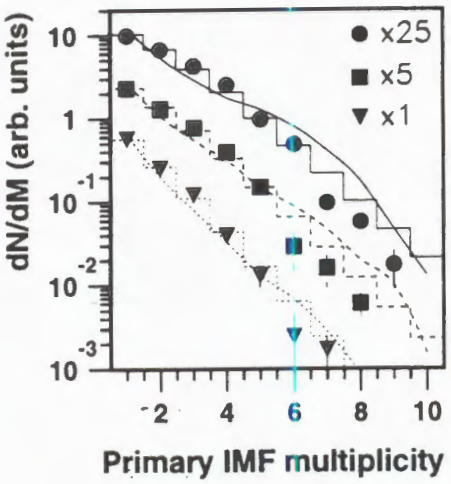

Fig.2. Primary IMF distributions. Symbols are for directly reconstructed distributions: circles, squares and triangles are for the beam energies 8.1, 3.6, 2.16 GeV respectively. Histograms are from Fig.1b, the smooth lines are calculated with the statistical multifragmentation model (see the text)

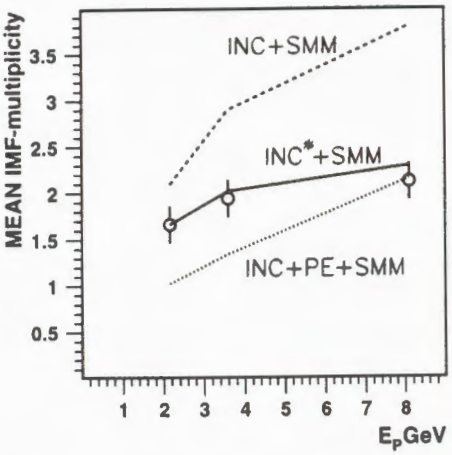

Fig.3. Mean IMF multiplicities as a function of the beam energy. Open points are experimental data. Dashed and dotted lines are drawn through the values calculated with INC + SMM and with INC + PE + SMM at the beam energies used. The solid line is obtained with the use of modified INC* followed by SMM

energy of 8.1 GeV coincides with the experimental one, but, as will be shown below, the model-predicted fragment kinetic energies are significantly lower than the measured ones. It means that the model underestimates the Z value of the target residue, as the fragment kinetic energies are determined in the main by the Coulomb field of the source [12]. With decreasing beam energy, the calculated mean IMF multiplicities fall rather fast approaching 1 at $E_p = 2.16$ GeV. The reason for that is the model underestimation of the spectator excitation energy. So, the use of the INC or INC + PE does not solve the problem of describing the properties of a target spectator for a wide range of projectile energies, and one should look for an alternative approach. The authors of [22] came to a similar conclusion and used some phenomenological distributions of the mass numbers and the excitation energies of a source to describe multifragmentation of spectators in relativistic heavy-ion reactions.

The solid line in Fig.3 was calculated using the empirical modified intranuclear cascade model (INC*) followed by SMM. In this modification the masses and charges of the residual are kept unchanged, as given by INC, but the excitation energies are α times reduced. The parameter α was taken to be equal to the ratio of the experimental mean IMF multiplicity to the calculated one in INC + SMM:

$$\alpha = \frac{\langle M_{\text{exp}} \rangle}{\langle M_{\text{INC + SMM}} \rangle} . \qquad (7)$$

Table. The calculated properties of the nuclear remnants in p + Au collisions

E_p, GeV	Exper. $\langle M_{IMF} \rangle$	Calculations							Model
		$\langle M_{IMF} \rangle$	Z_R	A_R	Z_{MF}	A_{MF}	E_R^*	E_{MF}^*, MeV	
8.1	2.1 ± 0.2	3.80	74	180	70	168	524	911	INC + SMM
		2.15	67	163	50	121	204	526	INC + PE + SMM
		2.29	74	180	69	164	289	591	INC* + SMM
3.6	1.9 ± 0.2	2.90	76	185	73	176	407	757	INC + SMM
		1.34	70	171	55	134	148	385	INC + PE + SMM
		2.02	76	185	73	174	285	582	INC* + SMM
2.16	1.7 ± 0.2	2.09	77	188	75	181	328	642	INC + SMM
		1.02	72	176	62	145	119	266	INC + PE + SMM
		1.66	77	188	75	180	262	543	INC* + SMM

Z_R, A_R, E_R^* are the charge, mass number and excitation energy averaged over all the target spectators.

Z_{MF}, A_{MF}, E_{MF}^* are the same, but averaged over the residues decaying with IMF emission.

This is motivated by the model correlation between $\langle M \rangle$ and the spectator excitation energy. We are aware that such a modification must be accompanied by corresponding changing of parameters of the cascade outgoing particles. However in the present paper we are concentrated only on reproduction of multifragmentation phenomena. So, the solid curve in Fig.3 is obtained with the parameter α equal to 0.8, 0.7, and 0.55 for the beam energies 2.16, 3.6, and 8.1 GeV respectively. It goes very close to the data.

The table summarizes the results of the calculations. Note that according to the INC* + SMM model, the mean excitation energy of the residues E_R^* is changed only slightly (from 285 to 289 MeV) when the beam energy varies from 3.6 to 8.1 GeV. This saturation effect was noted already in papers [7,8] for ^{3}He interactions (up to 4.8 GeV) with silver. The IMF emission takes place on the tail of the excitation energy distribution, therefore the mean excitation of the fragmenting nuclei is approximately twice as large.

The model-calculated IMF multiplicity distributions (for the case of INC* + SMM) are shown in Fig.2 together with the reconstructed experimental ones.

Energy Spectra and Charge Distributions of IMF

Figure 4 presents the comparison of the mean kinetic energies of fragments (measured at the beam energies of 2.16 and 8.1 GeV) with the calculated ones. The data are obtained with the telescope located at $\theta = 87°$ and corrected for the detection threshold (E/A = 1.2 MeV). The measured mean energies for the lower beam energy are slightly higher than

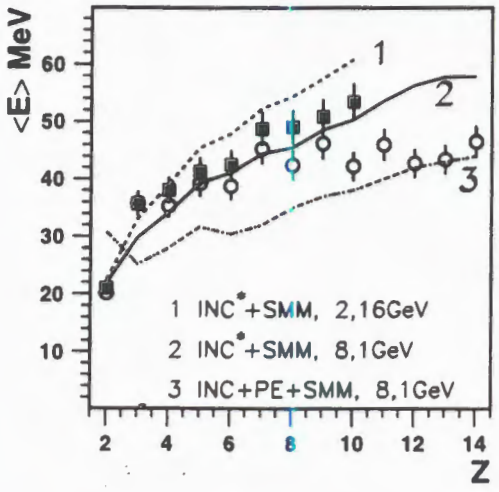

Fig.4. Mean kinetic energies of fragments in p + Au collisions at 2.16 GeV (solid points, line 1) and 8.1 GeV (open points, lines 2,3). The lines are calculated with modified INC* + SMM (1,2) and INC + PE + SMM (3)

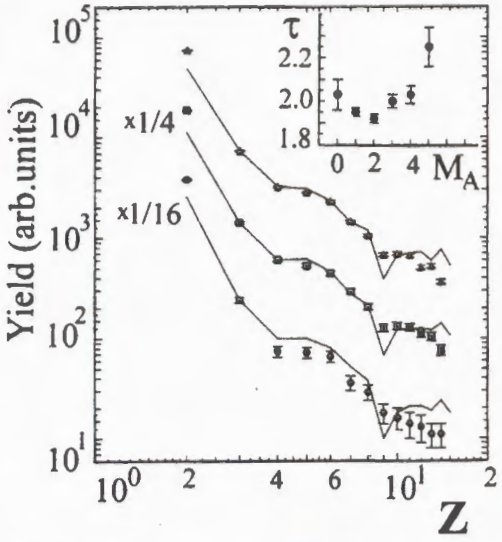

Fig.5. Fragment charge distributions measured at $\theta = 87°$ for the beam energies 8.1 GeV (top), 3.6 GeV (middle) and 2.16 GeV (bottom). The lines are calculated by INC* + SMM (normalized at $Z = 3$). The insert gives the τ-parameter deduced from the IMF-charge spectra for the beam energy 8.1 GeV

those for $E_p = 8.1$ GeV. This is caused, in the main, by the larger charge of the decaying nucleus for the lower beam energy.

Let us first consider the region $Z_{IMF} \leq 9$. The calculations using the INC + PE + SMM model for $E_p = 8.1$ GeV give definitely lower mean energies than the experimental ones indicating the model underestimation of the target spectator Z and A. The calculated mean energies are close to the data when modified INC* followed by SMM is used. For $E_p = 2.16$ GeV, Fig.4 presents the results obtained with the modified intranuclear cascade model. The calculated values are slightly above the experimental ones.

Let us consider the data for heavier fragments shown for $E_p = 8.1$ GeV. For $Z > 9$ IMF-energies practically do not change in contrast to the model prediction. It could be explained by dominating of channels with small number of IMF's. For these channels the break-up volume may not be constant and may increase with the IMF's size; it needs an additional analysis. Another possible explanation of this observation is the failure of the SMM assumption that the fragments have equal probabilities to be formed at any available place inside the break-up volume. In fact, the interior of the expanded nucleus is favoured over the diffuse edge for the appearance of larger IMF's as the fragments are formed via the density fluctuations. This results in lower Coulomb energies for them with respect to

the model prediction. This observation presents additional evidence for the volume emission of the fragments. A similar conclusion was made in [23].

Figure 5 shows the charge distributions of IMF's. The calculations in the INC* + SMM model resemble the general behaviour of the data. The empirical power law $Y(Z) \sim Z^{-\tau}$ describes the data also well. In the insert of Fig.5 the dependence of the τ-parameter on the associated IMF-multiplicity M_A is shown: with increasing multiplicity, the τ-parameter goes down and further goes up. In the earlier papers on the multifragmentation [23,24] the power law for the fragment charge yield was interpreted as an indication of the proximity to the ciritical point for the liquid-gas phase transition in nuclear matter. But in fact the fragmenting system is not so close to the critical point [25] and one should look for a less exotic explanation of the power law behaviour of $Y(Z)$. Probably a convenient interpretation can be found in a more correct consideration of the secondary decay of excited fragments. As was already mentioned, the IMF multiplicity is correlated with the excitation energy of the system. For the low multiplicities the system is close to the evaporation regime. In this case increasing excitation energy results in enhancement of the yield of heavier fragments (τ falls down). As the excitation continues increasing, the secondary decay of the fragments becomes more significant, enhancing the yield of lighter fragments (τ goes up).

It was mentioned in the introduction that the IMF + IMF angular correlation gives important information on the emission time. In this work we obtained a correlation function $R(\theta_{12})$ from the coincidences between the trigger telescopes and the PM's of the fragment multiplicity detector at the beam energy of 8.1 GeV. The correlation function shows a minimum at $\theta_{12} \approx 0$ caused by the Coulomb repulsion between fragments. The magnitude of the small angle suppression is practically the same as for collisions ^{4}He (14.6 GeV) + Au [12,13]. This means that the IMF emission time for proton-induced multifragmentation does not exceed 100 fm/c as in collisions He + Au. Detailed analysis of the angular correlations will be presented in a separate publication.

Conclusion

Multiple emission of intermediate mass fragments has been studied for the collisions p + Au at the beam energies 2.16, 3.6, and 8.1 GeV with the modified FASA set-up. The mean IMF multiplicities are equal to 1.7 ± 0.2, 1.9 ± 0.2, and 2.1 ± 0.2 respectively. The intranuclear cascade calculations with or without preequilibrium emission do not solve the problem of describing the properties of a target spectator for the projectile energies used. The epxerimental data on the IMF multiplicity and charge distributions as well as fragment kinetic energies are described with the empirically modified intranuclear cascade calculations followed by the statistical multifragmentation model. The present data support a scenario of true thermal multifragmentation of a hot and expanded nuclear system.

The authors are thankful to Prof. A.Hrynkiewicz, A.M.Baldin, S.T.Belyaev and E.Kankeleit for support. The research was supported in part by Grant No.RFK300 from the International Science Foundation and Russian Government, Grant No.96-02-18952 from Russian Foundations for Basic Research, by Grant No.94-2249 from INTAS, by Grant

No.P30B 09509 from Polish State Committee for Scientific Research, by Contract No.06DA453 with Bundesministerium für Forschung und Technologie and by the US National Science Foundation.

References

1. Lynch W.G. — Ann. Rev. Nucl. Part. Sci., 1987, v.37, p.493.
2. Moretto L.G., Wozniak G.J. — Ann. Rev. Nucl. Part. Sci., 1993, v.43, p.379.
3. Bondorf J.P. et al. — Phys. Reports, 1995, v.257(3), p.133.
4. Avdeichikov V.V. et al. — Yad. Fiz., 1988, v.48, p.1796.
5. Lips V. et al. — Phys. Rev. Lett., 1994, v.72(11), p.1604.
6. Pienkovski L. et al. — Phys. Lett., 1994, v.B336, p.147.
7. Morley K.B. et al. — Phys. Rev., 1996, v.C54(2), p.737.
8. Foxford E.R. et al. — Phys. Rev., 1996, v.C54(2), p.749.
9. Viola V.E., Kwiatkowski K. — Progress Report INC-40007-112, Indiana University, Bloomington, 1996.
10. Tanaka K.H. et al. — Nucl. Phys., 1995, v.A583, p.581.
11. Schapiro O., Gross D.H.E. — Nucl. Phys., 1994, v.A573, p.143.
12. Shmakov S.Y. et al. — Yad. Fiz., 1995, v.58(10), p.1735; (Phys. of Atomic Nucl., 1995, v.58(10), p.1635).
13. Lips V. et al. — Phys. Lett., 1994, v.B338, p.141.
14. Karnaukhov V.A. et al. — JINR Preprint E1-96-50, Dubna, 1996.
15. Avdeyev S.P. et al. — Pribory i Tekhnika Eksper., 1996, v.39(2), p.7; (Instr. Exp. Techn., 1996, v.39(2), p.153).
16. Avdeyev S.P. et al. — Nucl. Instr. Meth., 1993, v.A332, p.149.
17. Stracener D.W. et al. — Nucl. Instr. Meth., 1990, v.A294, p.485.
18. Toneev V.D., Gudima K.K. — Nucl. Phys., 1983, v.A400, p.173c.
19. Botvina A.S., Iljinov A.S., Mishustin I.N. — Nucl. Phys., 1990, v.A507, p.649.
20. Karnaukhov V.A. et al. — In: Proc. of Int. Conf. «Low Energy Nucl. Dynamics» St. Petersburg, ed. Yu. Oganessian, World Scientific, Singapore, 1995, p.423.
21. Blann M. — Ann. Rev. Nucl. Sci., 1975, v.25, p.123.
22. Botvina A.S. et al. — Nucl. Phys., 1995, v.A584, p.737.
23. Hirsch A.S. et al. — Phys. Rev., 1984, v.C29, p.508.
24. Siemens P.J. — Nature, 1983, v.305, p.410.
25. Karnaukhov V.A. — JINR Preprint E7-96-182, Dubna, 1996; Yad. Fiz., 1997, v.60(10).

Received on February 27, 1997.

УДК 539.172.13

SEARCH FOR EFFECTS OF THE OZI RULE VIOLATION IN φ AND ω MESONS PRODUCTION IN POLARIZED DEUTERON BEAM INTERACTION WITH POLARIZED PROTON TARGET (PROJECT DPHE3)

V.Yu.Alexakhin, N.Angelov, S.N.Filippov[1], F.F.Guber[1], A.B.Kurepin[1], V.P.Nomokonov, E.A.Pasyuk, N.M.Piskunov, M.G.Sapozhnikov, I.M.Sitnik, E.A.Strokovsky, Yu.A.Usov

It is proposed to verify the predictions of the intrinsic polarized nucleon strangeness model by investigation of the reaction $\vec{d}+\vec{p}\rightarrow{}^3\mathrm{He}+\varphi$ with different deuteron and proton spin orientations. This reaction is very convenient to make such a test because of large momentum transfer and since the substantial OZI rule violation has been already found for this reaction at SATURNE II for the non-polarized proton and deuteron. The predictions of the model are very clear: the φ production should be increased with parallel deuteron and proton spins orientation and suppressed with antiparallel one. We propose to perform measurements using the polarized deuteron beam from the JINR Nuclotron and the BES spectrometer with a movable polarized proton target.

The investigation has been performed at the Laboratory of Nuclear Problems, JINR.

Поиск эффектов нарушения правила ОЦИ в рождении φ- и ω-мезонов во взаимодействии пучка поляризованных дейтронов с поляризованной протонной мишенью (проект DPHE3)

В.Ю.Алексахин и др.

Предлагается проверка предсказаний модели поляризованной внутренней странности в нуклоне с помощью изучения реакции $\vec{d}+\vec{p}\rightarrow{}^3\mathrm{He}+\varphi$ с различными ориентациями спинов дейтрона и протона. Изучение этой реакции имеет ряд преимуществ для проверки предсказаний этой модели, а именно: сильное нарушение правила ОЦИ с неполяризованными начальными частицами уже обнаружено в экспериментах на САТУРН II. Предсказания модели очень четкие: выход φ должен быть усилен при параллельной ориентации спинов дейтрона и протона и подавлен при их антипараллельной ориентации. Предлагается использовать пучок поляризованных дейтронов от нуклотрона ОИЯИ и спектрометр БЕС с передвижной поляризованной протонной мишенью.

Работа выполнена в Лаборатории ядерных проблем ОИЯИ.

[1]Institute for Nuclear Research, Troitsk

1. Physical Motivation

According to the naive quark models, the proton wave function contains just two u quarks and one d quark. This model gives a good general picture of the hadron structure at large distances, while probes of a shorter distance reveal more constituents like a sea of $\bar{q}q$ ($q = u, d, s$) pairs and gluons, qualitatively as expected on the basis of perturbative QCD. However, there are now some experimental indications that the proton wave function can contain a substantial fraction of $\bar{s}s$ pairs.

The presence of $\bar{s}s$ pairs in the nucleon was first indicated by measurements of the charm production in the deep-inelastic neutrino scattering and low energy πN scattering data on the σ term. The magnitude of the strange quark contribution varies for different nucleon matrix elements. Thus the fraction of the nucleon momentum carried by the strange quarks is $(4.08 \pm 0.41)\%$ [1]. The contribution of the strange quarks in the nucleon mass is surprisingly high $m_s \langle \bar{s}s \rangle = 190 \pm 60$ MeV [1]. Recently the EMC and successor experiments (SMC, E142, E143) have not only confirmed the indication that such pairs are present, but also indicated that they are polarized. This latter observation has stimulated great theoretical interest (for review, see [1]—[3]). A number of competing explanations appeared and attention was drawn back to some old problems.

Thus the presence of a substantial amount of strange quarks in the nucleon arouses a problem of applicability of the Okubo–Zweig–Iizuki (OZI) rule [4] to processes involving baryons. The OZI rule predicts that diagrams with disconnected quark lines should be suppressed as compared to connected quark diagrams. If there are no strange quarks in the nucleon, then production of the φ meson, for instance in $\bar{p}p$ annihilation, should look like in Fig.1(a). The $\bar{s}s$ pair should be created in the final state, which is absent in the initial state, so φ production is described by the disconnected diagram and should be suppressed. On the contrary, production of the ω meson, which contains only light quarks, could be described by the diagram of Fig.1(b), where the quark lines of the initial state are connected with the final state ones. Therefore, no suppression is expected for ω meson production.

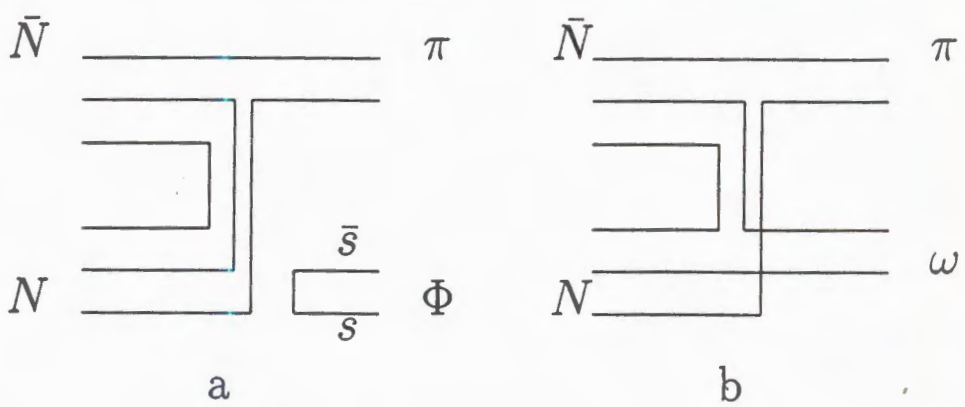

Fig.1. Disconnected quark diagram of φ meson production in $\bar{N}N$ interaction (a). Diagram of ω production in the same process (b)

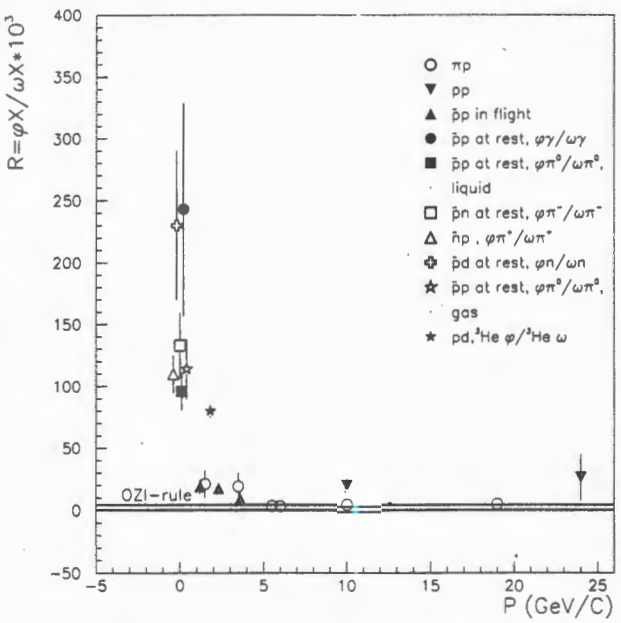

Fig.2. Ratio $R = \varphi X / \omega X$ multiplied by 10^3 for different hadronic interactions

The OZI rule was tested in a number of experiments. The results of these tests are shown in Fig.2, where the ratio $R = \varphi X / \omega X$ multiplied by 10^3 is plotted. One can immediately realize that for pp, πp interactions and $\bar{p}p$ annihilations in flight no strong deviations from the OZI rule prediction was found. However, strong violation of the OZI rule was observed in recent experiments with stopped antiprotons at LEAR (CERN).

The very existence of strong deviation from the OZI rule in annihilation of stopped antiprotons is a firmly established experimental fact seen by different groups in different reactions (for a review, see [5]).

The most striking feature of the OZI rule violation found in the experiments at LEAR is its strong dependence on the quantum numbers of the initial state.

For instance, the OBELIX collaboration have studied the channel $\bar{p}p \to \varphi\pi^0$ for annihilation in hydrogen targets with different densities [6], [7] and not only a large ratio φ/ω was found (30 times higher than the naive OZI rule prediction), but also it turned out that the φ production is 50 times more prominent for annihilation from the triplet initial state than from the singlet one.

Some attempts were made to explain the strong OZI rule violation in $\bar{p}p$ annihilation at rest [8]—[10] on the basis of the traditional ideas, but these approaches are unable to reproduce all the features of φ production observed now. On the contrary, the model of the polarized intrinsic nucleon strangeness [11] provides the physically transparent explanation of the observed spin dependence of the φ yield and predicts some definite tests.

1.1. Polarized Intrinsic Nucleon Strangeness. First of all, it is assumed that the OZI rule itself is valid. Its violation is only apparent and could be regarded as a signal of a complicated nucleon structure. It is supposed [11], [12] that the abundant φ meson production could be the consequence of an admixture of $\bar{s}s$ pairs in the nucleon. In this case the φ production in NN or $\bar{N}N$ interactions is described by the diagarms with connected s-quark lines.

At first glance, the intrinsic strangeness of the nucleon should lead to the same enhancement of the φ production in all annihilation channels. This is in contradiction with the experimental data. To solve this principal difficulty it was assumed [11] that the $\bar{s}s$ component in the nucleon is polarized.

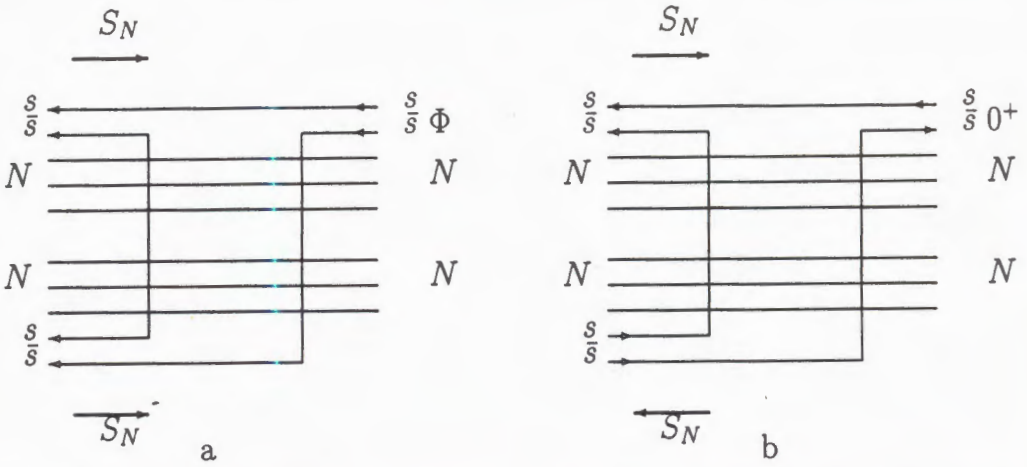

Fig.3. Production of the φ meson in *NN* interaction from the spin-triplet (a) and spin-singlet (b) states. The arrows show the direction of nucleons and strange quark spins

Indeed, the results from the deep inelastic lepton-nucleon experiments indicate that strange quarks and antiquarks in the nucleon have a net polarization opposite to the proton spin [13]:

$$\Delta s \equiv \int_0^1 dx\,[q_\uparrow(x) - q_\downarrow(x) + \bar{q}_\uparrow(x) - \bar{q}_\downarrow(x)] = -0.10 \pm 0.03. \qquad (1)$$

Adopting this observation from the deep inelastic scattering one may ask what happens if the nucleon wave function, even at small momentum transfers, contains an admixture of $\bar{s}s$ pairs with spin of both strange quarks oriented opposite to the nucleon spin.

Let us consider *NN* interaction from a spin-triplet initial state in which the nucleon spins are parallel (see Fig.3). In this case the $\bar{s}$ and s quarks in both nucleons will also have parallel spins. If the rearrangement diagram of Fig.3 is dominant and the polarization of the strange quarks is not changed during the interaction, then the $\bar{s}$ and s quarks will have parallel spins in the final state as in the quark-model wave function of the φ meson. If the *NN* initial state is an *S* state, the $\bar{s}s$ pair will probably also be in an *S* wave as in the φ meson. Therefore, the maximum enhancement of φ production is expected in the $^3S_1$ channel, as observed in the $\bar{p}p \to \varphi\pi$ channel. If the initial *NN* state is spin singlet, then the rearrangement diagrams like that in Fig.3b may lead to the system in the final state also in the spin-singlet state, but that is not a φ meson.

This model also qualitatively suggests why φ production may be more enhanced in $\bar{p}p$ annihilation at rest than in other hadronic interactions. The reason is that higher energy collisions involve an increasing admixture of partial waves, implying that the «rearrangement» into the $\bar{s}s$ spin-triplet *S*-wave state of the φ meson becomes progressively more

diluted. On the contrary, in the $\bar{p}p$ annihilation at rest only one pure spin state $^3S_1$ is possible for $\varphi\pi$ production in S-wave annihilation.

An important step was made in [12], where arguments were given on the basis of chiral symmetry that the $\bar{s}s$ pair in the nucleon wave function might be in a $^3P_0$ state.

We would like to stress that all tests of the predictions of this model [11] performed up to date gave positive results (for review, see [5]).

1.2. $\vec{d}+\vec{p}\to{}^3\mathrm{He}+\varphi$ *as a Test of the Polarized Proton Strangeness Model.* The spin dependence of the φ yield should manifest itself in polarized proton interactions with polarized deuterons

$$\vec{p}+\vec{d}\to{}^3\mathrm{He}+\varphi. \tag{2}$$

It is predicted [11] that φ production will be enhanced when spins of the proton and deuteron are parallel. When spins of the beam and target particles are oppositely directed, the φ production is predicted to be suppressed.

The φ (and ω) yields in reaction (2) were measured at SATURNE II with the unpolarized beam and target combination [14]. A large deviation from the OZI rule prediction was revealed: $R(\varphi/\omega)=(80\pm 3^{+10}_{-4})\cdot 10^{-3}$.

These results are promising and give credence to study the polarization effects of the OZI rule violation in these processes. The main physical advantage of ^{3}He production reactions (2) is that they provide a possibility of studying OZI rule violation in the high-momentum transfer region.

Recently the $pd\to{}^3\mathrm{He}+X$ processes were considered in [16], [17] on the assumption that the meson X production is going on via a two-step mechanism involving the subprocesses $pp\to d\pi$ and $\pi N\to XN$. In this scheme the φ production occurs not in NN interaction but in πN one.

Numerically, the calculations of [16] underestimate the cross sections of φ and ω production by a factor of 2.4. In [17] it is stressed that the absolute value of the cross section is very sensitive to the spin structure of the elementary amplitudes and underestimates the cross sections of φ and ω production by a factor of 10. Thus, one could conclude that this simple two-step mechanism alone is responsible for ^{3}He production. In principle, there are different possibilities of matching high momentum transfer of ^{3}He with the deuteron formfactor.

It is remarkable that the «standard» two-step model of ^{3}He production in reaction (2) predicts completely different behavior of the φ yields. It was calculated [17] that if vector mesons are created via the $pp\to d\pi$ and the $\pi N\to XN$ chain, then they should be produced mainly from the antiparallel orientation of the proton and deuteron spins. The value of the asymmetry

$$A=\frac{Y(\uparrow\uparrow)-Y(\uparrow\downarrow)}{Y(\uparrow\uparrow)+Y(\uparrow\downarrow)} \tag{3}$$

(where Y is the ^{3}He yield for the parallel and antiparalel orientations of the spins of protons and deuterons) near the threshold is expected to be $A = -0.95$. The intrinsic polarized strangeness model predicts that A should be positive. Thus, it would be extremely interesting to perform these measurements.

It is important to compare characteristics of φ production with those for ω meson. The effects of nuclear dynamics of ^{3}He formation with φ and ω mesons should be rather similar. The ω production would be a nice reference point providing information on standard mechanisms of the vector meson production.

It is expected that the ratio of φ/ω cross sections should be high and the asymmetry (3) would be positive and large for the φ production.

2. The Experimental Apparatus

2.1. Selection of the Reactions with φ(ω) Mesons. The polarized deuteron beam with a proper momentum of about 5 GeV/c will be available at the JINR Nuclotron. The polarized proton target was already installed and the first experiments with it have been done [18], [19].

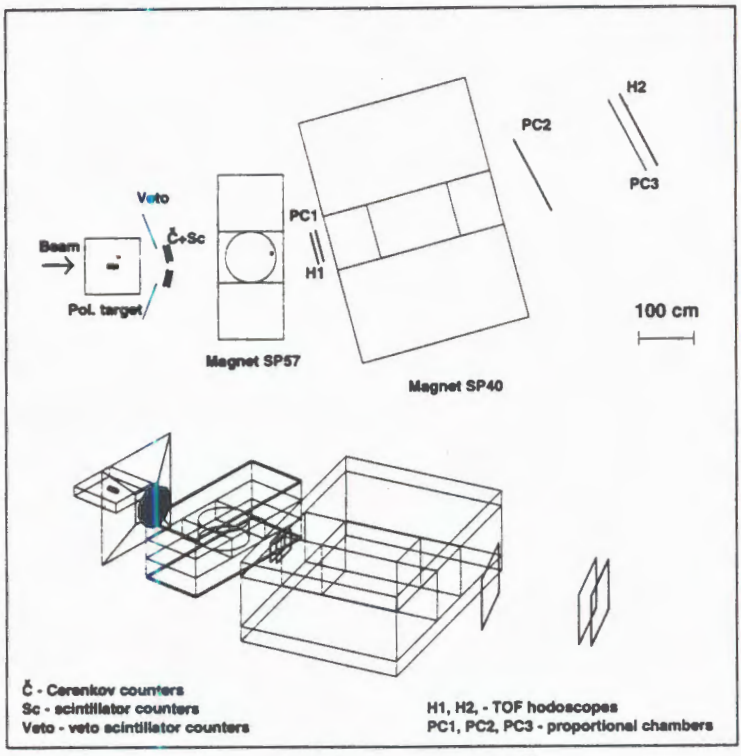

Fig.4. General layout of the proposed apparatus

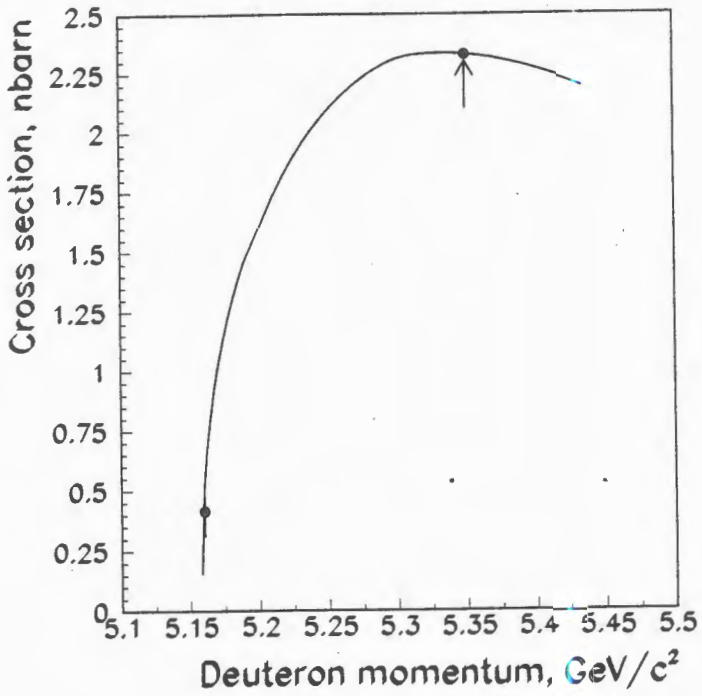

Fig.5. Cross section of the $dp \to {}^3\mathrm{He}\varphi$ reaction as a function of the deuteron momenta scaled in accordance with the experimental data (see the text). The arrow indicates the chosen point

The BES magnetic spectrometer [20], which is under development at LHE JINR, will be used for measurements of ^{3}He in the reactions:

$$\vec{d} + \vec{p} \to {}^3\mathrm{He} + \varphi, \tag{4}$$

$$\vec{d} + \vec{p} \to {}^3\mathrm{He} + \omega. \tag{5}$$

The general layout of the apparatus is shown in Fig.4. It consists of magnets SP57 and SP40, proportional chambers, TOF hodoscopes, scintillator and Cherenkov counters.

The binary reactions (4), (5) will be selected by a peak in the missing mass spectrum of ^{3}He.

As a working point we choose the deuteron momentum 5.35 GeV/c. In [17] the cross section of reaction (2) as a function of the beam energy was calculated. This dependence for reaction (2) as a function of incident deuteron momentum was scaled in accordance with the experimental data [14] and shown in Fig.5. The arrow indicates the chosen point on momentum.

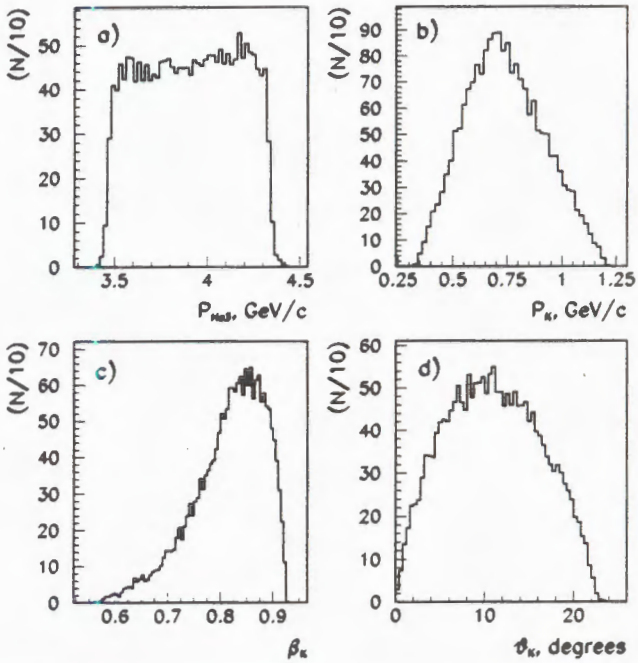

Fig.6. Kinematic characteristics of the φ production reaction: (a) ^{3}He momentum distribution; (b) kaon momentum distribution; (c) distribution on β for kaons; (d) distribution in scattering angles for kaons

One could see that the cross section reaches its maximum just at this point. This momentum in the laboratory system corresponds to the c.m.s. momentum of 258 MeV/c in the φ production reaction (4). The same c.m.s. momentum for ω production (5) corresponds to the initial deuteron momentum of 4.37 GeV/c.

In Fig.6. the kinematic characteristics of the φ production reaction (4) are shown. The momentum distribution of ^{3}He is shown in Fig.6(a), the ^{3}He momenta are in the range 3.5—4.4 GeV/c. The momentum distribution of kaons from the φ decay is shown in Fig.6(b). It is peaked at 700 MeV/c. The corresponding distribution in the velocity β of the kaons is shown in Fig.6(c). One can see that most kaons have $\beta < 0.9$. The angular distribution of the kaons is shown in Fig.6(d). The kaon scattering angles are confined within 20°.

It is assumed to detect the ^{3}He nucleus and to measure its angle and momentum. Then φ(ω) mesons could be selected by the peak in the missing mass spectrum.

The Monte-Carlo simulation of the reactions under investigation was performed. The momentum resolution of the BES spectrometer was assumed to be 1% and the angular resolution was taken as 0.1°.

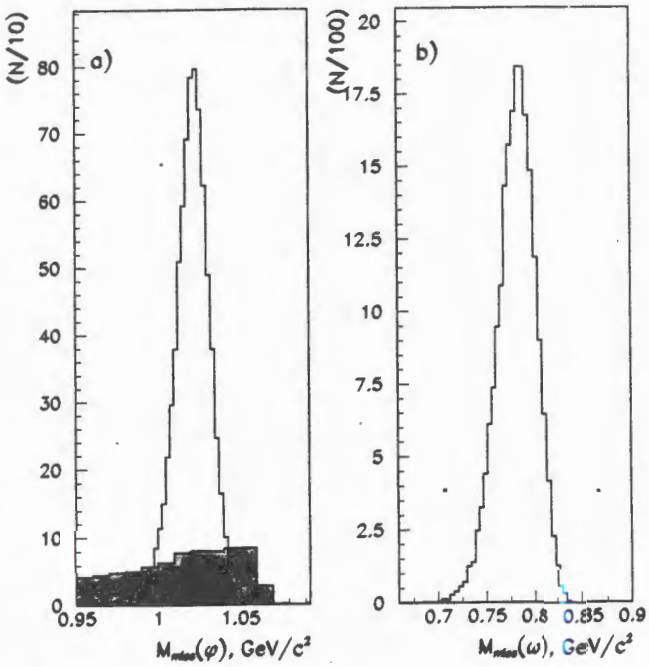

Fig.7. Missing mass distribution: (a) in the φ production reaction, the hatched area corresponds to the reaction on the bound nucleus; (b) in the ω production reaction

In Fig.7 the simulated missing mass spectra for reactions (4), (5) are shown. One could see that smearing of the φ and ω peaks due to the detector resclution and energy losses in the 20-cm-thick polarized target is not dramatic. The narrow peaks with $\sigma_\varphi = 9 \pm 1$ MeV and $\sigma_\omega = 25 \pm 1$ MeV (when fitted by a Gaussian) are seen.

The ^{3}He nuclei will be separated from the background with the time-of-flight and charge identification systems of the BES spectrometer.

2.2. Analysis of the Background Reactions. As was pointed out, the φ and ω mesons should manifest themselves as the peaks in a missing mass spectrum with respect to ^{3}He. However, there is a significant background from other reactions, particularly from the reaction $\vec{d} + \vec{p} \to {}^3\mathrm{He} + n \cdot \pi$. To evaluate the background a Monte-Carlo simulation of one of the most important background channels

$$\vec{d}\vec{p} \to {}^3\mathrm{He}\,\pi^+\pi^-\pi^0\pi^0 \tag{6}$$

has been done. In Fig.8(a) the pion momentum distribution is shown. The pions from reaction (6) have a rather broad distribution peaked at 300 MeV/c. The corresponding distribution in the velocity β is shown in Fig.8(c). Though the low-β tail for pions is not

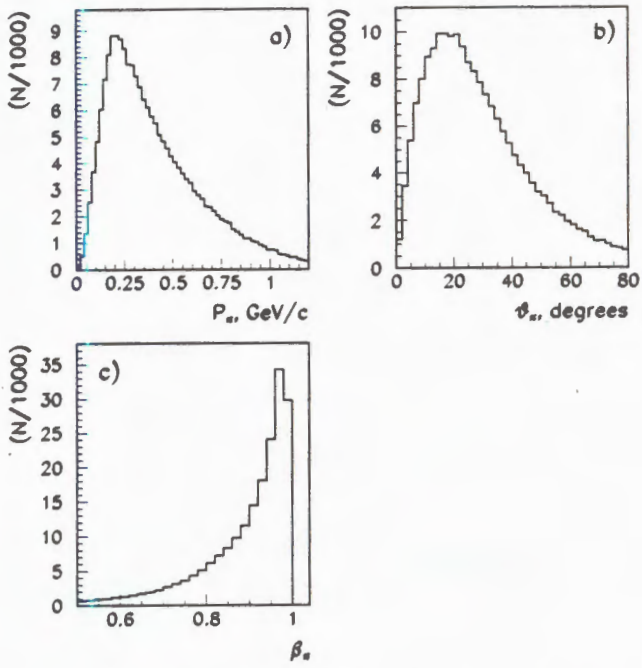

Fig.8. Momentum distribution of pions in the background reaction (a), distributions in scattering angle (b) and β (c)

negligible, most of them have $\beta > 0.9$, while most of kaons from φ decay have $\beta < 0.9$ (Fig.6(c)). The distribution of the pion scattering angles is shown in Fig.8(b). It is significantly broader than the corresponding distribution for the kaons (Fig.6(d)). Thus, it is quite natural to use angular, velocity and multiplicity cuts for the background suppression.

We also investigated reaction (2) on bound, not polarized protons. It appears that the peak from the φ meson in the missing mass spectra is strongly smeared because of the Fermi motion (see Fig.7(a), hatched area). Our estimations show that the signal from the reaction on a free proton is about 14 times higher than from the reaction on bound proton, if both distributions are integrated within the $m_\varphi \pm 3\sigma$ interval.

The practical scheme of the background suppression is proposed as follows. The array of the Cherenkov counters followed by a similar array of thin scintillator counters is placed downstream the target in front of the BES spectrometer. This detector array covers the scattering angle range $5° < \theta < 20°$. It allows one to select events with two slow charged particles within the defined angular range. Besides this detector system, a veto detector covering the angular range $\theta > 20°$ is installed. This detector will reject background events with charged particles scattered at large angles.

It is proposed to use the total internal reflection to construct the Cherenkov detector, because the velocity threshold was chosen as 0.9, which corresponds to $n = 1.11$. Only gases and aerogels could have such a refractive index, but construction of gas counters is difficult

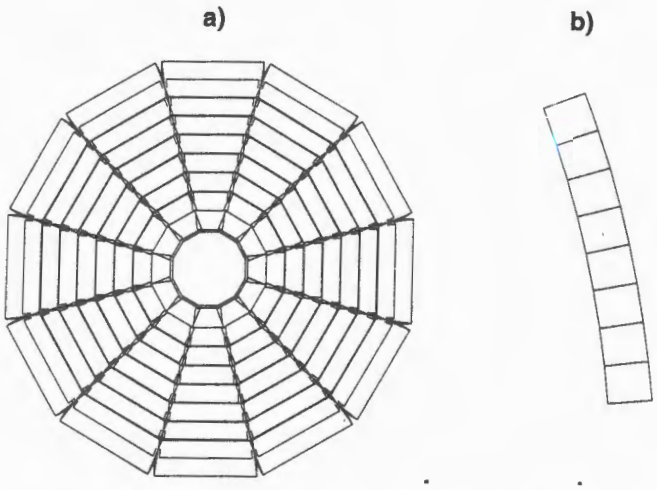

Fig.9. Array of the Cherenkov counter as seen from the beam direction (a) and the lateral view of a single counter (b)

and aerogels with the needed n are not available. The proposed Cherenkov detector (see Fig.9) will consist of twelve trapezoids. It will be placed downstream the target around the beam axis leaving a hole for the beam passage.

Each trapezoid will be made of one-piece plexiglas and specially machined to give it a complex shape, namely it will consist of nine segments each covering 1.7° in θ-angle and having its own slope angle to the beam axis to provide the best discrimination in β. The slope angles for each segment were optimized by our Monte-Carlo simulation.

The trapezoids will have a reflective front side (viewing the target) and their both lateral sides will be in contact with two adjoining trapezoids. All trapezoids will be attached to the photomultiplier tubes from the external side. The similar structure — a set of 10-mm-thick plastic scintillator detectors — will be placed just behind the Cherenkov counter. This structure will cover the angular range $5° < \theta < 20°$. The rest of the solid angle will be covered by the veto detector. It consist of four 10-mm-thick plastic scintillator segments.

The trigger will require the presence of a ^{3}He nucleus and the absence of signals in the veto counters, while in the off-line analysis we will take events with two signals in the scintillator counters and without signals in the Cherenkov counter.

The performance of the proposed set-up was estimated by the Monte-Carlo simulation. To evaluate the suppression factor we generated $2 \cdot 10^6$ events of the background channel (6) and the same number of events for this reaction on bound nucleons.

Just 0.05% of the events from the reaction (6) and 0.025% from reaction on bound nucleons pass through the set of cuts on the velocity ($\beta < 0.9$), multiplicity ($N = 2$), angles $5° < \theta < 20°$ and the requirement of ^{3}He nucleus detection. The channels with higher multiplicity have lower cross sections and the channels with lower multiplicity have fast

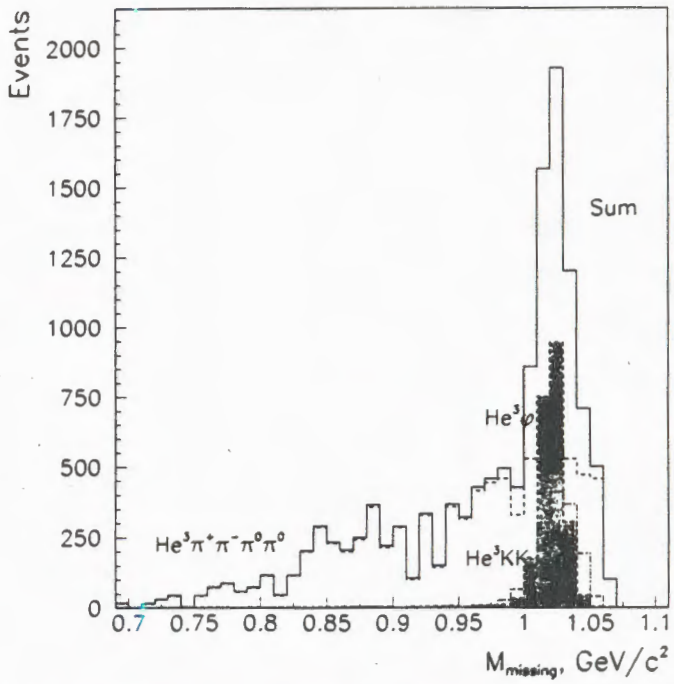

Fig.10. Expecting missing mass distribution for the φ production reaction and background reactions after selection cuts on the velocity and multiplicity

pions and will be suppressed by the Cherenkov detector more strongly. Therefore the background suppression of $10^3 - 10^4$ seems to be feasible.

In Fig.10 the missing mass distribution for the φ production reaction is compared with the background reactions (6) and $dp \to {}^3\mathrm{He}\,K^+K^-$. It was assumed that $\sigma(\varphi) = \sigma(K^+K^-) = 10^{-3}\sigma(4\pi)$. The above-mentioned cuts were applied to all reaction channels.

A clear peak from φ is evident.

3. Requests for the Beamline, Polarized Target and Accelerator Time

Thc possible event rate for $p_d = 5.35$ GeV/c was estimated. Assuming the polarized beam intensity $N_d = 10^8\ \mathrm{s}^{-1}$, the polarized target $C_3H_8O_2$ ($L = 20$ cm, $\rho = 0.7\ \mathrm{g/cm}^3$) and the cross section $\sigma = 2.3$ nb, the expected number of φ events is

$$N_\varphi = N_d \cdot \rho_p \cdot L \cdot \sigma \cdot R_{\varphi \to KK} \cdot \varepsilon \cdot d \approx 1160/\mathrm{day},$$

where $R_{\varphi \to KK} = 0.49$ is the probability of φ decay into K^+K^-, $\rho_p = 4.4 \cdot 10^{22}$ is the number of free protons in 1 cm^3, $\varepsilon = 0.150 \pm 0.003$ is the registration efficiency, $d = 0.9$ is the duty factor.

The statistical accuracy of the asymmetry measurements was estimated. To obtain ~ 10000 events (2), 9 days of polarized deuteron beam with the intensity $N_d = 10^8\ s^{-1}$ are needed.

A discussion about possibility of the moving Medium Resolution Spectrometer (MRS) [21] from Los-Alamos to JINR is going on. We would like to stress that the MRS could be used to our investigations.

We are grateful to V.I.Komarov, L.K.Lytkin, L.V.Malinina and Yu.N.Uzikov for extremely useful discussions.

This work is supported in part by the Russian Foundation for Basic Research, grant No.95-02-05807-a.

References

1. Jaffe R.L. — Proc. Conf. Trends in Collider Spin Physics, Trieste, 1995; hep-ph/9603422.
2. Decker R., Nowakowski M., Weidner U. — Fort. Phys., 1993, v.41, p.87.
3. Ellis J., Karliner M. — Proc. Int. School of Nucleon Spin Structure, Erice, 1995; CERN-TH/95-334, 1995, Geneva.
4. Okubo S. — Phys. Lett., 1963, v.B5, p.165.
   Zweig G. — CERN Report No.8419/TH412, 1964.
   Iizuka I. — Prog. Theor. Phys. Suppl. 37, 1966, v.38, p.21.
5. Sapozhnikov M.G. — JINR Preprint E15-95-544, Dubna, 1995. Lecture at the XXIX St.Petersburg Winter School on Nuclear Physics and Elementary Particles, Zelenogorsk, 1995, p.252.
6. Ableev V.G. et al. — Nucl. Phys., 1995, v.A594, p.375.
7. The OBELIX collaboration. A.Bertin et al., Proc. HADRON'95 Conference, Manchester, 1995.
8. Locher M.P., Lu Y., Zou B-S. — Z. Phys., 1994, v.A347, p.281.
   Locher M.P., Lu Y. — Z. Phys., 1995, v.A351, p.83.
9. Buzatu D., Lev F. — Phys. Lett., 1994, v.B329, p.143.
10. Zou B.S. — Proc. NAN'95 Conference, Moscow, 1995.
11. Ellis J. et al. — Phys. lett., 1995, v.B353, p.319.
12. Alberg M., Ellis J., Kharzeev D. — Phys. Lett., 1995, v.B356, p.113.
13. The EMC Collaboration, Ashman J. et al. — Phys. Lett., 1988, v.B206, p.364; Nucl. Phys., 1989, v.B328, p.1.
14. Wurzinger R. et al. — Phys. Rev., 1995, v.C51, p.R443.
    Wurzinger R. et al. — Phys. Lett., 1996, v.B374, p.283.
15. the OBELIX Collaboration, Cerello P. et al. — Proc. NAN'95 Conf., Moscow, 1995.
16. Faldt G., Wilkin C. — Nucl. Phys., 1995, A587, p.769; Phys. lett., 1995, v.B354, p.20.
17. Kondratyuk L.A., Uzikov Yu.N. — Pisma v ZhETP, 1996, v.63, p.3.

18. Bazhanov N.A. et al. — Nuclear Instruments and Methods in Physics Research, 1996, v.A372, p.349—351.
19. Adiasevich B.P. et al. — Z. Phys., 1996, v.C71, p.65-74.
20. Sitnik I.M. et al. — JINR Rapid Comm. 1995, 2[70]-95, p.19.
21. Baldin A.A. et al. — JINR Communication B1-1-97-39, Dubna, 1997.

Received on March 21, 1997.

УДК 539.1.074.3

FAST DETECTOR FOR TRIGGERING ON CHARGED PARTICLE MULTIPLICITY FOR RELATIVISTIC NUCLEUS-NUCLEUS COLLISIONS

G.Agakichiev, A.Drees*[1], *P.K.Manyakov, N.S.Moroz, Yu.A.Panebrattsev, S.V.Razin, N.Saveljic*[2], *G.S.Shabratova, S.S.Shimansky, G.P.Škoro*[3], *V.I.Yurevich

The simple and fast detector of charged particle multiplicity for relativistic nucleus-nucleus collision studies is performed. The multiplicity detector has been designed for the first level trigger of the CERES/NA45 experiment to study Pb-Au collisions at CERN SPS energies. The detector has allowed a realization of the 40 ns trigger for selection of events with definite impact parameters. The construction, operation characteristics, method of calibration, and testing results are described in detail.

The investigation has been performed at the Laboratory of High Energies, JINR.

Быстрый детектор для триггера по множественности заряженных частиц для релятивистских ядро-ядерных столкновений

Г.Агакишиев и др.

Создан простой и быстрый детектор множественности заряженных частиц для изучения релятивистских ядро-ядерных столкновений. Детектор множественности разработан для триггера первого уровня эксперимента CERES/NA45 по изучению Pb-Au столкновений при энергиях SPS ускорителя в ЦЕРН. Детектор позволяет реализовать 40 нс триггер для выделения событий с определенными прицельными параметрами. Подробно описаны конструкция, рабочие характеристики, метод калибровки и результаты тестирования.

Работа выполнена в Лаборатории высоких энергий ОИЯИ.

1. Introduction

Ultrarelativistic heavy ion collisions with 160 GeV/n lead beam have been investigated in CERN since November 1994. For study of the events with specific inpact parameter which is not a priori known it is necessary to consider a global feature of an event correlated with centrality. There are two main approaches to get this aim:

[1]University of Heidelberg, Germany.

[2]University of Montenegro, Podgorica, Yugoslavia.

[3]INS «Vinca», Belgrade, Yugoslavia.

1. to measure transverse energy, $dE_T/d\eta$ or beam energy deficiency at zero degree by calorimeter;

2. to study the multiplicity of secondaries that can quite comfortably be done by hodoscope scintillator arrays or by semiconductor detectors with appropriate segmentation.

Both of them were successfully used for the first level triggering for experiments with ultrarelativistic heavy ions.

In this paper we report the fast low-segmented scintillation Multuplicity Detector (MD) designed specially for the first level trigger of the CERES/NA45 double RICH spectrometer at CERN SPS [1] to study Pb-Au collisions at 160 GeV/nucleon. Previous trigger was based on SIPD (SIlicon Pad Detector) [2] with 64 segments and was used for the first level triggering in the CERES experiments with proton and sulphur beams. It provided an interaction trigger sensitive to low multiplicity events for proton beam and an impact parameter selective collision trigger for sulphur beam. The counter was situated immediately behind a Silicon Drift Chamber (SIDC) [3] in the target area of the experiment. The upgrading of the CERES/NA45 spectrometer, with an aim to start the experiments with ultrarelativistic lead-nuclei beam of the SPS, CERN, was performed in a period 1994-95. A new tracking device consisting of a doublet of the SIDC [4] was installed at about 10 cm distance downstream of the target. Simultaneously the SIPD was taken out from the target area with a goal to minimize a mass of materials in the region between the target and the entrance window of the RICH1 detector. A new conception of the trigger detectors was designed. Trigger is based on information from small-mass gaseous Cherenkov beam counters [5] and the scintillation array of the MD. One of the Cherenkov micro-counters is placed in a gap between the target and the SIDC doublet, and it is used for selection of the events with the absence of lead ions behind the target (the interaction trigger). The impact parameter selection is done by multiplicity triggering with the MD, located 5.35 m downstream from the target and about 2 m behind the RICHs. A role of the MD is to measure charged particle multiplicity at mid rapidity region which is in strong correlation with an impact parameter of collision. Very fast, 40 ns, analysis of the MD response leads to high quality selection of useful events and good time synchronization of the trigger signals and a readout of information from the slower main detectors, of the spectrometer such as RICH detectors [6], SIDCs and PC (Pad Chamber). The MD is one of the most important elements in the trigger detector system, but it can also be considered as an independent elements of the spectrometer giving the charged particle multiplicity data for more complete physical analysis of the events.

2. Multiplicity Detector

The MD has to content the following criterions:

1. Active zone of the MD has to cover essential part of midrapidity range corresponding to the maximum of charged particle multiplicity from fireball decay;

2. Analog signal from the MD has to be proportional to the number of charged particles produced in nucleus-nucleus collision;

3. To cover a broad multiplicity range up to a few thousands;

4. A readout and an analysis of the information for trigger signal processing have to be as fast as possible;

5. There has to be very low level of the background contribution to the MD response;

6. To work under the magnetic field generated by the CERES magnet system;

7. To have small mass, to be simple and stable in exploitation for the long term and cheap.

Most of these requirements could be contented by using a plastic scintillator for the MD active zone. Requirements for stability, simplicity and cheapness are equivalent to the requirement to minimize a granularity of the detector. For this problem to be solved special investigations were done with an aim to find the best way for sectioning of the active zone of the MD which could give a standard analog signal per minimum ionization particle (mip) independently of a particle hitting point position. The active zone of the MD for the CERES experiment is a disk made of plastic scintillator of 1 cm thickness and outer diameter of 120 cm with a central hole of 20 cm in diameter. The measurements have shown that the requirement mentioned above can be reached by using the active zone consisting of 24 equal sectors/counters (with an opening angle 15°, each) and with special way of polishing of the scintillator surface. Worked out this way, the MD allows realization of two branches of the logical and analog signals:

— 24 logical signals from counters are used for generation of the minimum bias pretrigger signal corresponding to the lowest level of the multiplicity;

— processing of 24 analog signals provides a possibility to set a threshold on a number of charged particles produced in nucleus-nucleus collision and by this way to organize the main N_{ch}-trigger (multiplicity trigger).

To study collisions with low multiplicity of charged particles the logical mode can be used as a base for trigger signal. In the case of relativistic heavy nuclei collisions, with high multiplicity of secondary particles, the analog mode is used for the main trigger signal. Minimization of background contribution to the MD response is done by fast analog signal processing including summing of pulses from all counters and then 40 ns integration. The sketch of the MD construction is shown in Fig.1. Basic characteristics of the MD are given in the Table.

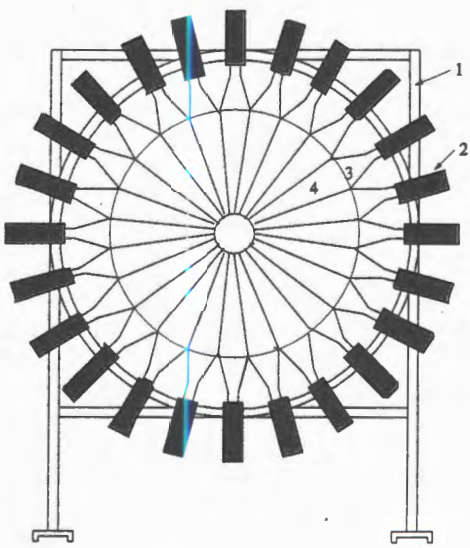

Fig.1. A sketch of the multiplicity detector (1 — mechanical support, 2 — photomultiplier tube within a magnetic shield, 3 — light guide, 4 — plastic scintillator)

Table. Main Characteristics of the Multiplicity Detector

Distance from the target	567 cm
Angular coverage	1.01° — 6.05°
Pseudorapidity region	2.94 — 4.73
Material	plastic scintillator
Thickness	1 cm
Inner diameter	20 cm
Outer diameter	120 cm
No. of sections	24
Photomultiplier	FEU-85

3. Monte Carlo Simulation Results

A research and development stage of the MD design for the CERES expeirment included the analysis of different characteristics of secondary radiation in the MD acceptance. Background conditions and effects were also estimated. For this purpose the VENUS 3.11 [7] and the HIJING [8] event generators were used. An analysis of radiation propagation through the experimental apparatus and the MD response were performed with

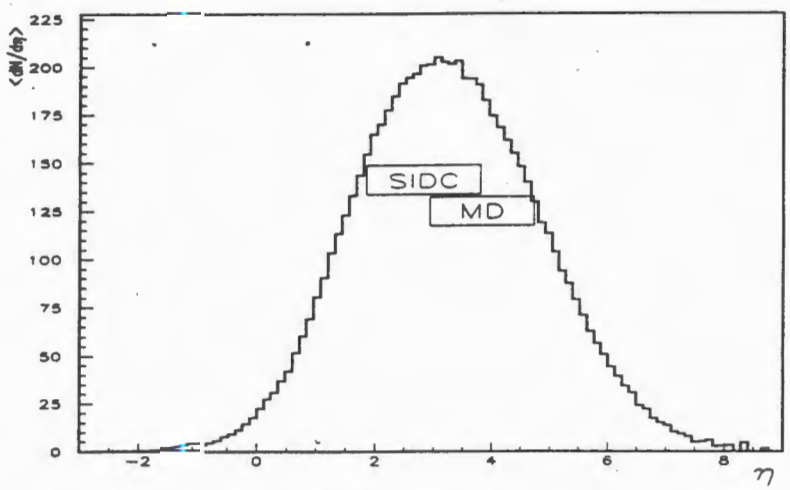

Fig.2. Average charged hadron distribution over pseudorapidity scale for Pb-Au collisions with impact parameters $b < 10$ fm at 160 GeV/n. Pseudorapidity ranges covered by the SIDC and the MD are also shown. The HIJING event generator was used

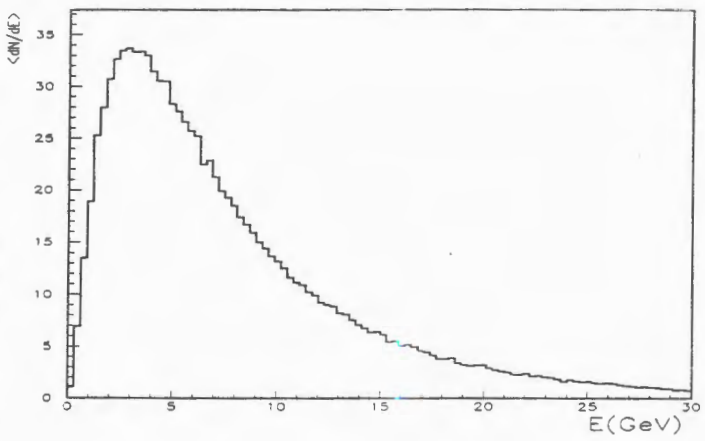

Fig.3. The energy spectrum of charged hadrons produced in Pb-Au collisions with $b < 10$ fm at 160 GeV/n obtained with the HIJING event generator for acceptance of the MD

the GEANT code [9]. A simulation of the projectile nucleus fragmentation characteristics was done according to the experimental distributions [10] where the result of the HIJING calculation was used as input information. The perpendicular momentum of the fragments was generated due to parabolic law [11]. All estimations were done for Pb projectile with energy 160 GeV/n and the gold target. Pseudorapidity distribution for charged secondaries originating from Pb-Au collisions with impact parameters less than 10 fm are shown in Fig.2. In the same figure the pseudorapidity ranges covered by the SIDC and the MD are also shown. Energy distribution of charged particles in the MD acceptance is shown in Fig.3. Practically, all hadrons are relativistic, so energy deposition of each of them inside the MD scintillator corresponds to approximately 1 mip. An analysis of radiation propagation within the CERES area showed that interaction of photons and charged hadrons with matter increases a number of charged particles within the MD acceptance. The result of the

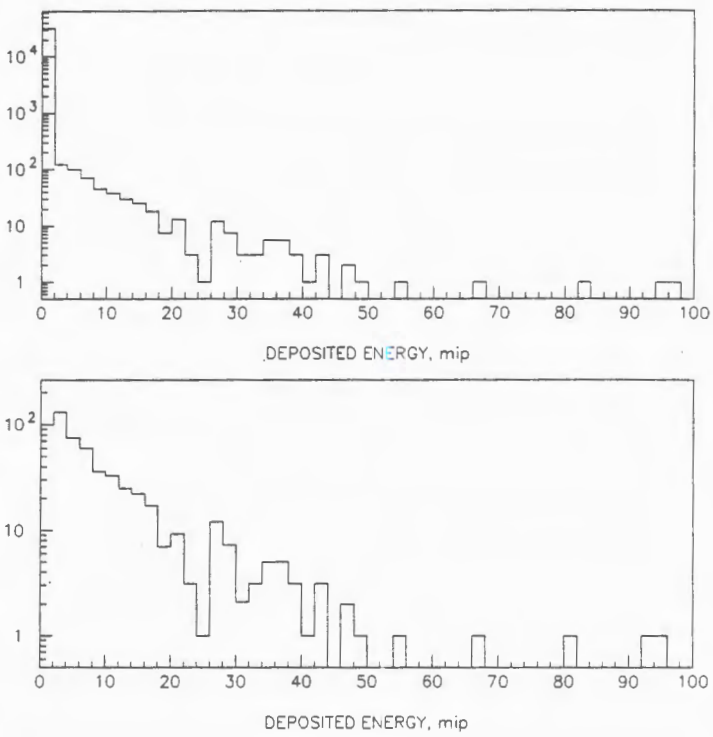

Fig.4. Monte Carlo simulation of the deposited energy distribution for 1-cm plastic scintillator and 10-GeV incident protons, total (top) and for nuclear reactions in the scintillator (bottom)

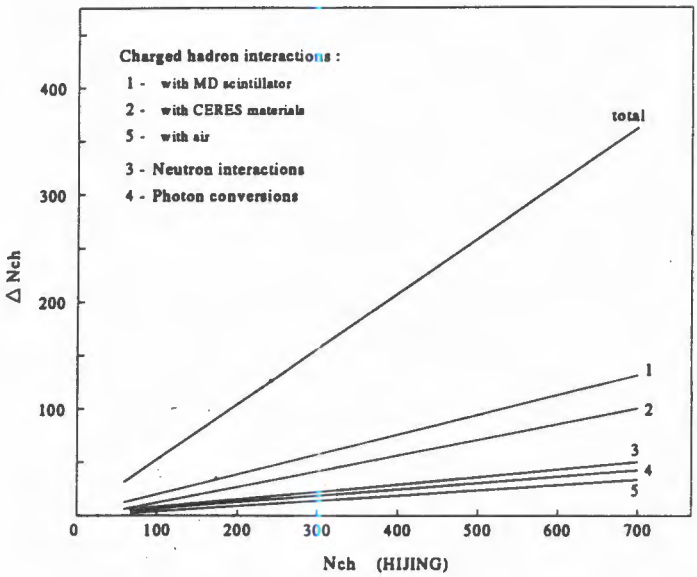

Fig.5. Average contributions from different background processes to the MD response

MC simulation of the energy loss in the MD scintillator for 10 GeV protons is shown in Fig.4. The energy loss per incident proton achieves 100 mips due to the inelastic nuclear

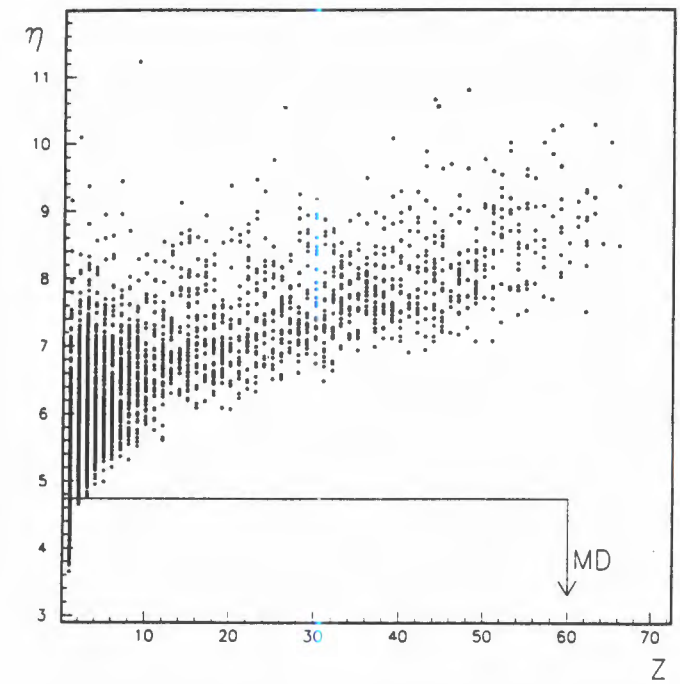

Fig.6. Monte Carlo simulation of the pseudorapidity distribution of lead ion fragments versus the fragment charge for Pb-Au collisions with $b < 10$ fm at 160 GeV/n. The upper edge of the MD region is also shown

interactions inside the scintillator. This is an additional contribution to the MD response, and it is the main source of the counter response fluctuations. The HIJING code predicts in average 657 charged hadrons in the MD acceptance for the central Pb-Au collisions at 160 GeV/n. It was obtained that this magnitude rises by a factor of 1.5 by means of particle multiplication process in the CERES medium. The average contributions from different background processes leading to the increasing of the MD respose are shown in Fig.5. Pseudorapidity destribution of Pb projectile fragments with charge Z for Pb-Au collisions with impact parameters $b \leq 10$ fm is shown in Fig.6. As one can see, there are only single charged fragments in the pseudorapidity region covered with the MD.

4. Counter Design

Each counter of the MD consists of plastic scintillator connected with photocathode of photomultiplier tube FEU-85 by means of the lightguide worked out from polished plexiglass as shown in Fig.7. Each plastic scintillator has 50-cm length and 1-cm thickness with an opening angle of 15°. Polystyrene based scintillators were produced in LHE, JINR. Light collecting homogeneity was achieved with different polishing of main and flanking areas of scintillator. Flanking surfaces with width of 1 cm were polished to the mirror quality level, but the surface of the active zone was done to the diffusion level. Scintillator together with lightguide are wrapped around by an aluminized mylar and black paper. The PMT has 25-mm diameter photocathode and 11 stages of amplification. Important characteristics of FEU-85 are good single electron response and timing properties (rise time and duration of anode pulse are 3 ns and 25 ns, respectively) with pulse height resolution not worse than 9%. Voltage divider of PMT is shown in Fig.8. To provide stable work and to expand dynamical range three last dinodes were supplied from the chain of the diodes BZTO3C150/C180. Voltage supply of the divider is in the range 1500-1600 V, while the value of current through the divider is $\simeq$ 1.2 mA.

An influence of the CERES magnetic field on regime of PMTs was tested at the working conditions in the experimental area of the spectrometer. Two identical samples of counters and different types of magnetic screens were used in test measurements. Results

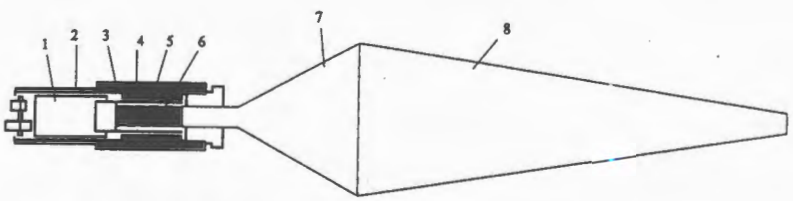

Fig.7. Sketch of a single counter of the MD array (1 — voltage divider, 2 — soft iron tube of the counter, 3 — additional soft iron cylinder, 4 — permaloy-B screen, 5— electrostatic screen, 6 — photomultiplier, 7 — lightguide, 8 — plastic scintillator)

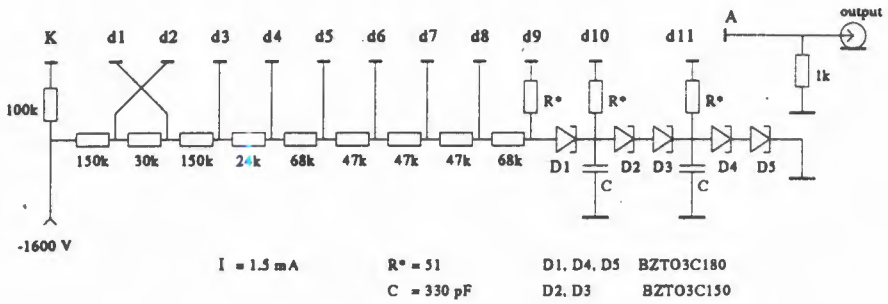

Fig.8. Voltage divider of the photomultiplier FEU-85

are shown in Fig.9 as a function of the distance from magnetic system of the CERES spectrometer. The measurements showed a high influence of the magnetic field on a counter operation at the distance of 1-2 m from the last correction magnet. Testing of different types of magnetic screens led to a choice of final variant of the counter design. The MD was installed at a distance of 2 m from the magnet system (5.35 m downstream of the target position). The PMTs were placed inside the 1.5-mm permaloy-B screen which was put into the counter tubes of soft iron with inner and outer diameters of 36 and 40 mm, respectively. An additional soft iron cylindrical screen, 180 mm long and 3.5 mm thick, was also used. For more stable operation of counter an electrostatic screen was wraped around PMT at photocathode potential. Homogeneity of light output for the MD counter was studied with collimated β-source of ^{144}Ce. Results of measurements are shown in Fig.10 as a map of relative response values for the different hitting points. The pulse height dispersion is less

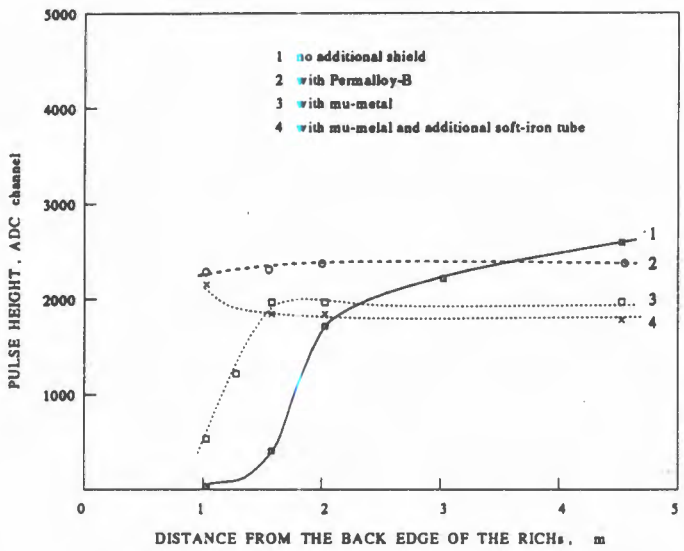

Fig.9. Test results on a dependence of the pulse height response of the MD counter on a distance from the magnetic system of the CERES spectrometer

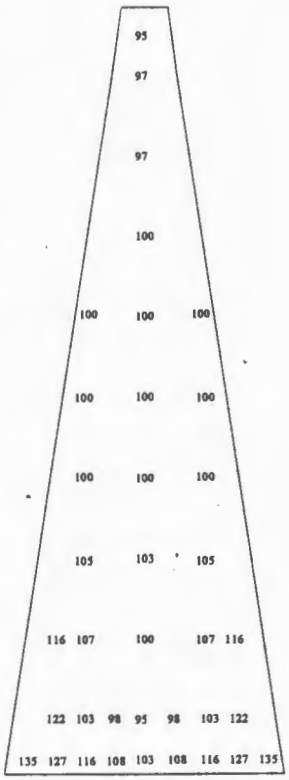

Fig.10. The response map for the MD counter scintillator obtained with a collimated β-source ^{144}Ce

than ~ 5% in the most part of counter active area and only in the angles far from the MD center it rises up to 35%.

The pulse height distribution for mip was also studied with deuteron beam with momentum of 8.9 GeV/c. The results were obtained for 4 cases when deuteron beam passed through the scintillator in three different points 10, 30 and 47 cm from the lightguide along counter axis and through the lightguide itself. For the first three cases the distributions are practically identical, and the beam passage through the lightguide does not produce any additional influence on the counter response.

So a requirement of independency of detector response on a hitting point position is well realized. Similar pulse height distributions for all counters of the MD were measured with muons at CERN and will be discussed below. One can consider this fact as a confirmation of proportionality of pulse height value to a number of hits. In a linear region of the detector, the MD responses for different number of charged mips were obtained with Monte Carlo simulation on a base of 1-mip distribution measured. With increasing of particle number, n, the distribution becomes close to Gaussian shape with a mean value A_n and a dispersion ΔA_n:

$$A_n = n \cdot A_1$$

$$\Delta A_n = 0.45\sqrt{A_n}\,.$$

The MD scintillators were pushed to be close to each other by fixing of the counters on a metallic frame. Dead space between the scintillators was less than 0.5 mm.

5. Signal Processing Electronics

The analog and trigger electronics of the CERES spectrometer is located 20 m from the experimental zone. The HV supply of PMTs is realized by 32-channel system (LeCroy model). Block scheme of electronics providing readout and processing of the MD signals is shown in Fig.11. The timing diagram of the MD signal processing is shown in Fig.12. Signals are taken from anodes of PMTs and brought to the inputs of the discriminators (LHE/JINR model 4F115). These discriminators allow one to set small thresholds ~ 10 mV, i.e., much lower than mean value of mip amplitude. The output NIM signals come to input register and to 24 inputs of majority logic unit (CEAN model, NIM) which generates the signal with a pulse height proportional to a number of pulses from the MD. By VME

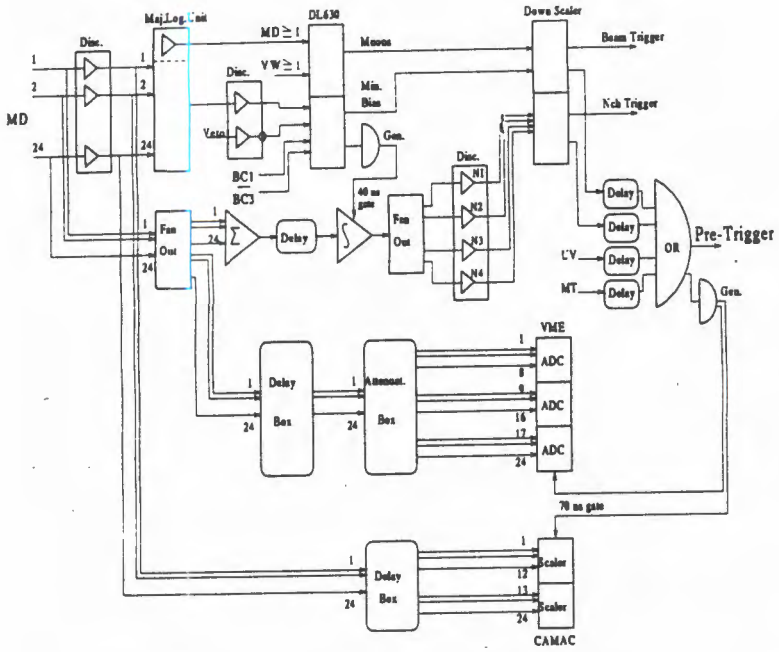

Fig.11. A scheme of the MD signal processing electronics

discriminator (Heidelberg univ. model) one can set a threshold on a number of MD pulses. Fast coincidence of pulse from VME discriminator with pulses induced with BC (BC1, BC3) and veto detectors (VETO) allows one to produce the minimum bias trigger signal by multifunctional logical module (Heidelberg univ. model DL630).

On the one hand, this signal can be used as a trigger with given minimum value of multiplicity threshold. On the other hand, it ptovides time synchronization of the trigger electronics. An experience has shown that a calibration of the MD can be carried out very effectively with the background muons produced by SPS beam in the experimental hall of the North Area. The muons passing through 8-m concrete shield come into the CERES zone. A 20-ns coincidence of signals of two scintillation arrays VW (Veto Wall) and the MD with about the same active areas gives a special trigger signal «muon» for the calibration goal. A distance between the VW and the MD is 9.8 m. The trigger signal appears only in a case if single counters of both arrays have given the pulses at the same time.

Analog signals of the MD are splitted on two branches. One set of the signals passing through a delay box and an attenuator (fine tuning of signal amplitudes) come to inputs of ADCs, VME modules. Another set arives in a sum module (LHE/JINR model 24LS243) which performs an analog summing of the input signals for next step of signal processing by integrator module (LHE/JINR model LV253). A time interval of sum pulse integration is given with 40-ns gate pulse generated by minimum bias trigger signal. As a result the amplitude of integrator signal is proportional to a charge particle multiplicity plus a

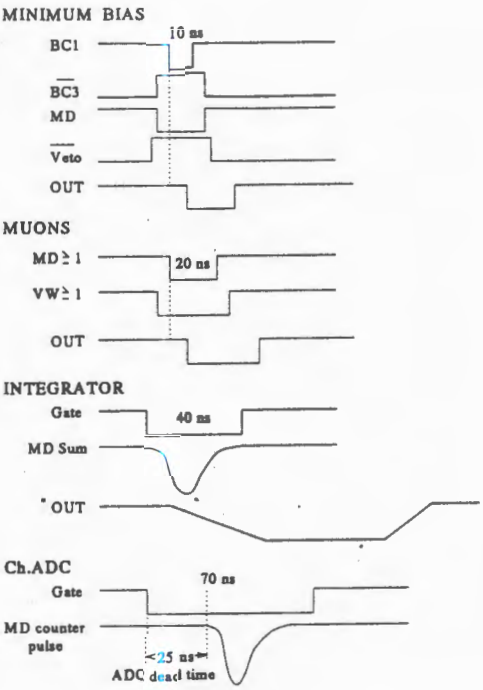

Fig.12. A timing diagram of the MD signal processing

pedestal. This signal after splitting is passed to four inputs of VME discriminator with different thresholds on a multiplicity calibrated. The N_{ch}-trigger signal is provided by the Down Scaler VME module (Heidelberg univ. model) which performs a selection of input signals from the N_{ch}-discriminators in a correspondence with a set of reduction factors. The output signal of this module is sent to the first level trigger electronics to generate the main trigger signal.

6. Adjustment and Calibration

An analysis has shown that the response of the MD for Pb-Au central collisions at 160 GeV/n achieves approximately 950 mips. An adjustment of the MD was performed right before the beginning of experiment when the magnetic system of the CERES spectrometer has been turned on. An investigation of dynamical range of the MD counter operation has shown a good linearity with unchanged pulse shape up to the pulse height value of 2.5 V. So the tuning procedure has a goal to get a correspondance between a maximum deposited energy (~ 60 mips per counter) and above-mentioned dynamical range. At this regim a mean value of pulse height from PMT for 1 mip is $\simeq$ 40 mV. Rough test of working capabilities of the MD counters can be carried out with the light emitted diodes (LED) placed on the lightguides of the counters. Short pulses with pulse height of ~ 70 V are produced for the LED system by a special generator (LHE/JINR model GSD712).

The main stage of adjustment and calibration of the MD was carried out with background muon flux using the special muon trigger. A typical number of the triggers per burst was about 3000-4000.

The fine tuning of 1 mip responses for individual counters was done by playing with the HV supply of PMTs. It was the iterative procedure performed with muon trigger and usually three steps were enough. The typical pulse height distributions measured with muons for some counters are shown in Fig.13.

To study Pb-Au semicentral and central collisions the following set of parameters was settled to realize the minimum bias trigger:

— Thresholds of discriminators for MD counter pulses $\simeq$ 140 mV (> 3 mips);

— Threshold on a number of pulses from the MD array was 15.

Such parameter set corresponded to an effective bias of the trigger of 80-90 mips. The next stage of calibration was an establishment of correspondence between the values of

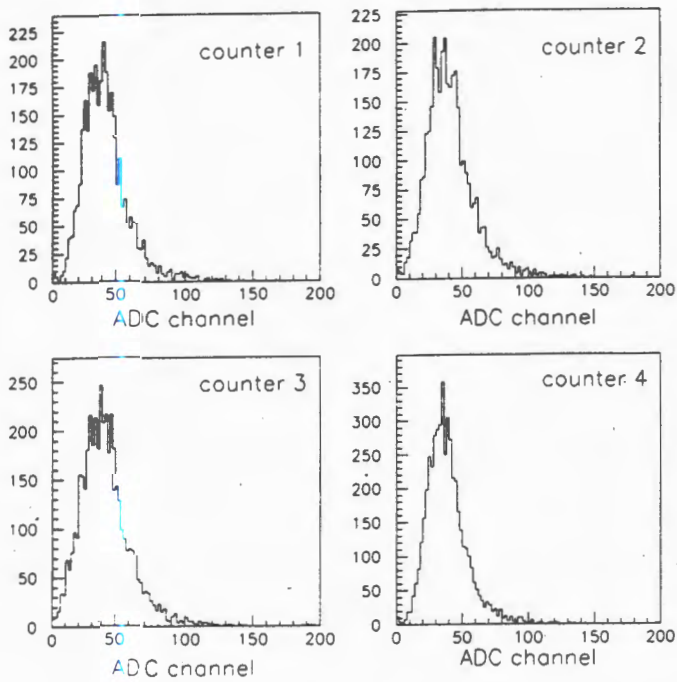

Fig.13. One-mip pulse height responses for some counters of the MD measured with background muon stream generated by the SPS beam in the North Area

discriminator threshold in mV and the multiplicity of particles measured with the MD or, in other words, the calibration of the main first level trigger signal, N_{ch}-trigger. With this aim special measurements for different threshold magnitudes were carried out with the lead-ion beam and the gold target. The distribution of number of charged particles was obtained by summing of 24 distributions measured with the individual counters calibrated before with muons.

7. Test Measurements with Lead Beam

The detector was tested with 160 GeV/n lead beam of the SPS CERN in November 1995. A background response of the MD for the single lead ion passed through the experimental zone without nuclear interactions is shown in Fig.14. Such response can be explained with the δ-electron production upstream of the MD, and it is much less in the case of close nucleus-nucleus collisions without high-charged projectile fragment. So 40 mips in average is the maximum background contribution from the CERES beam line. A correlation between responses of two detectors, the MD and the SIDC, measuring the multiplicity of charged particles for the Pb-Au collisions with the interaction trigger (the lowest bias trigger) is shown in Fig.15. The SIDC1 was located at 9.8 cm behind the target

and, covered the pseudorapidity region $1.8 < \eta < 3.8$. There is a good correlation and linearity between responses of both detectors in all dynamical range. A correlation of two processes such as the multiple charged particle production within the MD acceptance and the projectile fragmentation measured with the Cherenkov counter BC2 is shown in Fig.16 (interaction trigger). The BC2 was located about 1 m behind the MD and covered pseudorapidity region $\eta > 6.7$. The counter response is proportional to the sum of fragment charges squared and so the big response can occur only in a case if the high-charged fragments are available. One can see that there are no big responses of the BC2 for the high-multiplicity events. Only for the peripheral collisions, $N_{ch} < 150$ ($b > 10$ fm), we can observe the fragmentation process with high-charged fragments. The bump in the multiplicity distribution at low multiplicities is explained with a high cross section of lead nucleus disintegration in the peripheral collisions.

A comparison of the experimental multiplicity distribution measured by the MD for Pb-Au collisions at 160 GeV/n with the HIJING-GEANT prediction for four different impact parameter cuts $b < 4, 6, 8$, and 10 is shown in Fig.17. There is a good agreement between experimental and predicted distributions in the range of semi-central and central Pb-Au collisions. The impact parameter regions $b < 10, 8, 6$ and 4 fm approximately correspond to the MD responses with $N_{ch} > 160, 350, 550$, and 750 respectively. The CERES gold target consisted of 8 microtargets of 600 μm diameter and 25 μm thickness, separated along the beam direction by 3 mm. The main statistics in the run'95 was got with the N_{ch}-trigger at the N_{ch}-bias of 300 ($b \simeq 8.5$ fm). The dependence of MD multiplicity on the interaction point, i.e., z coordinate of the vertex, is shown in Fig.18 for two triggers, interaction trigger and N_{ch}-trigger. Vertex reconstruction was done by double tracking device SIDC1,2. The most of produced particles originated in the target region. It is cleary visible there are two additional background sources, the mylar windows of the vacuum pipe at $z = -5.3$ cm and of the Cherenkov counter BC3 at $z = 0.5$ cm in the interaction trigger case. For N_{ch}-trigger one can see practically only particles produced in the gold microtargets.

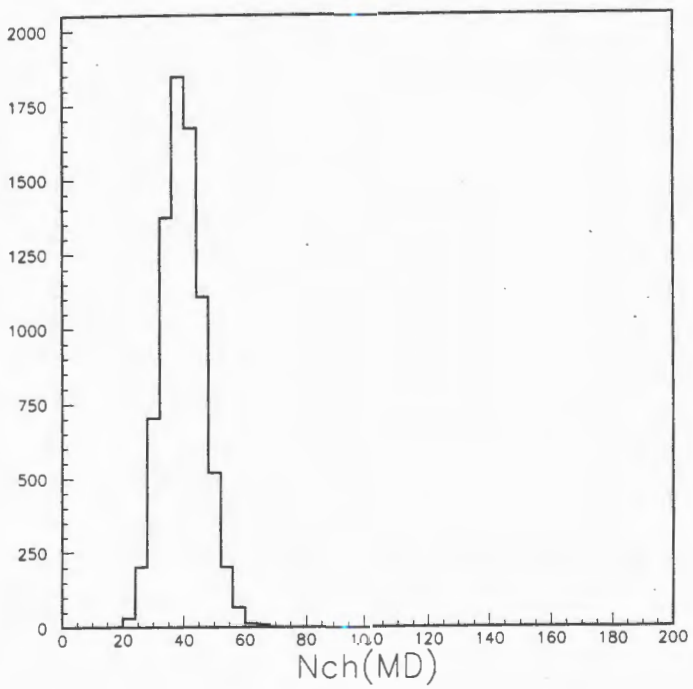

Fig.14. Background response of the MD for the case of single lead ion passage through the experimental zone without nuclear interactions

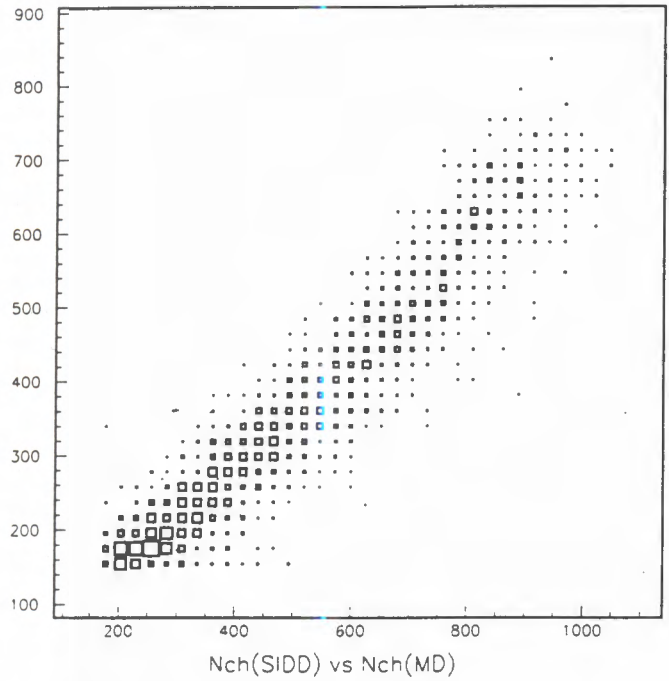

Fig.15. A correlation between the MD and the SIDC responses measured with minimum bias trigger

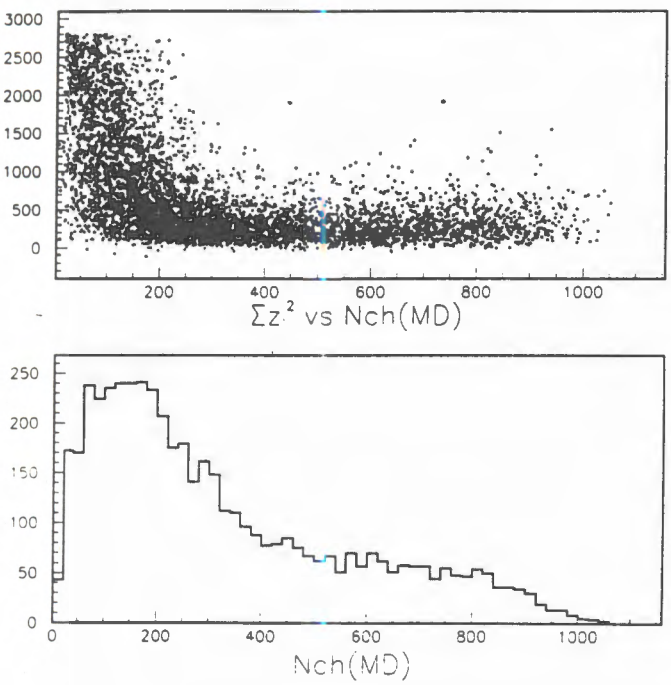

Fig.16. A correlation of multiple charged particle production within the MD acceptance and projectile fragmentation measured with the BC2 (top). A distribution of charged particle multiplicity measured by the MD with the interaction trigger (bottom)

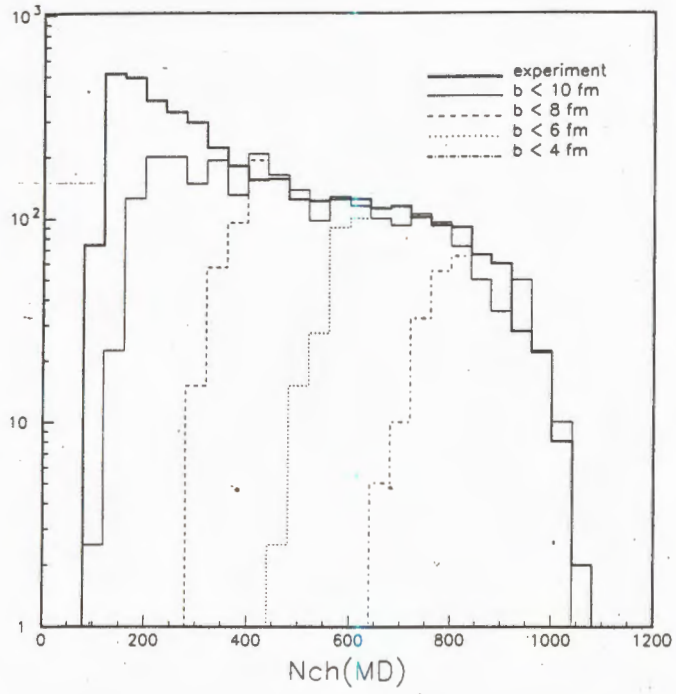

Fig.17. The MD multiplicity distributions measured and predicted with the HIJING-GEANT for the Pb-Au collisions with $b < 10$, 8, 6, 4 fm

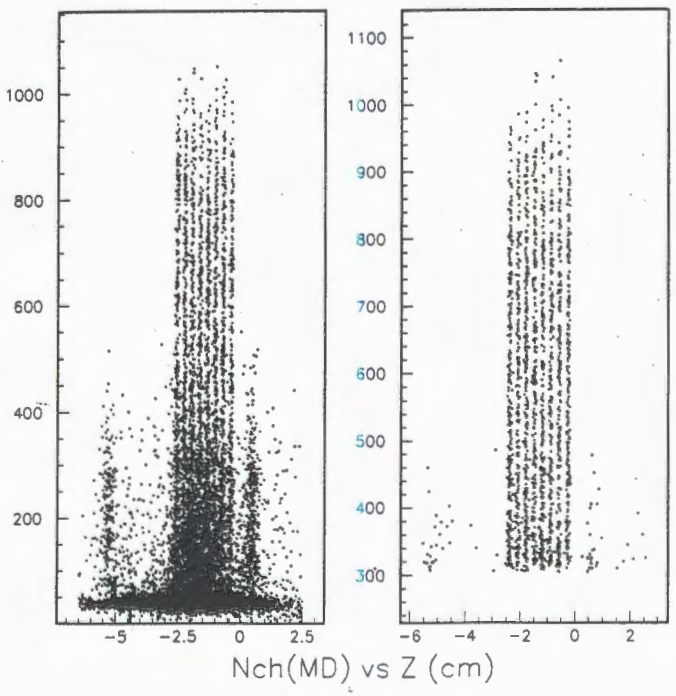

Fig.18. A dependence of the MD multiplicity on Z-coordinate obtained by vertex for the interaction trigger (left) and the N_{ch}-trigger (right)

8. Conclusion

We described the capabilities of the low-segmented scintillation array for the fast multiplicity triggering in a broad dynamical range up to a few thousand mips within the detector acceptance. The active time of the MD is defined by the 40-ns integration of sum pulse and can be even reduced twice. The test measurements with 160 GeV/n lead beam have shown a good correlation and linearity for the multiplicity data obtained with the MD and the SIDC. The maximum background response of the MD is about 40 mips whereas the MD response for central Pb-Au collision corresponds to about 950 mips. The HIJING event generator prediction of multiplicity is in good agreement with the SIDC data and has to be multiplied by a factor of 1.5 with a goal to reproduce the MD results. The GEANT simulation and estimation performed have shown that this effect is produced by particle multiplication process in the CERES medium and nuclear reactions in the MD scintillator. First level triggering with $N_{ch} > 300$ selects only Pb-Au collision events with the impact parameters less than $\simeq 8$ fm. It has been the major trigger for the CERES experiment in 1995 and 1996. In a future we plan to use the MD as one of the major trigger detectors of the DISC spectrometer for nucleus-nucleus collision study at the Nuclotron energy in Dubna.

9. Acknowledgements

We would like to thank the members of the CERES collaboration for their help in detector integration into spectrometer scheme. Specially we wish to acknowledge Prof. I.Tserruya, P.Glassel and P.Wurm for their support of our work and the stimulating discussions.

This work was supported in part by the Russian Foundation for Fundamental Research, Grant No.95-02-05061.

References

1. Holl P. et al. — Proposal to the SPSLC, CERN/SPSLC 94-1, SPSLC/P280, 1994.
2. Gunzel T.F. et al. — Nucl. Instr. and Meth., 1992, v.A316, p.259.
3. Chen W. et al. — Nucl. Instr. and Meth., 1993, v.A337, p.273.
4. Faschingbauer U. et al. — Preprint CERN-PPE/95-132, 1995, to be published in Nucl. Instr. and Meth.
5. Agakichiev G. et al. — Submitted to Nucl. Instr. and Meth.
6. Baur R. et al. — Nucl. Instr. and Meth., 1994, v.A343, p.87.
7. Werner K. — Phys. Lett., 1987, v.B179, p.225.
8. Wang X.N., Gyulassy M. — Phys. Rev., 1991, v.D44, p.3501, Phys. Rev., 1992, v.D45, p.844.
9. Brun R. et al. — GEANT 3.14, CERN Program Library Long Writeup W5013.
10. Adamovich M. et al. — Zeitsch. Phys., 1992, v.C55, p.235.
    Krasnov S.A. et al. — JINR Communication P1-88-252, Dubna, 1988.
11. Lepore J.V., Riddel D.J. — Report LBL-3086, 1974.

Received on December 10, 1996.